National Library of Canada
Bibliothèque nationale du Canada

Canadian Theses Service
Service des thèses canadiennes

Ottawa, Canada
K1A 0N4

NOTICE

The quality of this microform is heavily dependent upon the quality of the original thesis submitted for microfilming. Every effort has been made to ensure the highest quality of reproduction possible.

If pages are missing, contact the university which granted the degree.

Some pages may have indistinct print especially if the original pages were typed with a poor typewriter ribbon or if the university sent us an inferior photocopy.

Reproduction in full or in part of this microform is governed by the Canadian Copyright Act, R.S.C. 1970, c. C-30, and subsequent amendments.

AVIS

La qualité de cette microforme dépend grandement de la qualité de la thèse soumise au microfilmage. Nous avons tout fait pour assurer une qualité supérieure de reproduction.

S'il manque des pages, veuillez communiquer avec l'université qui a conféré le grade.

La qualité d'impression de certaines pages peut laisser à désirer, surtout si les pages originales ont été dactylographiées à l'aide d'un ruban usé ou si l'université nous a fait parvenir une photocopie de qualité inférieure.

La reproduction, même partielle, de cette microforme est soumise à la Loi canadienne sur le droit d'auteur, SRC 1970, c. C-30, et ses amendements subséquents.

NL-339 (r. 88/04) c

Canada

Numerical Calculations

of

Ellipsoidal Blast Waves

by

Mark Mortimer

A thesis submitted to the
School of Graduate Studies and Research
in partial fulfilment of the requirements
for the M.A.Sc. Degree in Engineering

Department of Mechanical Engineering,

Faculty of Engineering,

University of Ottawa

September 24, 1990

ISBN 0-315-68045-8

UNIVERSITÉ D'OTTAWA
UNIVERSITY OF OTTAWA

Abstract

This thesis investigates the progression of a blast wave created by the volumetric explosion of a pressurized ellipsoidal region. The use of numerical methods on a digital processing machine is made. Eight cases of four different ellipticities and two different overpressures were examined to determine the influence of the shape of the blast sources.

It is shown that, for an ellipsoidal cold region generated from a volumetric explosion, the peak pressure through the intermediate fields would be up to three times greater than the peak pressure for an equivalent spherical region and occurs along the initially minor axis of the blast source. The static impulse and the dynamic impulse were also up to two to three times greater than those for an equivalent spherical region, through most of the intermediate and near far fields. A corresponding decrease in the values of these parameters was noted along the major axis.

TABLE OF CONTENTS

Page No.

Acknowledgements

I would like to express my deepest gratitude and appreciation to my thesis advisor, Dr. C.M. Guirao, for her understanding and guidance.

Further, I would like to thank the assistance of Dr. S. Tavoularis for his recommendations and Dr. S. Cheng and Dr. E. Plett for their helpful comments.

I would like to also thank my parents whose unending support and confidence helped me through the task of creating this document.

Finally, I would like to extend my appreciation to Jessie Seetarram, who assisted greatly in bringing this document together, and to the staff of Thomson-CSF Systems Ltd., who always provided much needed moral support.

List of Tables

List of Figures

Chapter 1

Introduction

1.1 Preliminary Remarks

The investigation of blast waves is an important field which has received much attention due to the destructive potential of this phenomenon. The blast wave is a physical occurrence by which a pressure wave of finite amplitude is generated by a rapid release of energy. Though often associated with pressure waves resulting from an explosion used for military purposes, any explosion, whether predetermined or accidental in initiation or nuclear or chemical in reaction type, can create a blast wave.

Predetermined blast sources in addition to an atomic explosion or a condensed chemical explosive such as TNT include bursting pressure vessels, muzzle and breech blasts from guns and recoilless weapons, and reactive gas mixtures. Accidental blast sources may originate from as disparate sources as lightning strikes, propane gas leaks or bursting pressure vessels. The following text describes some current hazards which give rise to accidental blast waves and a brief account of the current means of estimating the blast wave.

The volume and rate at which flammable liquids and vapours are being transported today throughout the world is rapidly increasing. This enhances the possibility of having explosive clouds formed in the atmosphere, as a consequence of a variety of spills and leaks resulting from accidents. This danger associated with the large scale transport of fuels, in particular liquid natural gas, has gained a considerable amount of attention. A specific analysis of a damage scenario with particular emphasis on fuel carriers in the Suez Canal is given by Elbahar and Kamel [1].

Liquified natural gas is also transported great distances above ground through pipelines. Should the pipelines be damaged and allow the gas to escape, wind and atmospheric conditions would distribute this gas into the environment usually in an asymmetrical shape. Given an ignition source, an explosion, then a blast wave would result. As the pipelines go through urbanized areas, to know, a priori, the destructive potential of a natural gas cloud would minimize the possible damage from an accidental explosion by indicating the need to reinforce structures at close proximity to the pipeline.

A common source of accidental explosion is the common hydrocarbon gases such as propane. Whether as a fuel for indoor appliances or as a cooking fuel in outdoor barbecues, this gas presents a hazard with a large destructive potential as has been unfortunately experienced many times. Upon refilling a propane tank, then incorrectly reconnecting the tank to the burner would result in the propane leakage. When the propane burner is ignited, an explosion will occur. A blast wave is created and, usually being at a very close proximity to residential structures, causes a large amount of damage.

The transportation of gases used by the chemical industry presents another type of hazard. Propylene oxide and nitromethane are two potentially highly explosive chemicals transported by rail. The blast hazards defined in chemical terms for vaporized nitromethane is described by Ribovich [2] and an examination of the thermal decomposition kinetics and chemical reactivity is completed by Piermarini et al. [3]. These chemicals with their great destructive potential could lead to a large loss of life given an accidental explosion in a highly urbanized area. If the potential damage could be determined beforehand, an adequate evacuation area about the damaged rail car could be calculated and the people removed to prevent a loss of life.

To know a priori, the damage resulting from a blast wave, the strength of the blast wave, usually quantified as the pressure increase above the ambient pressure, must be determined. Apparently only of theoretical interest before the second world war, the advent of high density chemical warheads and atomic warheads brought a keen need to predetermine the destructive potential from blast sources. As it was difficult if not impossible, to measure the great increase in pressure (as measuring devices could not survive the conditions), alternative analytical means were devised such as using a shock tube for low energy acoustic analysis, then extrapolating to high energy conditions. Later, the use of numerical analysis coupled with field experiments provided an effective joint means to analysis blast waves.

This joint analytical means resulted in accepted computational techniques. However, non-ideal blast waves, typically originating from accidental explosions, distinguish themselves from ideal point blast waves in that the energy release rate as well as the physical dimensions of the energy source are both finite and usually considered to be in the weak shock regime. Further, it has been found that a weak blast has a stronger directionality than a strong blast. Consequently, new methods were needed to analyse the particular phenomena.

1.2 Literature Review

The literature review examines the progress made in the analysis of blast waves, particularly relating to volumetric explosions. Then, the numerical techniques are discussed with emphasis placed upon the requirements for modelling the unique physical characteristics of a blast wave.

1.2.1 The Physical Behaviour of Blast Waves

A thorough description of the physical behaviour of blast waves is presented. This is followed by a review of the current state in the analysis of blast waves.

A typical blast has complex occurrences in both a physical sense and a chemical sense. Though the chemical behaviour of the gases, especially during an expansion, bears directly upon the problem, it is not included in this study in order to enable a clear examination of the effects of the shape of the blast wave. An excellent description of the chemical process is given by Fickett and Davis [4]. For a clear interpretation of the physical bases of the phenomena arising in the field of high temperature gas dynamics, refer to Zed'dovich and Raizer [5]. Here an attempt is made to explain the physical essence of the phenomena using simple mathematical tools, and relying on theoretical discussions.

The physical behaviour of the blast wave is characterized by a blast front which in a discontinuous jump increases the ambient pressure. In addition the blast front in its passage through the ambient atmosphere increases not only the pressure but also the density and temperature, and it accelerates the particles to produce a particle velocity in the direction of travel. It is this discontinuous, irreversible, adiabatic process, also called a shock wave, which presents the major difficulty when analyzing flows with blast waves.

For any finite energy and finite dimension source, the blast wave can also exhibit numerous repeated shocks of small amplitude at various times after the passage of the first shock. This is caused by the successive implosion of rarefaction waves from the contact surface between explosion products and air. Secondary and tertiary shocks of this nature have been observed in experiments by Baker [6], however, they appear to have little effect on any of the characteristics of the positive phase of the blast wave.

When undertaking analysis of blast waves, experimentation has proved useful in determining damage potential. The collection of measurements about an atomic test site in the far field allowed many trends to be found. Scaled chemical explosives allowed the measuring devices to be brought closer to the source and also provided a means of scaling the blast wave depending upon the strength of the blast source. These studies coupled with numerical work allowed a comprehensive analytic study of a high energy point source (eg. solid explosives), blast wave to be made by Baker [6].

In these blast sources, the important energy transfer proceeds by mass flow in strong compression waves, with negligible contributions from other processes like heat conduction. This enables an accurate estimate of potential blast damage by using the total energy to be released by the reaction and scaling the results.

The total energy is considered to be coming from a point source because of the relatively small dimensions of the concentrated charge, the charge dimensions, and the characteristic time for the energy deposition which can be ignored. Nearly all the chemical energy released by these process can be considered to be transferred to the shock front. Thus energy and characteristic explosion length can be derived to scale all ideal explosions as shown by Bach et al. [15].

This estimation using total energy enables the destructive potential of these solid sources or point sources to be determined a priori. Given the mass of the solid explosive charge, the blast energy is calculated, usually as a function of the total weight, before combustion, (combustion energy of the material) and a characteristic explosion length can be derived. Then the blast damages are derived from the overpressure and impulse versus distance curves corresponding to those for tabled TNT explosions. The most common form of scaling is Hopkinson or 'cube-root' scaling which states that self-similar blast waves are produced at identical scaled distances when two explosive charges of similar geometry and the same explosive, but of different size, are detonated in the same atmosphere. The Sach's Scaling Law may also be used for a more general means of scaling the resultant air blast waves. A thorough discussion of these techniques is presented by Baker [6].

In the same text, Baker [6] also provides an excellent source of tables of experimental and numerical data from point sources such as TNT or pentolite spheres. Various scaling techniques are presented to provide the reader with a means to determine the peak overpressure and positive impulse as a function of scaled distance from the source.

Numerical techniques have been used to eliminate the effects of the atmospheric conditions not being studied and to provide precise insight into the flow parameters of the blast wave. In particular, for spherical blasts in air, analytical solutions have been obtained for strong shocks in an ideal gas by von Neumann and Richtmyer [7], for intermediate shocks by Bach and Lee [8], and in the weak shock approximation by Whitham [9]. Some codes have been developed which are capable of analyzing shocks in all three ranges as shown by Brode [10].

For reference, Brode's [10] explosions were simulated for peak overpressures of two thousand atmospheres to less than one-tenth of an atmosphere, though the majority of the information presented is for two cases, one of an initial two thousand fold increase in the ambient pressure, and, the other at an initial hundred and twenty two fold increase. The blast wave parameters include overpressure, density, particle velocity, and wave position as functions of time and space.

The numerical method used in Brode's paper was based on the work by von Neumann and Richtmyer [7]. This method employed an artificial viscosity to dampen out the short wavelengths attributed to the amplification factor, thus removing the instabilities of the numerical technique. The physical equations were resolved using stepwise solutions of difference equations which approximate the differential equations.

Though these studies have been intense and informative, the source of the blast wave was restricted to a point such as would be applicable to a solid explosive. It is realized that experimental studies of blast waves from a shaped source which is of equal interest, have been limited due to the difficulty in creating various initial blast source shapes and magnitudes. To ignite a shaped charge or explode a membrane, simultaneously and evenly everywhere, is extremely difficult. Hence, other means such as numerical methods were used to analyse the progression of blast waves resulting from various shaped blast sources.

Brode [11] has used numerical techniques to establish trends for distributed sources in addition to point sources. The blast wave created from the detonation of a spherical charge of TNT was described based on results of a numerical calculation and was compared to experimental data. The use of similarity conditions commonly used to provide the initial conditions to the flow parameters for point sources was not used hence providing insight into the near field flow parameters immediately upon commencement of the blast wave, heretofore not seen.

The blast wave from a distributed sphere or finite source rather than a point source has been examined before by Brode [12]. The gas dynamics resulting from the release of an isothermal sphere of gas initially at rest and at a high pressure were described by the numerical solution of the differential equations which represent an ideal gas in radial motion.

In a paper by Plooster [13], the shock wave progression from a line source (cylindrical equivalent to a point source) and a cylinder source were examined using both numerical solutions and measurements. This was particularly designed to study the cylindrical shock front produced by a lightning discharge. Consequently, much effort was expended in describing the thermal equation of state, the caloric equation of state and the various changes due to ionization.

The numerical scheme used by Plooster was based upon Richtmyer and Morton's [14] technique, incorporating the artificial viscosity method of von Neumann and Richtmyer [7]. Data were presented for various parameters indicative of a strong blast. It was found that the cylindrical source led to a flow pattern which is initially different from the asymptotic solution, but which rapidly converges upon it. An empirical solution was suggested which concurred with the experimental work.

Oppenheim et al. [44] examined non-steady flow fields formed in an inert atmosphere surrounding an exploding cloud, which was assumed to be spherical. By using self-similar initiations, data for blast waves supported by steady combustion fronts, was gathered. Three kinds of processes were considered; a detonation, a deflagration, and a deflagration representing a flame with a low burning speed. Courant and Friedrichs [42] described the gas reaction in these types of processes.

Though each case of Oppenheim's study exhibited initially distinct characteristics features, especially in the vicinity of the cloud boundary, by the time the front reaches a distance of about five cloud radii, individual differences faded out. Thus, it was concluded, that the potential danger at a relatively short distance from the combustible cloud was practically independent of the particular combustion process by which it was consumed, provided that the flame achieves a sufficiently high velocity. In particular, the transition to detonation is determined to be irrelevant.

The question of scaling the non-ideal blast waves in a manner similar to point blasts obviously presents itself. Bach et al. [15] examined the far field equivalency, energy scaling, and the energy distribution. It was considered that the energy used to prepare the sphere to its bursting state being path independent was arbitrary. The true energy of any given explosion was energy delivered to the environment via work done by the expanding explosion products (neglecting other means of energy transport such as radiation). Given the initial states of the sphere and the environment, this energy was unique since the process of the energy transmission was via a shock wave. Unfortunately, the explosion energy could not be specified a priori without a knowledge of the shock propagation. Only in the case of the ideal point blast in which all the energy release goes to the environment was the explosion energy known a priori.

The question regarding the effect of the types of process has been examined further by Guirao et al. [16] and Bach et al. [8]. In these papers, excellent discussions were presented both on the type of process and the best means of simulating the processes. These papers would provide the interested reader with an excellent quantitative comparisons.

Guirao et al. [16] found that on the basis of the effective blast energy, non-ideal blast waves from fuel-air and oxygen explosives were all equivalent in the far field and the blast parameters scaled according to the explosion length.

Using the energy equivalent defined by the hot sphere and by the cold sphere, Guirao found that for very weak explosions, the shock overpressure was less than that for an ideal point blast of the same energy at the same shock location. For very strong explosions, the far field behaviour for both ideal and non-ideal blasts was identical. For intermediate strength explosions, the shock overpressure was significantly higher than the ideal point blast case.

It was also shown that, in the far field, the equivalent source energy from a fuel-air and oxygen explosion was three times greater than the energy for a point blast.

Using numerical techniques, Guirao found that the initial strength of the blast wave from volumetric explosion being half the value from detonation resulted in a slower decay of the blast strength, hence, larger damages in the intermediate field. The strong blast waves of high energy density generated by solid explosives were less destructive in the intermediate and far fields than the moderate strength blast waves associated with smaller energy density explosions.

Lastly, a study by Chiu et al [17], examined the blast waves from asymmetrical explosions using the ray shock method of Whitham [9] with the Brinkley-Kirkwood [41] method for the numerical analysis. Attention was focused on the question of wave asymmetry rather than the non-idealism arising from the finite rate of energy deposition. It was assumed that the propagation of the asymmetrical blast wave remains in an elliptical shape with only a small change allowable in the elipticity through time. This assumption was believed to be too restrictive and provided apparently acceptable results for only an ellipticity range of 0.5 to 2.0.

It has been only in the last few years that experimental work in shaped, distributed blast sources has been undertaken. A working group headed by Brossard [18] provided data for numerous experimental results for blast waves generated by spherical and hemispherical unconfined gaseous detonations. This study was part of an effort to assess the mechanical effects of an accidental explosion of a hydrocarbon-air cloud.

This group investigated the mixtures of hydrocarbons with oxygen or air at various dilutions. The peak pressure, positive duration, positive impulse, maximum negative over pressure, negative and duration, and negative impulse were clearly correlated with a scaling parameter. Though informative, these experiments do not provide a general analytical technique for the flow parameters, particularly for variable shaped blast sources such as elliptical blast sources.

The study of the flow patterns of a blast wave resulting from a shaped blast source is continued in this thesis. Due to the inability to conduct adequate experimentation, a generalized numerical scheme is used to analyze the flow patterns. For this study, the blast wave is considered to be generated from the sudden rupture of a pressurized ellipsoidal container, that is a volumetric explosion, in order to isolate the effects of the source shape from the reaction method.

1.2.2 Numerical Techniques for Fluid Dynamics in the Presence of Steep Gradients

The field of fluid dynamics constitutes the physical laws and postulates governing the dependent variables of a fluid which is moving. The reader is referred to fundamental fluid dynamics texts such as by Currie [19] for a review of the basic concepts and principles and their relation to specialized fluid flow and Oppenheim [40] for a more specific text on gas dynamics. The following sections examine the specialized field of numerical techniques pertaining to fluid dynamics in the presence of steep gradients.

The use of governing physical relationships relates the mass flow, momentum, and energy transfer of a homogeneous fluid medium. The governing equations of fluid dynamics consist of an indeterminant set of hyperbolic partial differential equations. Much use is made of physical assumptions to limit the complexity and thereby construct a functional solution.

The introduction of a discontinuity such as a shock wave presents a further analytical challenge. One may notice reference to shock analysis in literature dating to 1910. Here Lord Rayleigh [20] and G.I. Taylor [21] discuss thermodynamic considerations related to shock waves.

A paper by Courant, Friedrichs, and Lewy [22], presented the important conditional stability of the difference-equation integration method for partial differential equations often used to model the shock wave.

An early numerical scheme is attributed to von Neumann and Richtmyer [7]. In this paper, an artificial viscosity term was used to ensure that the shock transition would be a smooth one extending over a small number of spatial intervals. Then, a finite-difference equation was constructed which included this dissipation. The viscosity automatically treats discontinuities such as shocks, thus avoiding the 'usual' difficult boundary conditions alongside the moving shock front. However, the near-discontinuity was spread over an infinite number of spatial points for a very weak shock and approaches zero spatial points only for a very strong shock.

Another document by Richtmyer [23] provides, amongst other initial value problems, a more detailed examination of the analysis of fluid dynamics in one dimension. The stability criteria, especially the restrictions on the eigenvalues, clearly demonstrated a necessary condition for a valid numerical scheme. Both the Lagrangean and the Eulerian coordinates basis were examined. This was further expanded by Richtmyer and Morton [14], who attempted to tie together the mathematical side namely, error estimates and convergence proofs, to the practical side, namely the physically sensible such as enforcing positive pressures.

The verification of modelling techniques has continued with Morton [24]. The general convergence and stability theory for finite difference approximations to fluid flow problems was described. The methods of analysis were outlined and applied to a typical problem. Practical stability limits, propagation and conservation properties, and nonlinear instabilities were particular characteristics considered.

The examination of the numerical analysis of a system of conservation laws was undertaken in a paper by Lax and Wendroff [25] who examined several classes of schemes and determined those which have the smallest truncation error and in which the discontinuities are confined to narrow band width.

Chu [26] in his text presented other papers which described how computing has been used to analyze physical problems, especially those which relate to numerical fluid dynamics. Another collection of various methods of numerically techniques for calculating shock waves was supplied by Roache [27].

Harlow [28] demonstrated the use of the particle-in-cell method for fluid dynamics. A region was sub-divided into cells with a length equal to the smallest characteristic length of the problem, ie. a shock width. The cell was supplied with a number of cells which indicated the fluid parameters, with a greater number of particles giving a great accuracy to the model. This method presented a high degree of correlation between experiment and partial theories, however it requires an excess quantity of computer memory for the problem considered here.

Another approach used to model compressible flows is called the Monte Carlo method and is described in a paper by Vogenitz et al. [29]. This method treats flows in the transitional regime between continuum and free molecule flow. This method has been confined to flows with simple boundary conditions usually flows about bodies and free jet flow. Due to the volume of gas involved in the blast study which would necessitate an excess number of molecules to maintain, this method was not employed.

There is promise in the field of finite element analysis with some codes being written to examine fluid flows as shown by Brooks and Hughes [30]. However, the modelling techniques require special software and hardware which was not accessible for this study.

In the difference methods noted, the simple, ideal, inviscid fluid flow when integrated forward in time may generate arbitrarily large gradients in both space and time even if the initial conditions are smooth. Given an unbounded gradient as in the case of a shock, it is with great hardship that any attempt to solve these problems is greeted whether using finite difference or finite element discretizations. Numerical methods which contain little or no inherent numerical dissipation inevitably are afflicted with nonphysical oscillations of 'ripples' which can easily destroy all information content in the calculation.

The numerical technique called the flux corrected transport algorithm developed by Boris and Book [31] and expanded upon in two further articles presented a viable solution. The first article discussed the origin of the algorithm which was designed to provide an accurate means of modelling conservation equations in fluid transport even in the presence of discontinuities. The conservation equations were written in an Eulerian finite-difference form then a diffusion algorithm was used which models the flow in a manner which ensured a stable monotonic solution to preserve the non-negative properties of realistic mass and energy densities.

After the diffusion algorithm, the flux correction term was applied. This term, in a non-linear fashion, removed the stability factors of the diffusion equation. This anti-diffusion was completed in such a way as to generate no new maxima or minima in the solution, nor did it accentuate already existing extrema. Though the positivity was obviously ensured, the preservation of the conservation law was not. This was the non-linearity aspect of the algorithm whereby the adjacent point of each Eulerian point was first examined to ensure the criteria of the anti-diffusion step was maintained before applying the corrected flux. This corrected flux at a half-point then affected the two adjacent points hence, ensuring conservation. Thus, small corrective quantities of material were moved from point to point locally but no net loss or gain to the system as a whole resulted.

Further, it has been shown by Boris and Book [31] that the amplitude and phase errors, when compared to the one-sided diffusion algorithm, the Lax-Wendroff algorithm, the Leapfrog algorithm and the Flux-Corrected algorithm were the least for the Flux-Corrected algorithm. Computer calculations confirmed this analysis for tests preformed on density square waves travelling with constant velocity. The distinctive feature immediately seen from the flux corrected algorithm from the results, was the lack of the significant undershoots and overshoots generated by the other highly diffusive algorithms. This was especially attractive given the jump discontinuity of the shock wave.

The second paper by Book, Boris and Hain [32], expanded upon the definition of the flux corrected algorithm by redefining it as a flux correction technique then applying this technique to general difference schemes. The algorithm was also expanded to general fluid systems. Multi-dimensions and curvilinear geometries are mentioned as a generalization of the given method.

In the first article, four test algorithms have been compared to the flux-correction technique. It was shown in this second article that the flux-correction technique could be in fact used in conjunction with the four test algorithms, with improved results. This was especially true if one wanted to minimize dispersion while maintaining positivity. However, also noted was the high cost, because the flux-correcting technique required about fifty percent more computer time.

The third article by Boris and Book [33], minimizes the remaining numerical error to develop improved flux-corrected algorithms. Several improved FCT algorithms are developed and judged against both standard flux-corrected transport algorithms and an optimal algorithm. The properties of several flux-corrected transport algorithms were studied and the algorithms modified to reduce undesirable amplitude and phase errors which arose from the use of local finite-difference approximations to derivatives. Three types of error were isolated: amplitude errors (damping or instability), phase errors (dispersion), and intrinsic grid representation errors (the Gibbs phenomenon). Primarily, the one-dimensional incompressible continuity equation often called the adjective equation was concentrated upon.

To sum up, the FCT algorithms were seen to be about an order of magnitude more accurate than more-or-less standard non-FCT algorithms.

Flux corrected transport seemed to strongly suppress or eliminate the nonlinear instabilities that resulted in grid-separation errors in many long runs using standard algorithms.

The paper by Zalesk [34] expanded upon the flux corrected algorithm developed by Boris and Book by placing it into a simple generalized format and adding a new algorithm for implementing the critical flux limiting stage in multi-dimensions without resort to time splitting. The 'clipping' problem associated with the original one dimensional flux limiter was also eliminated or alleviated.

A second paper by Zalesk [35] continued the development of this two dimensional algorithm to include shock discontinuities and the associated conservation laws. An example of the algorithm modelling fluid flow in a shock tube was completed. A number of high order and low order (monotone) schemes were proposed. Though reservations were presented by Kreiss [36] about the ability of modelling a curved shape on a rectangular grid, the results of Zalesk have been found to be acceptable.

The high order schemes Zalesk used were the leapfrog method and the leapfrog-trapezoidal method. These are both second order accurate in time and an optional spatial order of accuracy. The leapfrog method required the storage of the values of the parameters from the previous time step and the present time step. The fluxes at the current time step were combined with the parameters at the previous time step to provide the new values for the parameters. The trapezoidal corrector took a weighted average of the flux at the present time step and the projected fluxes.

The leapfrog scheme was examined in greater depth by Kreiss and Oliger [37]. This paper was written for computations in dynamic meteorology and oceanography, where the need to use accurate methods for the integration of hyperbolic equations was the same. The leapfrog scheme of fourth order was shown to be stable when only a small amount of dissipation was used.

The low order schemes presented by Zalesk were the donor cell method and the Rusanov scheme. These were both first order accurate in time and space. It was sufficient that the low order scheme be monotonic and stable hence the accuracy of the scheme was not as great a consideration.

In the paper by Rusanov [38], the low order monotone scheme was defined for problems arising in connection with the propagation and interaction of two-dimensional (or axially symmetrical) non-steady shock waves in gas dynamics. The standard fluid flow equations were written in Eulerian coordinates in two dimensions as the Lagrangian coordinates were found to lead to a considerable loss of accuracy.

The difference method used a diffusion component to ensure the stability of the problem. Allowing for different mesh sizes or, more particularly, different angled boundary walls, each layer was checked to be sure that no flux was able to pass across a cell width in one time step. Recall that this is Courant's conditions of stability. This was shown to be efficient by applying the Fourier method and examining the determinant of the system of equations.

Given the need for an accurate numerical technique to examine the progression of a shock front in two dimensions, the flux corrected transport method of Boris and Book, utilizing the high order difference scheme of Zalesk, and the lower order difference scheme of Rusanov, is used for the numerical scheme in this thesis.

This process uses explicit calculations in a Eulerian coordinate system. The explicit calculations enable coding to be completed directly from the difference algorithms into the software (FORTRAN) and requiring a smaller amount of computer memory usage for each time step. The Eulerian coordinates are also the preferred choice for numerical schemes which use the parameter values at given points through time as required.

1.3 Purpose and Scope of the Investigation

The purpose of this thesis is to provide data relating the shape of a blast source to relative charges in the atmospheric parameters. In particular, the peak pressure, the static impulse, and the dynamic impulse are platted as a function of the initial ellipticity of the gas source.

The study is limited to volumetric explosions in order to isolate the effects of the shape from any reaction effects. Further, the blast is assumed to be symmetric about one axis for the duration of the scenario. This again isolates the effects from any attributes from swirling or mixing of the gas.

In Chapter 2, the governing equations are derived from the physical laws. These equations are then modified to suit the ellipsoidal problem.

The numerical scheme is detailed in Chapter 3. This examines the FCT algorithm, the low order scheme, and the high order scheme. The final difference equations used in the simulation are presented.

In Chapter 4, the results of several simulations given a variety of ellipticities and initial pressurization of the region are discussed. The flow parameters, pressure, density, and velocity are presented in great detail along the axes.

The closing discussion is in Chapter 5 and suggestions for future research are presented in Chapter 6.

Chapter 2

Governing Equations

A blast wave is defined as a process by which a pressure wave of finite amplitude is generated in air by a rapid release of energy. If air is assumed to have the characteristics of a continuous, homogeneous medium, then the laws of fluid dynamics will apply to the subsequent air motion. Basic equations describing the transmission of blast waves through air will be presented here.

By using assumptions, the physical laws of fluid dynamics can be presented as a sufficient set of equations able to predict the physical parameters of the fluid in motion. The physical parameters are the fluid velocity components, pressure, density, temperature and internal energy. The equations governing these parameters are derived from the physical laws of mass, momentum, and energy conservation and an equation of state.

The physical law of conservation of mass leads to the continuity equation. Considering the Lagrange frame of reference, if a given fluid mass is followed as it flows, its size and shape will be observed to change but its mass will remain unchanged.

The mathematical equivalence is:

(2.1-1)

$$\frac{D}{Dt} \int_V \rho \, dV = 0$$

D/Dt - Lagrange operator
V - volume
ρ - density / mass of the fluid

This equation may be converted to a volume integral in which the integrand contains only Eulerian derivatives. This is through the use of Reynolds' transport theorem which results in:

(2.1-2)

$$\int_V \left[\frac{\partial \rho}{\partial t} + \frac{\partial (\rho U_K)}{\partial x_K} \right] dV = 0$$

$\partial/\partial t$ - derivative w.r.t. time
$\partial/\partial x_k$ - derivative w.r.t. space
U_k - velocity components

The tensor notation is used for convenience and indicates the summation over the three coordinate dimensions.

As the volume is chosen arbitrarily, the only way to satisfy the above equation is for the integrand to be nil. Thus the Eulerian equation for conservation of mass is:

(2.1-3)

$$\frac{\partial \rho}{\partial t} + \frac{\partial}{\partial x_k} (\rho U_K) = 0$$

The physical law of conservation of momentum leads to the Navier-Stokes equations. Starting again with the Lagrangian frame of reference, the rate at which the momentum of the fluid mass is changing is equal to the net external force acting on the mass. Using the Reynold's transport theorem, the equivalent form in the Eulerian frame of reference is:

(2.1-4)

$$\frac{\partial}{\partial t} (\rho U_j) + \frac{\partial}{\partial x_K} (\rho U_j U_K) = \frac{\partial \sigma_{ij}}{\partial x_i} + \rho f_j$$

σ_{ij} - stress tensor

f_j - resultant of the body forces per unit mass.

Note that for this equation, the stress tensor has three components of stress (one normal and two shear) on each coordinate plane.

The physical law of conservation of total energy leads to the energy equation. Using the first law of thermodynamics, for a system which is originally at rest and, after some event, is finally at rest again, then the internal energy, due to the event, is equal to the sum of the total work done upon the system and any heat which was added. As we are considering a gas, which is never at rest, the kinetic energy is added to the internal energy to constitute the total energy. The resulting equation is:

(2.1-5)

$$\frac{\partial}{\partial t}(\rho\bar{e} + \frac{1}{2}\rho U_j U_j) + \frac{\partial}{\partial x_K}[(\rho\bar{e} + \frac{1}{2}\rho U_j U_j)U_K]$$

$$= \frac{\partial}{\partial x_i}(U_j \sigma_{ij}) + U_j \rho f_j - \frac{\partial q_j}{\partial x_j}$$

$\bar{e}$ - internal energy

q_j - conductive heat flux leaving the fluid mass per unit time.

Two equations of state complete the list of equations. The first is for the thermal equation of state and the second is for the caloric equation of state, which are respectively:

(2.1-6)

$$P = P(\rho, T)$$

P - normal unit of stress given negligible visions effects (pressure)

T - temperature

and,

(2.1-7)

$$e = c(\rho, T)$$

e - total energy, internal plus kinetic

The complexity of the problem becomes apparent when upon inspection, the above definition provides seven equations to resolve twenty-one unknowns.

Only a few "exact" solutions for limiting cases and restricted geometries are possible for such a complex set of equations. One must usually resort to numerical solution by electronic computer to obtain predictions that can be compared with experiment for the remaining types of problems. However, even with electronic computers, the given set of equations presents a formidable challenge to resolve. It is the physical nature of the particular problem being studied which is now used to make the system determinant.

For the present study, the gas medium may be assumed to be inviscid (ie. having negligible shear forces). The resulting equations are reduced to the Euler equations, which are:

(2.1-8)

$$\frac{\partial \rho}{\partial t} + \frac{\partial}{\partial x_K}(\rho U_k) = 0$$

$$\rho\frac{\partial U_j}{\partial t} + \rho U_k\frac{\partial U_j}{\partial x_K} = -\frac{\partial P}{\partial x_j} + \rho f_j$$

$$\rho\frac{\partial \bar{e}}{\partial t} + \rho U_k\frac{\partial \bar{e}}{\partial x_K} = -P\frac{\partial U_i}{\partial x_i} - \frac{\partial q_j}{\partial x_j}$$

Note that by using the mass conservation equation, the momentum equations have been simplified. Also, to simplify the energy equation, both the mass conservation equation and the momentum equations have been used.

Two last assumptions due to the gaseous medium ensures an equal number of equations to unknowns. In the present context, the body forces associated with gravity are negligible when compared to the pressure forces. Next, assuming that the gas is a non conducting medium, the heat transfer can be neglected. These result in equations for an inviscid, non heat conducting gas which are:

(2.1-9)

$$\frac{\partial \rho}{\partial t} + \frac{\partial}{\partial x_K}(\rho U_k) = 0$$

$$\rho \frac{\partial U_j}{\partial t} + \rho U_k \frac{\partial U_j}{\partial x_K} = -\frac{\partial P}{\partial x_j}$$

$$\rho \frac{\partial \bar{e}}{\partial t} + \rho U_k \frac{\partial \bar{e}}{\partial x_K} = -P\,\partial \frac{U_i}{\partial x_i}$$

Assuming that the gas behaves as a calorically perfect gas, the equations of state become:

(2.1-10)

$$P = \rho R T$$

R – *gas constant*

and,

(2.1-11)

$$e = C_v T$$

C_v – *specific heat at constant volume*

With these assumptions, the original conservation equations have been reduced to as set of seven equations with seven unknowns. Unfortunately, even with these assumptions, few exact solutions are known. Consequently, the use of numerical methods is employed. There is one last modification due to the problem being studied.

As discussed in the literature review, in an accidental explosion, the initial region is usually in an axisymmetrical shape. This naturally indicates that the use of spherical or cylindrical co-ordinates be made. If an axisymmetric shape is assumed to be maintained (that is negligible gas circulation about an axis for the duration of the simulation) then a coordinate may be removed. By using this assumption, the equations are first written into cylindrical coordinates, then the dependence upon the angular coordinate is removed and the height and radial coordinates remain.

In cylindrical coordinates, equation 2-19 becomes:

(2.1-12)

$$\frac{\partial \rho}{\partial t} + \frac{1}{R}\frac{\partial}{\partial R}(R\rho U_R) + \frac{\partial}{\partial \theta}(\rho U_\theta) + \frac{\partial}{\partial Z}(\rho U_Z) = 0$$

$$\frac{\partial (\rho U_R)}{\partial t} + \frac{1}{R}\frac{\partial (\rho U_R U_R R)}{\partial R} + \frac{1}{R}\frac{\partial (\rho U_R U_\theta)}{\partial \theta} + \frac{\partial (\rho U_R U_Z)}{\partial Z} = -\frac{\partial P}{\partial R}$$

$$\frac{\partial (\rho U_\theta)}{\partial t} + \frac{1}{R}\frac{\partial (\rho U_R U_\theta R)}{\partial R} + \frac{1}{R}\frac{\partial (\rho U_\theta U_\theta)}{\partial \theta} + \frac{\partial (\rho U_\theta U_Z)}{\partial Z} = -\frac{1}{R}\frac{\partial P}{\partial \theta}$$

$$\frac{\partial (\rho U_Z)}{\partial t} + \frac{1}{R}\frac{\partial (\rho U_R U_Z R)}{\partial R} + \frac{1}{R}\frac{\partial (\rho U_\theta U_Z)}{\partial \theta} + \frac{\partial (\rho U_Z U_Z)}{\partial Z} = -\frac{\partial P}{\partial Z}$$

$$\frac{\partial (\rho e)}{\partial t} + \frac{1}{R}\frac{\partial (\rho e R U_R)}{\partial R} + \frac{1}{R}\frac{\partial (\rho e U_\theta)}{\partial \theta} + \frac{\partial (\rho e U_Z)}{\partial Z} = -\left(\frac{1}{R}\frac{\partial (R U_R P)}{\partial R} + \frac{1}{R}\frac{\partial (U_\theta P)}{\partial \theta} + \frac{\partial U_Z P)}{\partial Z}\right)$$

Different notation is now introduced for convenience. Further, if the azimuthal symmetry is taken into account, there is no change in the properties of the medium in the azimuthal direction and all references to change in that direction are removed from the difference equations. Finally, in preparation for the numerical technique, the radial difference component is rewritten to provide a source term for each equation. The final set of equations is:

(2.1-14)

$$\frac{\partial \rho}{\partial t} + \frac{\partial}{\partial R}(\rho U_R) + \frac{\partial}{\partial Z}(\rho U_Z) + \frac{\rho U_R}{R} = 0$$

$$\frac{\partial (\rho U_R)}{\partial t} + \frac{\partial (\rho U_R U_R + P)}{\partial R} + \frac{\partial (\rho U_R U_Z)}{\partial Z} + \frac{\rho U_R U_R}{R} = 0$$

$$\frac{\partial (\rho U_Z)}{\partial t} + \frac{\partial (\rho U_R U_Z)}{\partial R} + \frac{\partial (\rho U_Z U_Z + P)}{\partial Z} + \frac{\rho U_R U_Z}{R} = 0$$

$$\frac{\partial (\rho e)}{\partial t} + \frac{\partial [\,(\rho e + P)\,U_R\,]}{\partial R} + \frac{\partial [\,(\rho e + P)\,U_Z\,]}{\partial Z} + \frac{1}{R}[\,(\,\rho e + P\,)\,U_R\,] = 0$$

Chapter 3

The Description of the Numerical Scheme

3.1 Introduction

The numerical approach used to model the ellipsoidal blast wave employs the flux corrected transport. A monotonic low order difference scheme is first used for the transport phase then a correction is made in a nonlinear fashion using the diffusive flux from a high order difference scheme. The low order scheme is discussed first, then the high order scheme, and finally, the flux corrected transport.

3.2 The Low Order Scheme

The prerequisite when choosing a low order scheme is that a stable, monotonic solution must be assured. The low order scheme, developed by Rusanov [38], is particularly well suited for this problem as it was designed for two dimensions, either planar or axisymmetrical non-steady flow.

The governing equations derived in Chapter 2 are rewritten to illustrate their flux components. Equations 2.1-14 when written in the divergence form, become:

(3.2-1)

$$\frac{\partial f}{\partial t} + \frac{\partial F^R}{\partial R} + \frac{\partial F^Z}{\partial Z} + \Psi = 0$$

where f, F^R, F^Z, Ψ are vectors with the four components:

(3.2-2)

$$f = \begin{pmatrix} \rho \\ \rho U_R \\ \rho U_Z \\ \rho e \end{pmatrix} \quad F^R = \begin{pmatrix} \rho U_R \\ \rho U_R U_R + P \\ \rho U_R U_Z \\ (\rho e + P)\, U_R \end{pmatrix} \quad F^Z = \begin{pmatrix} \rho U_Z \\ \rho U_R U_Z \\ \rho U_Z U_Z + P \\ (\rho e + P)\, U_Z \end{pmatrix}$$

$$\Psi = \begin{pmatrix} \dfrac{\rho U_R}{R} \\ \dfrac{\rho U_R U_R}{R} \\ \dfrac{\rho U_R U_Z}{R} \\ \dfrac{(\rho e + P)\, U_R}{R} \end{pmatrix}$$

The difference scheme uses a right-angle lattice with equal spatial steps in each direction. If the temporal step value is defined as the superscript ^{n} and the two spatial step values are designated as the subscripts $_m$ and $_l$ respectively, then the formula for the divergence equation is:

(3.2-3)

$$
\begin{aligned}
f_{m,l}^{n+1} = f_{m,l}^{n} - \Delta t \Psi_{m,l}^{n} - \frac{\Delta t}{2\Delta R} \left(F_{m+1,l}^{R} - F_{m-1,l}^{R}\right)^{n} \\
- \frac{\Delta t}{2\Delta R} \left(F_{m,l+1}^{Z} - F_{m,l-1}^{Z}\right)^{n} \\
+ \frac{1}{2} \left[\phi_{m+\frac{1}{2},l}^{R} - \phi_{m-\frac{1}{2},l}^{R} + \phi_{m,l+\frac{1}{2}}^{Z} - \phi_{m,l-\frac{1}{2}}^{Z}\right]
\end{aligned}
$$

Δt - temporal step
ΔR - spatial step in the radial direction
ΔZ - spatial step in the height direction

Note that the flux term is calculated at the midpoint between two grid points. It is the difference between this average flux term and the adjacent average flux term which is used in the calculation.

The last four terms of the preceding equation are the diffusion components which ensure stability due to the damping out of the short wavelength oscillations. These numerical diffusion terms are further defined as:

(3.2-4)

$$\phi^{R}_{m+\frac{1}{2},l} = \alpha^{n}_{m+\frac{1}{2},l} \left(f_{m+1,l} - f_{m,l} \right)^{n}$$

$$\alpha^{n}_{m+\frac{1}{2},l} = \frac{1}{2} \left(\alpha_{m+1,l} + \alpha_{m,l} \right)^{n}$$

$$\alpha^{n}_{m,l} = \omega \frac{\sqrt{2}}{2} \frac{\Delta t}{\Delta R} \left(w + c \right)^{n}_{m,l}$$

$$\phi^{Z}_{m,l+\frac{1}{2}} = \beta^{n}_{m,l+\frac{1}{2}} \left(f_{m,l+1} - f_{m,l} \right)^{n}$$

$$\beta^{n}_{m,l+\frac{1}{2}} = \frac{1}{2} \left(\beta_{m,l+1} + \beta_{m,l} \right)^{n}$$

$$\beta^{n}_{m,l} = \omega \frac{\sqrt{2}}{2} \frac{\Delta t}{\Delta Z} \left(w + c \right)^{n}_{m,l}$$

ω - stability condition
w - flux velocity
c - speed of sound

The stability condition is shown by applying the Fourier method to the system of equations of 3.2-3. The eigenvalue is obtained, indicating stability restrictions for possible solutions. Upon examination of the roots, it is found that, to ensure a possible solution, the stability conditions must be:

(3.2-5)

$$\sigma^{n}_{o} \leq 1 \;\wedge\; \sigma^{n}_{o} \leq \omega \leq \frac{1}{\sigma^{n}_{o}}$$

$$\sigma_o^n = \max_{m,l} \sigma_{m,l}^n$$

$$\sigma_{m,l}^n = \frac{\sqrt{2}\Delta t}{\delta R} (w + c)_{m,l}^n$$
$$= \frac{\sqrt{2}\Delta t}{\Delta Z} (w + c)_{m,l}^n$$

The second value represents the Courant number modified for two dimensions with equal spatial grid steps. Recall that the Courant condition defining the Courant number requires that no information be passed further than one spatial step during one temporal step to ensure a stable numerical scheme.

For each time step, at each grid point, the sum of the magnitude of the flux velocity and the speed of sound is determined. Then, comparing the values at all grid points (assuming that all cell sizes are identical), the maximum sum is obtained and used to calculate the maximum allowable temporal step. This ensures that no information is carried by the combined flux and fluid flow further than one spatial grid step in one temporal step, and, consequently, it prevents an unstable situation.

Given this discretization of the governing equations in a monotonic low order scheme, the stability of the blast wave simulation is ensured. This low order scheme constitutes the transport phase.

3.3 The High Order Scheme

The high order scheme used to determine the anti-diffusive flux is the leapfrog-trapezoidal predicator-corrector scheme, see Kuriha [43]. This scheme is second order accurate in time and variable order accurate in the spatial differencing.

The governing equations written in flux form (equations 3.2-1) are again used to define this scheme. The leapfrog trapezoidal scheme in one dimension is given by:

(3.3-1)

$$w_i^{*} = w_i^{n-1} - \frac{2\Delta t^n}{\Delta x} \left[F^n_{i+\frac{1}{2}} - F^n_{i-\frac{1}{2}} \right]$$

$$f^{*} = \frac{1}{2} \left(f_i^n + f_i^{*} \right) = \frac{1}{2} \left(f\left(w_i^n \right) + f\left(w_i^{*} \right) \right)$$

$$w_i^{n+1} = w_i^n - \frac{\Delta t^n}{\Delta x} \left[F\left(f^{*} \right)_{i+\frac{1}{2}} - F\left(f^{*} \right)_{i-\frac{1}{2}} \right]$$

This is easily expanded to multiple dimensions by adding respective difference terms to the first equation. The spatial accuracy is determined by the functional dependence of F on f. The formulae were derived by Zalesk [34], for any order of spatial accuracy. The formula differentiates the Lagrange interpolation formula $(df/dx)_i$ and ensures that the flux dependence ([F i+1/2] / Δx) maintains the order of accuracy required.

For example, the five point Lagrange interpolation formula is

(3.3-2)

$$\begin{aligned}F(x) &= \frac{(x-x_2)(x-x_3)(x-x_4)(x-x_5)}{(x_1-x_2)(x_1-x_3)(x_1-x_4)(x_1-x_5)} f_{i+2} \\ &+ \frac{(x-x_1)(x-x_3)(x-x_4)(x-x_5)}{(x_2-x_1)(x_2-x_3)(x_2-x_4)(x_2-x_5)} f_{i+1} \\ &+ \frac{(x-x_1)(x-x_2)(x-x_4)(x-x_5)}{(x_3-x_1)(x_3-x_2)(x_3-x_4)(x_3-x_5)} f_{i+\frac{1}{2}} \\ &+ \frac{(x-x_1)(x-x_2)(x-x_3)(x-x_5)}{(x_4-x_1)(x_4-x_2)(x_4-x_3)(x_4-x_5)} f_1 \\ &+ \frac{(x-x_1)(x-x_2)(x-x_3)(x-x_4)}{(x_5-x_1)(x_5-x_2)(x_5-x_3)(x_5-x_4)} f_{i-1}\end{aligned}$$

This formula is differentiated and calculated to a fourth order of accuracy. The results are;

(3.3-3)

$$F_{i+\frac{1}{2}} = \frac{7}{12}\,(\, f_i + f_{i+1}) - \frac{1}{12}\,(\, f_{i-1} + f_{i+2})$$

This is the high order flux calculation scheme for each grid point.

As this was the interpolation scheme used in the simulation, a fourth order spatial accuracy will be obtained by the high order difference scheme.

3.4 The Flux Corrected Transport

The FCT algorithm consists of two major stages, a transport or convective stage, followed by an anti-diffusive or corrective stage. Both stages are conservative and maintain positivity. Their interaction enables the FCT algorithms to treat strong gradients and shocks without the usual ripples generated due to dispersions.

In the transport stage, the continuity equations are computed. These are characterized by a large numerical error in the form of a strong diffusion. The anti-diffusive stage then removes any large diffusive term introduced in the transportive stage such that the removal does not accentuate any extreme (maximum or minimum). This is a non-linear technique used to guarantee the stability of the problem using diffusion whenever needed, however, allowing sharp discontinuities to exist.

This flux correction makes the overall algorithm non negative and stable and yet reduces spurious numerical diffusion, the usual stabilizing element of most methods, to a very low level.

The nonlinear technique requires first the results from the low order diffusion scheme as discussed in section 3.2. Then, the anti-diffusive fluxes, being the difference between the flux calculated using the high order scheme and the flux calculated using the low order scheme, are determined. Next, it is determined whether or not any maxima or minima are accentuated should these anti-diffusive fluxes be applied.

To enforce this condition in the case of maxima, first, the sum of all the anti-diffusive fluxes into a grid point are calculated to determine the potential change due to the anti-diffusive flux.

(3.4-1)

$$P_i^+ = \max\ (0, A_{i-(\frac{1}{2})}) - \min\ (0, A_{i+(\frac{1}{2})})$$

A - anti-diffusive flux

Then, to determine that no maxima are reinforced or created, the differences between the current preliminary independent parameters are compared to the maximum of the final independent parameters of the previous time step and the preliminary, independent, immediately adjacent grid points.

(3.4-2)

$$w_i^{max} = \max\ (w_{i-1}^a, w_i^a, w_{i+1}^a)$$

$$w_i^a = \max\ (w_i^n, w_i^{td})$$

w_i^n - previous time step parameters

w_i^{td} - preliminary parameters

This difference is multiplied by the grid spacing to correctly scale the results.

(3.4-3)

$$Q_i^+ = (w_i^{max} - w_i^{td})\,\Delta x_i$$

Then the fraction is found which must multiply all anti-diffusive fluxes into the grid point to guarantee no overshoots. This fraction, which obviously is never allowed to exceed one, is found by dividing the calculated difference by the sum of the anti-diffusive fluxes.

(3.4-4)

$$R_i^+ = \begin{pmatrix} \min\ (1, \dfrac{Q_i^+}{P_i^+}) & if\ \ P_i^+ > 0 \\ 0 & if\ \ p_i^+ = 0 \end{pmatrix}$$

This procedure is repeated to prevent any new minimum from forming. That is, the sum of all the anti-diffusive fluxes out of the same grid point is calculated to determine the potential change due to the anti-diffusive flux.

(3.4-5)

$$P_i^- = \max\ (0, A_{i+(\frac{1}{2})}) - \min\ (0, A_{i-(\frac{1}{2})})$$

Then to determine that no minima are reinforced or created, the difference between the current preliminary independent parameters are compared to the maximum of the final independent parameters of the previous time step and the preliminary independent parameters of the current time step at the grid point and all immediately adjacent grid points.

(3.4-6)

$$w_i^{min} = \min\ (w_{i-1}^b, w_i^b, w_{i+1}^b)$$

$$w_i^b = \min\ (w_i^n, w_i^{td})$$

Similarly the fraction is found which must multiply all anti-diffusive fluxes out of the grid point to guarantee no undershooting.

(3.4-7)

$$Q_i^- = (w_i^{min} - w_i^{td})\,\Delta x_i$$

$$R_i^- = \begin{pmatrix} \min\left(1, \dfrac{Q_i^-}{P_i^-}\right) & if \;\; P_i^- > 0 \\ 0 & if \;\; p_i^- = 0 \end{pmatrix}$$

Finally, as all anti-diffusive fluxes are directed away from one grid point and into an adjacent one, limiting will be taken with respect to undershoots for the minimums and overshoots for the maximums.

(3.4-8)

$$C_{i+\frac{1}{2}} = \begin{pmatrix} \min\,(R_{i+1}^+, R_i^-) & if \;\; A_{i+(\frac{1}{2})} \geq 0 \\ \min\,(R_i^+, R_{i+1}^-) & if \;\; A_{i+(\frac{1}{2})} < 0 \end{pmatrix}$$

This coefficient is used on the anti-diffusive flux to obtain the optimum flux while maintaining positivity and conservation.

3.5 The Boundary and Initial Conditions

Recall that using the Eulerian coordinates allows the value of the parameters at a fixed point to be recorded through time. Thus, the physical region is divided into a number of cells with the point at the centre of the cell being the data to be recorded. It is the changing parameters at these cell points or grid points which provide data for the dynamic analysis.

The cells were arranged in a rectangular grid based on the two axes. These represented the radial and height directions with regard to the ellipsoidal region being studied (recall that the azimuthal coordinate was removed due to symmetry). The grid was mapped onto the axis such that the cell points along each axis were a half a cell width away from the axis (Figure 3.5-1 and Figure 3.5-2). This prevents the unnatural enforcement of a zero velocity should a cell point be located on either axis.

Additionally, by placing the cell points at a half cell width from the axis, it was assumed by symmetry that the values of the cell points on the other side of the axis were equal except for the perpendicular velocity component which was equal in magnitude but opposite in direction.

The initial unique physical parameters: pressure and temperature were allocated to each cell point by using the equation for an ellipsoid and determining if each cell point was at a distance from the centre which put it either inside or outside the ellipsoid. This provided an interface which was not smooth (a problem discussed by Kreiss [36]) but with an adequate fidelity, to not significantly affect the simulation's results.

The boundaries of the problem were fixed using either symmetrical arguments or by maintaining a zero slope. The symmetry argument was used about the axis. That is, the pressure and density were assumed to be mirror values across the axis. The parallel velocity was also assumed to be a mirror value. The perpendicular velocity component was assumed to equal in magnitude however opposite in direction. These arguments were used for both the height and radial axes.

On the other two boundaries of the grid any values required for cells outside this region, such as for the high order interpolation scheme, were given the same value as the value of the cells at the closest boundary point (ie. zero slope).

As data would be lost should the shock front progress past the boundary, a re-scaling technique is used to continue the time steps with only a small decrease in accuracy. The technique temporarily stored every second cell point of each parameter into arrays then erase the original arrays and insert the saved values. This provides values for a quarter of each parameter's array respectively and the remaining three quarters of the array are filled with the ambient value of the parameters. A consequence of this is to double the cell width with the resulting loss in fidelity.

This technique does not adversely affect the simulation as it was found that no one point contained data that would make the simulation erroneous if the value was lost.

Chapter 4

Results

4.1 The Initial Flow Parameters

The initial flow parameters are defined for the simulations undertaken. For all computations, the medium was assumed to be a perfect gas with a constant specific heat ratio of 1.4. No initial temperature difference was considered, as the sphere was assumed to have been created by isothermal compression. The temperature was initially 300 K throughout the domain.

The dimensions were defined using the allowable limit of the available computer memory. The maximum array size for the code was found to be 100*100, hence there were 100*100 grid points. The length scale was considered to be 2 m indicating that the cell width in each direction was 2 cm.

Finally, the pressures within the initial blast source region and outside the region were defined. For this analysis, the pressure outside the region was set equal to the standard atmospheric value of 101325 P and the pressure inside the region was set to various multiples of the atmospheric pressure.

To analyze the effect of the initial distribution of the source region upon the resultant blast wave, eight scenarios were completed. Two different values of the overpressure ratio Δp, defined as;

$$\Delta P = \frac{P}{P_{ambient}} - 1 \tag{4.1-1}$$

were tested. These were 19 and 8. Each overpressure ratio was examined for the same four different initial ellipticities of the source region.

The variables used in the simulation were not scaled to any characteristic value. Full double precision real values of the computer were used to maintain accuracy.

4.2 The Blast Wave Progression for an Overpressure of 19

In this first series of simulations, the initial overpressure was set to 19. This is a typical overpressure for a blast generated from a volumetric explosion of a propane-oxygen mixture. The four initial ellipsoidal shapes were:

i) ellipticity = 1	a sphere
ii) ellipticity = 1.5	a near sphere
iii) ellipticity = 3	a moderate ellipticity
iv) ellipticity = 10	a near cylinder

These are shown comparatively in Figure 4.2-1. For each case, the height axis was the initial major axis and the radial axis was the initial minor axis.

4.2.1 The Blast Wave From a Source with an Initially Moderate Ellipticity for $\Delta p=19$

The results of the simulation with an overpressure of 19 and an initially moderate ellipticity of 3 are described. The ellipticity is moderate but pronounced enough to supply distinctive features of the ellipsoidal blast wave. Five parameters, the time, the pressure, the density, the fluid velocity in the radial direction, and the fluid velocity in the height direction, were analyzed.

The time from initiation is used to scale this simulation with other simulations and to measure the dynamic impulse and the static impulse. This simulation was run for 380 time steps. It was re-scaled when the shock front approached the array boundaries. The re-scaling occurred after the 110th time step, the 220th time step, and the 300th time step. This caused the spatial cell width to be increased by a factor of eight from the original cell width, hence the shock, though still mapped onto three to five cell points, was effectively eight times wider than the original width and was smeared over a large length. The times corresponding to these time steps are shown in Table 4.2.1-1.

The pressure value provides the best indication to indicate the strength of the blast wave. The pressure at iterative time steps, for each grid point, was recorded. Pressure profiles were then plotted which displayed the normalized pressure (recorded pressure/ambient pressure). As the ellipsoidal effects would be felt most along the axes, only pressure profiles along the height and radial axes are analyzed. Further, as the re-scaling changed the distance between each grid point, the profiles for each cell width (that is each re-scaling) have been plotted separately. Lastly, to provide adequate resolution, the curves were plotted for each tenth time step step.

The figures have the time step steps labelled for each curve. To associate a time to these time step steps, use the values recorded in Table 4.2.1-1.

The pressure curve is initially a step as seen for the profile along the radial axis (Figure 4.2.1-1) and for the profile seen on the height axis (Figure 4.2.1-2), labelled as the 0th time step. The subsequent curves on the pressure profile figures show the expansion wave moving into the source and the rapid motion of the interface. As expected, the pressure at the initial interface dramatically decreases. The use in the value of the ambient pressure can be estimated using the Rankine-Hugoniot equations for a normal shock front. With an overpressure of 19, the expected pressure ratio is calculated to be 3.75. This is approximately the same value seen at the interface. The radial axis pressure ratio is greater than this expected ratio by a value of 0.6 whereas the pressure ratio on the height axis is less than the expected ratio by a value of 0.8. The difference in values may be attributed to the degree of curvature of the ellipsoid on the respective axes.

The shock front on the radial axis has progressed further from its initial position than the shock front on the height axis. The pressure ratio has also decreased at a slower rate along the radial axis than along the height axis. These trends are clearly seen when the scale of the ordinate axis of the figures is expanded (Figure 4.2.1-3 and Figure 4.2.1-4).

The continuing normalized pressure profiles are plotted. As the shock front had approached the computer's array limits, the first re-scaling occurred and doubled the cell width (Figure 4.2.1-5 and Figure 4.2.1-6). The shock front continues to progress as expected. The slope at the jump discontinuity of the height axis is decreasing when compared to the shock front on the radial axis. This indicates again, that the strength of the shock front on the height axis is the smaller of the two. The pressure ratio on the radial axis is now decreasing at a greater rate than the pressure ratio on the height axis although it maintains a greater value. The shock fronts on each axis reach the distance of 2.75 m at the same time. After this, the shock front on the radial axis is further from the origin than that on the height axis for all steps. That is, the initial ellipticity of the shock front has inverted. Where the distance from the centre of the shock front on the radial axis compared to the height axis was 1/3, now it has increased to a value greater than one.

After the second re-scaling, the cell width is now four times the original value. The expansion of the blast wave continues as seen on the normalized pressure profiles (Figure 4.2.1- 7 and Figure 4.2.1-8). The shock front on the height axis is still unable to maintain as sharp a shock front as the shock front on the radial axis. The pressure ratio on the radial axis is still greater than that of the height axis indicating a lasting directional quality to the blast wave. The shock front on the radial axis is now about 0.5 m ahead of the shock front on the height axis with respect to the origin.

Also seen on the figures is that the pressure reaches a minimum at the origin, thus indicating that the secondary shock is beginning to form. The magnitude of the secondary shock is about the same on each axis. However, the secondary shock on the radial axis is spreading faster than that on the height axis.

The last re-scaling extended the cell width to eight times the original value (Figure 4.2.1-9 and Figure 4.2.1-10). The primary shock front on the radial axis and height axis continues to decrease. The shock on the radial axis is almost 1 m ahead of the shock on the height axis. The pressure ratio of the primary shock on the radial axis is still greater and decreasing faster than the primary shock on the height axis. Though the figures have sharp features, recall that the cell width has increased by a factor of eight over the original cell width.

The secondary shock fronts along each axis for this re-scaling show the effects of the original ellipsoid blast wave. The radial axis secondary shock is spread over many cell widths and is unable to show a peak. The secondary shock front along the height axis has a significant and sharp peak. Note the normalized pressure value at the origin for the first pressure profile curve (#310) is greater than the normalized pressure value at the primary shock front on the height axis (#310 on Figure 4.2.1-10).

By the last time step, each shock front is at approximately the same distance from the origin. Notice, also, that the magnitude of the pressure ratio of the secondary shock on the height axis is larger than that on the radial axis, which is opposite to the respective pressure ratios of the primary shocks.

Again, behind the secondary shock front, a minimum value for the pressure ratios has been reached at the origin, and the pressure is rising again which is indicative of the formation of the tertiary shock.

The density parameter is now discussed. The difference between each axis with respect to the change in density bears a similarity to the changes of the pressure. The normalized density curves (density recorded/ambient density) are also plotted for each axis (Figure 4.2.1-11 and Figure 4.2.1-12). The curves for the time step steps

0, 50, 100, 150, 200, 250, and, 300, are shown. The times associated with these time step steps (hence curves) are again listed in Table 4.2.1-1.

The significant feature of these profiles is the large density value which occurs in the region immediately adjacent to the initial blast region. This is due to the initial large pressure difference creating a density surge, then the shock front (with a much smaller pressure difference) out distancing this surge. The large density values must then follow normal diffusion laws to disperse.

The shock front is evident for the density curves on both the radial and height axis. Contrary to the pressure, the first density profile curve (0th time step) after the initial curve shows the density to be greater on the height axis than the radial axis. However, this reverses as the density quickly drops on the height axis. The respective distances from the origin follow the pattern of the pressure curves. That is, the shock front on the radial axis is initially closer to the origin than the shock front on the height axis. As the radial shock is stronger, it then moves at a greater velocity and overtakes the shock front on the height axis with respect to the distance from the origin.

The curve for the 50th time step on each of the normalized density profile figures, shows a sharp peak on the radial axis which only appears as a plateau on the second curve of the density ratios on the height axis though the magnitude on the height axis is greater. The curve for the 100th time step on each of these figures, already shows the effect of the shock front out pacing the large initial density redistribution though this has not appeared on the radial axis. The curve for the 150th time step for each axis shows a shock front well established and removed from the initial interface positions. By integrating the area under each curve, it is obvious that most of the original mass inside the blast source region has been moved in a radial direction. The curve for the 200th time step continues this trend, indicating that the large initial value of density has diminished. The region close to the origin is now at a density level less than ambient. The curve for the 250th time step shows a continuation of these trends. The curve for the 300th time step shows a large increase of density at the origin which indicates the formation of the secondary shock wave.

Similar to the pressure, the density ratio on the radial axis for each time step has a greater value than that of the height axis at the primary shock front, implying that most of the mass was transported in the radial direction. This emphasizes the directional quality attributed to the initial ellipticity of the source.

The velocity parameters are now analyzed. The gas is set in motion by the passage of the shock wave. It is the velocity or, more properly, the momentum which determines the mass distribution. As the simulation is in two dimensions, the gas velocity, a vector, is decomposed into radial velocity and height velocity.

The radial velocity curves, normalized with the ambient sound speed, are discussed first. The values along the radial axis are shown in Figure 4.2.1-13 and the values along the height axis are shown in Figure 4.2.1-14. Again, the curves for the time step steps 0, 50, 100, 150, 200, 250, and 300, are shown. These also correspond to the times shown in Table 4.2.1-1. The simulation started with the gas at rest consequently no profile is visible for the 0th time step.

The radial velocity on the radial axis (Figure 4.2.1-13) has an initial peak at the initial interface between the blast source and the ambient atmosphere seen for the 50th time step. The curve for the 100th time step shows the initial peak expanding and flattening. The shock position is clearly evident. The subsequent curves all show this flattening of the initial peak and the progression of the shock front. By the curve for the 250th time step, the velocity has reversed its direction, indicating that mass is now flowing towards the origin and is building the secondary shock. The curve for the 300th time step shows a portion of its length with a negative value indicating a flow which is returning to the origin.

The perpendiculare velocities have non-zero components as the grid points are located a half cell width from the true axis. The normalized radial velocity along the height axis (Figure 4.2.1-14) is 30 times smaller in magnitude for the 50th time step, giving an indication of the shock's smaller strength on this axis than the shock front on the radial axis. The curve for the 100th time step indicates that there is motion all along the height axis and it is bearing mass out from the origin. There is no peak at the initial interface, however, the shock front and a following plateau are evident. The next curves show that the velocity decreases in magnitude, however a greater region of the air is now in motion. The curve for the 250th time step shows the first reversal in the velocity's direction, though the reversal has not yet reached to the origin. The seventh and last curve shows a very small positive velocity component and an expanded region of flow reversal.

The normalized height velocity curves on both the radial axis (Figure 4.2.1-15) and the height axis (Figure 4.2.1-16) are now examined. Again note that the curve for the initial velocity does not appear as the simulation starts the gas from rest. The radial axis is examined first.

The normalized height velocity curves along the radial axis (Figure 4.2.1-15) are the perpendicular velocity components. The curve for the 50th time step has a peak at the shock front and an expanding wave behind it. This motion is then extended from the shock front to the origin by the curve for the 100th time step. This trend continues, as the velocity increases and expands with the shock front. Again, on the curve for the 250th time step, the flow reversal has occurred for the formation of the secondary shock. On the figure's curve for the 300th time step shows a decrease in the positive velocity and the broadening of the region which is flowing into the origin.

The normalized height velocity curves along the height axis (Figure 4.2.1-16) correspond to the component parallel to this axis. The initial peak velocity occurs at the initial position of the interface. By the curve for the 100th time step, the shock front is well removed from this peak velocity. The peak velocity has not noticeably declined. By the curve for the 200th time step, the velocity at the shock front has finally surpassed the initially velocity at the interface. The curve for the 250th time step shows the direction reversal of the flow. This curve expands without much change into the curve for the 300th time step.

When comparing the radial velocity curves along the height axis and the height velocity curves along the radial axis (the perpendicular components), the magnitude of the radial velocity is initially greater than the height velocity component. The curves after the start are similar in shape and magnitude. The last curve shows the radial velocity to be smaller in magnitude and have the peak of the primary shock closer to the origin than for the height velocity curves.

The radial velocity curves along the radial axis and the height velocity curves along the height axis (the parallel components) are noticeably different. The height velocity maintains a large velocity value (or peak) at the original interface. The radial velocity has a slight rise close to the original interface. Each curve has a flow direction reversal on the sixth curve which occurs for approximately the same length with respect to the origin. The magnitude of the velocity in the reversed direction is twice as great for the height velocity than the radial velocity. The last curve shows the radial velocity at the shock front to be greater and further from the origin than the height velocity. The greater value of velocity on the height axis indicates that the gas on the height axis is contributing more mass to build the secondary shock than the gas on the radial axis.

With a moderate ellipsoid as the shape of the initial blast source, the shock front formed on the radial axis was greater in strength than the shock front formed on the height axis and was greater for the duration of the simulation. The pressure jump across the shock front was greater, the speed of the shock front was greater, and the amount of mass change in that direction was greater along the radial axis. However, the decrease in strength along the radial axis was also always greater than along the height axis.

4.2.2 The Blast Wave From a Near Spherical Source for $\Delta p=19$

The near spherical case with an overpressure of 19 was given a small ellipticity of 1.5 for the initial blast region. The small ellipticity was chosen to enable the differentiation between the features representative of ellipsoidal sources and the features representative of spherical sources. Again the height axis was the major axis and the radial axis was the minor axis.

The near spherical case was executed for 320 time steps. This required two re-scaling steps, once at the 120th time step and the second at the 230th time step. The final cell width was four times greater than the initial cell width.

The normalized pressure profile curves are plotted for values along the radial axis (Figure 4.2.2-1) and for values along the height axis (Figure 4.2.2-2). The curves for the time step steps 0, 50, 100, 150, 200, 250, and 300, are shown. The times associated with each of these steps are shown in Table 4.2.2-1.

A large pressure decrease on each axis was again recorded after starting the simulation. The radial axis pressure ratio is barely greater than the pressure ratio along the height axis. The shock front retains its sharp rise for both the height axis and the radial axis though again the radial axis has a greater or more abrupt slope.

The shock front in the radial direction starting closer to the origin than the shock front in the height direction maintains a greater pressure ratio and is able to proceed further from the origin by the last time step.

For this ellipticity, the shock fronts on each axis reach a distance of 2.25 metres from the origin at the same time. The last curve, at the 300th time step, shows the shock front on the radial axis to be 0.5 metres further than the shock front on the height axis.

The secondary shock formation is evident by the rise in pressure at the origin of each figure. The shock front on the radial axis again has a smaller slope than the shock front on the height axis.

The normalized density profile curves for both the radial axis (Figure 4.2.2-3) and the height axis (Figure 4.2.2-4) show trends similar to the density curves given a source with the same overpressure and a moderate ellipticity of three. However, the difference between the corresponding curves of each figure is smaller due to the small initial ellipticity. The time step steps are the same as for the pressure and the times associated with each of these curves is again shown in Table 4.2.2-1.

The radial axis continues to have the greater density figures along the lengths of its curves which follow the shock front. This is the case for the duration of the simulation, which is contrary to the equivalent curves with an ellipticity of three.

The shock fronts on each axes maintain the distance from the origin as has been seen on the pressure curves previously discussed in this section. This also applies to the respective shock magnitudes on each axis.

The normalized velocity components' curves are also plotted. These are shown for the radial velocity on the radial axis (Figure 4.2.2-5) and the radial velocity on the height axis (Figure 4.2.2-6) and the height velocity on the radial axis (Figure 4.2.2-7) and the height velocity on the height axis (Figure 4.2.2-8). The time step steps are the same as for the pressure and the times associated with each of these curves is again shown in Table 4.2.2-1.

The velocity components on each axis which were parallel to that axis were found to be an order of magnitude greater than the perpendicular velocity components. The distinction between the two parallel velocity components, that is, the height velocity on the height axis and the radial velocity on the radial axis, is maintained.

The height velocity curves along the height axis had a greater plateau region behind the shock front for the 150th and 200th time step than was seen for the same case but with an ellipticity of 3.

The reversed velocity which forms the secondary shock is again of greater magnitude in the height axis than on the radial axis by a factor of about 1.5. However, by the 300th time step, the reversed flow has still not gone to the origin, indicating that the secondary shock is taking a longer time to form for this case than for the case given an initial ellipticity of 3.

4.2.3 The Blast Wave From a Near Cylindrical Source for $\Delta p=19$

The near cylindrical case with an overpressure of 19 was given a large ellipticity of 10 for the initial blast region in order to perceive differences between the features representative of an ellipsoidal source and the features representative of a cylindrical source.

The near cylindrical case was executed for 300 time steps. This required 2 re-scaling steps, once at the 50th time step and the second at the 190th time step. The final cell width was four times greater than the initial cell width.

The normalized pressure profile curves are plotted for values along the radial axis (Figure 4.2.3-1) and for values along the height axis (Figure 4.2.3-2). The curves for the time step steps; 0, 20, 50, 100, 150, 200, 250, and 300 are shown. The accumulated time in seconds is shown in Table 4.2.3-1.

The trends as discussed for the case of an ellipticity of 3 continue and are accentuated. The shock front on the radial axis maintains a sharp discontinuity however on the height axis the sharp shock front is all but washed out by the last time step. The radial axis peak pressure ratio is more than twice that of the peak pressure ratio on the height axis initially, and is still appreciably greater at the last time step.

The shock front along the radial axis starts much nearer the origin than the shock front proceeding in the height direction. The shock fronts are at the same distance from the origin at about 4 m. At the last time step, the shock front along the radial axis is a full meter further from the origin than the shock front on the height axis.

The secondary shock formation is spread through so many cells on the radial axis that the characteristic sharp shock front is not evident. Relatively, a sharp front exists for the secondary shock on the height. Neither of these shock fronts had detached themselves from the origin. It is interesting to see the secondary shock fronts starting to form a hundred time steps sooner in this ellipticity than for the case with an ellipticity of three. This is due to initial proximity of the blast source interface to the height axis.

The normalized density profile curves for both the radial axis (Figure 4.2.3-3) and the height axis (Figure 4.2.3-4) show trends similar to the density curves given a source with the same overpressure and a moderate ellipticity of three. However, the difference between the corresponding curves of each figure (that is the along the height axis and along the radial axis) is larger due to the large initial ellipticity. The time step steps are the same as for the pressure and the times associated with each of these curves is again shown in Table 4.2.3-1.

There is very little density increase in the direction of the height axis. Most of the density increase occurs on the shock interface which is along the radial axis. This large increase at the start of the simulation again is seen to disperse.

The value of the density ratio along the radial axis is about twice that of the density ratio along the height axis, consistent with the verification of the pressure.

The density is increasing, which is indicative of the formation of the secondary shock. The secondary shock may be significant, because at the last time step the density value was almost twice that at the shock front. Again, as the secondary shock front on the radial axis is washed out, and the secondary shock on neither axis has detached, these observations are speculative at best.

The curves for the normalized velocity components are also plotted. These are shown for the radial velocity on the radial axis (Figure 4.2.3-5) and the radial velocity on the height axis (Figure 4.2.3-6) and the height velocity on the radial axis (Figure 4.2.3-7) and the height velocity on the height axis (Figure 4.2.3-8). The time step steps are the same as for the pressure and the times associated with each of these curves is again shown in Table 4.2.3-1.

The velocity curves are similar in appearance to the velocities in the case with moderate ellipticity, with some accentuation. The perpendicular components of the velocity along each axis are an order of magnitude less than the parallel velocity components. The height velocity component on the radial axis is two orders of magnitude less than the radial velocity component on the same axis. There is a strong contribution from the flow reversal which is shown on the curve for the 250th time step. For a distance up to one meter from the origin, this perpendicular velocity component is of almost equal magnitude as the parallel velocity component.

The radial velocity component along the height axis has a peak value just past the initial interface as does the parallel velocity component. By the 150th time step, the radial velocity component is less than two orders of magnitude smaller than the parallel velocity component.

The height velocity on the height axis has the same shapes for the first three curves as that for the height velocity of the case of moderate ellipticity. The initial large velocity due to the formation of the shock front remains up to the 150th time step, even though between this peak and the shock front, the flow has already reversed directions. This prevents any flow out from the origin, and during the next time steps, the flow from this point to the origin is completely reversed.

The radial velocity has an initial peak velocity at the interface, then the shock front maintains the maximum velocity as it progresses away from the origin. This follows the more traditional progression for normal shocks, as, in effect, it is a normal shock along the radial axis for most of the time simulated.

For this simulation we see two quite distinct types of shock fronts progressing along each axis. On the radial axis there is the appearance of a shock front from a steady state flow with no curvature effects. The height axis immediately takes on the characteristics of an acoustic or low energy shock front.

4.2.4 The Blast Wave From a Spherical Source for $\Delta p=19$

The spherical case with an overpressure of 19 was given an ellipticity of 1. This case was simulated to both isolate the features between the ellipsoidal blast source region from the spherical blast source and to test the results of this code with existing experimental data and other accepted codes.

The spherical case was executed for 300 time steps. This required two re-scaling steps, once at the 130th time step and the second at the 310th time step. The curves plotted for each parameter and each axis were found to be identical until the 200th time step when some numerical error introduces a small discrepancy. This error was a difference in the sixth significant digit, hence, the results were assumed symmetrical for the complete simulation.

The normalized pressure profile curves are plotted for values along the radial axis (Figure 4.2.4-1) and for values along the height axis (Figure 4.2.4-2). The curves for the time step steps; 0, 20, 50, 100, 150, 200, 250, and, 300, are shown. The time required for execution is shown in Table 4.2.4-1.

The pressure curves are similar in shape to those in the case with a near spherical ellipticity blast source. The magnitude of the secondary shock of the spherical case is greater than that for either of the axes for the ellipticity of 3 case.

The density and velocity components are not presented as their values were not used further in this analysis.

4.3 The Blast Wave Progression for an Overpressure of 8

The second series of simulations were conducted with an overpressure of eight throughout the initial blast region. This is a typical overpressure for a blast generated from the volumetric explosion of a propane-air mixture. The four initial shapes of the blast region are repeated. These are:

i) ellipticity = 1 a sphere

ii) ellipticity = 1.5 a near sphere

iii) ellipticity = 3 a moderate ellipticity

iv) ellipticity = 10 a near cylinder

Refer to Figure 4.2-1 for the relative shapes of these sources. Again, for each case, the height axis was the initial major axis and the radial axis was the initial minor axis for the blast source.

4.3.1 The Blast Wave From a Source with an Initially Moderate Ellipticity for $\Delta p=8$

The results of the simulation with an overpressure of 8 and a moderate ellipticity of 3 are described. The ellipticity is moderate but pronounced enough to supply distinctive features of the ellipsoidal blast wave. Five parameters the accumulated time, the pressure, the density, the fluid velocity in the radial direction and the height direction, were analyzed. These are used to compare with the simulations completed with an overpressure of 19.

The moderate ellipsoidal case was executed for 430 time steps. This required three re-scalings, once at the 140th time step, again at the 250th time step and the last at the 340th time step. The spatial cell width had increased by a factor of sixteen from the original cell width, hence the shock front which was originally mapped onto approximately four cells, is after the last re-scaling, mapped onto equivalently 32 cells of the initial cell width. This demonstrates the degree of spreading which had to be accepted to continue the simulation.

The normalized pressure profile curves are shown for values along the radial axis (Figure 4.3.1-1) and for values along the height axis (Figure 4.3.1-2). These curves represent values for the time steps steps: 0, 20, 50, 100, 150, 200, 250, 300, 350 and 400. The time for each time step is shown in Table 4.3.1-1.

The abrupt pressure decrease at the initial interface of each axis due, to the formation, of the shock is again evident. The radial axis pressure ratio is greater than the pressure ratio along the height axis. The shock front appears to maintain its sharp slope equally well for each axis.

The primary shock front travelled at a greater velocity on the radial axis than on the height axis, again. The shock fronts on each axis are approximately three metres from the origin at the same time. By the last time step, the shock front on the radial axis has proceeded a metre further.

The shape of the curve which represents the secondary shock is much clearer and is detached on each axis for the last two profiles. As expected, the secondary shock is much weaker than the primary shock. The secondary shock on the height axis has a greater pressure jump than the secondary shock front on the radial axis, indicating a greater strength. The secondary shock front on the height axis also is at a greater distance from the origin than the shock front on the radial axis. However, the detail is inadequate to discern whether or not this relationship changes.

The normalized density profiles are shown for the radial axis (Figure 4.3-3) and the height axis (Figure 4.3.1-4). The time step steps are the same as for the pressure and the times associated with each of these curves is again shown in Table 4.3.1-1. It is seen that a similar shape exists for each profile but the magnitude is different. Along the radial axis, the density value has the greater increase. The large density increase immediately adjacent to the initial blast region is again evident on each axis. The distance of each shock front from the origin is the same for each axis as that described for the pressure.

The secondary shock appears on the density curves initially at the same (150th) time step on each axis. The maximum density value is the same at the origin. The increase in the density due to the passage of the secondary shock is marginally greater on the height axis.

Note that the density starts to increase again at the origin for the formation of the tertiary shock front.

The normalized velocity profiles were also plotted for each axis. The radial velocity components are shown for the radial axis (Figure 4.3.1-5) and the height axis (Figure 4.3.1-6). The time step steps are the same as for the pressure and the times associated with each of these curves is again shown in Table 4.3.1-1.

The velocity component which is parallel to the axis is again an order of magnitude greater than the velocity component perpendicular to the axis. The peak velocity value on the radial axis is apparent on the initial interface. The curves demonstrate the progression of the rarefaction wave as it proceeds into the origin and the progression of the shock front as it moves away from the origin.

The flow reversal which creates the secondary shock is first noticed on the curve for the 200th time step. By the curve for the 300th time step, the positive motion of the secondary shock is apparent as it detaches itself from the origin.

There is no evident flow reversal for the tertiary shock's formation as suggested by the density profiles.

The normalized height velocity profile curves are shown along the radial axis (Figure 4.1.2.1-7) and along the height axis (Figure 4.3.1-8). The time step steps are the same as for the pressure and the times associated with each of these curves is again shown in Table 4.3.1-1. Again, the parallel velocity components parallel to the axis is an order of magnitude greater than the component which is perpendicular to the axis. The peak velocity value at the initial interface is evident. This peak value remains on the height axis as the shock front advances.

The flow reversal which indicates the formation of the secondary shock is seen on the seventh profile of Figure 4.3.1-8. The detachment of the secondary shock front from the origin is evident.

The curve for the 350th time step of the same figure, shows a second flow reversal of a small magnitude which goes positive on the curve for the 400th time step. That is, the tertiary shock front is forming but is small.

4.3.2 The Blast Wave From a Near Spherical Source for $\Delta p=8$

The near spherical case with an ellipticity of 1.5, was run for 430 time steps. The three re-scaling occurred at the 140th time step, the 230th time step, and the 330th time step. The final cell width was eight times greater than the initial cell width. The profiles curves plotted for the following discussion represent values for the time steps

steps: 0, 20, 50, 100, 150, 200, 250, 300, 350 and 400. The time for each time steps is shown in Table 4.3.2-1.

The normalized pressure profiles are plotted for values along the radial axis (Figure 4.3.2-1) and for values along the height axis (Figure 4.3.2-2). As before, the shock front on the radial axis starting closer to the origin, has a steeper gradient and a greater pressure ratio magnitude across the primary shock front than the shock front on the height axis. On the radial axis, the shock front is also travelling at a faster speed.

The secondary shock front is formed then detaches itself from the origin as expected. There is insufficient detail to determine if the secondary shock front is different on either axis.

The tertiary shock front is not seen on these profiles.

The normalized density profile curves for both the radial axis (Figure 4.3.2-3) and the height axis (Figure 4.3.2-4) show no unexpected trends. The time step steps are the same as for the pressure and the times associated with each of these curves is again shown in Table 4.3.2-1. Again, the large density value increase at the initial interface position indicates the formation of the primary shock front. The formation of the tertiary shock is seen by a small increase in the density value on the last curve of each figure.

The normalized velocity components' curves are also plotted. These are shown for the radial velocity on the radial axis (Figure 4.3.2-5) and the radial velocity on the height axis (Figure 4.3.2-6) and the height velocity on the radial axis (Figure 4.3.2-7) and the height velocity on the height axis (Figure 4.3.2-8). The time step steps are the same as for the pressure and the times associated with each of these curves is again shown in Table 4.3.2-1.

These figures show the expected large velocity for the component parallel to the given axis. Again the component perpendicular to the axis are each at least an order of magnitude smaller. This difference changes to two orders of magnitude when the shock front is at least eight metres from the origin.

4.3.3 The Blast Wave From a Near Cylindrical Source for $\Delta p=8$

The case with the blast source having a near cylindrical shape, an ellipticity of 10, was executed for 380 time steps. The three re-scalings occurred at the 50th time step, the 190th time step, and the 280th time step. The relatively early first re-scaling is due to the initial interface position on the height axis being close to the maximum array length along that axis.

The normalized pressure profile curves are for values along the radial axis (Figure 4.3.3-1) and for values along the height axis (Figure 4.3.3-2). These curves represent values for the time steps steps: 0, 20, 50, 100, 150, 200, 250, 300, 350 and 400. The accumulated time in seconds is shown in Table 4.3.3-1.

As with the other ellipticities of the same initial overpressure, the shock front on the radial axis which is initially closer to the origin, is the stronger shock. It has a steeper gradient and a greater pressure ratio for the duration of the simulation. Associated with this is the capability to travel at a faster rate, and by the end of the simulation, going quite further from the origin than the shock front on the height axis.

The secondary shock front on each axis, detaches itself from the origin as expected. The secondary shock on the height axis appears to have a greater jump across the shock front however there is still insufficient detail to determine if the secondary shock front is different on either axis.

The tertiary shock front is not seen on these profiles.

The normalized density profiles are shown for the radial axis (Figure 4.3.3-3) and the height axis (Figure 4.3.3-4). The time step steps are the same as for the pressure and the times associated with each of these curves is again shown in Table 4.3.1-1. The density profiles exhibit no unusual features. The density increase along the height axis is practically nil compared to the density increase on the radial axis. Again, the density increase at the origin which indicates the formation of the tertiary shock, is seen.

The normalized velocity components' curves are also plotted. These are shown for the radial velocity on the radial axis (Figure 4.3.3-5) and the radial velocity on the height axis (Figure 4.3.3-6) and the height velocity on the radial axis (Figure 4.3.3-7) and the height velocity on the height axis (Figure 4.3.3-8). The time step steps are the same as for the pressure and the times associated with each of these curves is again shown in Table 4.3.3-1.

The figures showed the expected large velocity for the velocity component along the axis which was parallel to the given axis. Again the component perpendicular to the axis are each at least an order of magnitude smaller. This decreases to two orders of magnitude outside the initial interface's position.

4.3.4 The Blast Wave From a Spherical Source for $\Delta p=8$

The spherical case with an overpressure of 8 had an ellipticity of 1. This case was simulated to test the results of this code with existing experimental data and other accepted codes.

The spherical case was executed for 420 time steps. The three re-scalings occurred at the 150th time step, the 240th time step and the 330th time step.

The normalized pressure profile curves are plotted for values along the radial axis and for values along the height axis (Figure 4.3.4-1). The curves for the time step steps; 0, 20, 50, 100, 150, 200, 250, 300, 350 and 400 are shown. The time required for execution is shown in Table 4.3.4-1.

The pressure curves are similar in shape to those of the case with a near spherical ellipticity blast source. The magnitude of the secondary shock of the spherical case is greater than that for either of the axes for the ellipticity of 3 case.

The density and velocity components are again not presented as their values were not used further in this analysis.

Chapter 5

Analysis of the Results and Discussion

5.1 The Comparison of the Four Different Ellipticities for $\Delta p = 19$

The five gas parameters discussed previously are compared for the four ellipticity cases. The peak pressure, dynamic impulse and static impulse as functions of distance are also presented.

The peak pressure is the maximum recorded pressure at a grid point over the duration of the simulation. This corresponds to the maximum value of the primary shock as the shock passes the grid point.

The dynamic impulse often used to characterize blast waves (see Baker [6]) is the accumulation at a point of the magnitude of the velocity squared multiplied by the density, from the time the velocity first increases due to the shock until the time either velocity component first becomes negative (indicating a reversal in the flow direction). This is normalized with respect to the ambient conditions, as:

(5.1-1)

$$I_d = \frac{1}{c_o^2 \rho_o} \int_{\tau_i}^{\tau_{fd}} \frac{\rho \left(v_r^2 + v_h^2 \right)}{2} \, dt$$

The static impulse also used to characterize blast waves (again see Baker [6]) is the accumulation of the overpressure at a point from the time the pressure first increases above the ambient pressure due to the shock until the pressure decreases to less than the ambient value.

(5.1-2)

$$I_s = \int_{\tau_i}^{\tau_{fs}} \frac{\Delta p}{p_o} \, dt$$

The cumulative time at each step for each ellipticity shows a different trend. After a hundred time steps, the near cylindrical case has progressed the furthest, followed by the spherical, near spherical and moderate ellipsoidal shapes respectively. This order is continued to three hundred time steps.

The normalized pressure profile curves for each ellipticity show similar shapes for similar time steps steps. In each case except for the spherical source, the pressure along the radial axis represented a stronger shock front than on the height axis. In each of these cases, the ellipticity changed such that the shock front on the radial axis initially closer to the origin than the shock front on the height axis, was much further away from the origin at the end of the simulation.

The secondary shock for each case except the spherical case had a reflection from the radial axis greater than that on the height axis. That is, the secondary shock on the height axis is greater than the secondary shock on the radial axis (pressure values).

The peak pressure values were recorded by the code automatically. The algorithm to record the peak pressure used the nature of the shock. That is, the peak pressure was presumed to occur after the initial increase due to the shock front initially passing.

The peak overpressure curves along the radial axis were recorded and plotted (Figure 5.1-1). The characteristic length for each ellipticity was defined as the length of the initial interface of a sphere with an equivalent volume divided by the length of the minor axis to the initial interface of the ellipse in question (ie. for the ellipticity of 3 of this study, λ= 0.404/0.25). As seen, as the ellipticity increases, the peak overpressure reaches a plateau at a larger value and for a greater length.

The peak overpressure curves along the height axis were similarly plotted (Figure 5.1-2). The length scale is the same as defined in the paragraph above. Due to the choice of the characteristic length, the trends of curves are not as easily seen. The curves do indicate that, as the ellipticity increases, the peak overpressure decreases.

In another sense, the curvature of the blast source at the radial axis decreases as ellipticity increases in agreement with the results by Chiu et al. [17]. That is, the initial curvature of the shock front is a major indicator of the subsequent strength of the shock front. Effectively, the curvature increased with increasing ellipticity along the height axis, and decreased on the radial axis.

On the axis of minimum curvature (Figure 5.1-1), where the shock front approaches a normal shock front, for all ellipticities, there is an immediate and sharp drop in the peak overpressure as the shock wave begins to move. The peak overpressure itself, remains greater given the greater ellipticity. Past the region where the shock wave forms, a plateau appears for both the near cylindrical and moderate initial ellipsoid. The overpressure of these plateau regions are similar to the overpressure at a normal shock front with a back pressure the same as that given to the blast source. Before these plateaus begin to decrease, the overpressure is a dramatic 2.5 times greater than for the spherical case. The curves do not continue far enough to make an adequate deduction regarding the far field behaviour.

This behaviour is in agreement with that suggested by Plooster [13] with regard to the extent of the plateau though the complete near field data is not shown by Plooster.

On the axis of maximum curvature (Figure 5.1-2), due to the scaling with respect to the position of the interface on the other axis, the curves do not follow any clear pattern. However, by ignoring the scaling, in each case the peak pressure quickly decreases from the value of the blast source. For the spherical and near spherical cases, the peak pressure experiences an abrupt decrease in the slope of the curve. Both the moderate ellipsoid and the near cylindrical ellipsoid appear to maintain a smooth and strong decrease. In each of the cases, it is readily apparent that the overpressure is less with the increase in the ellipticity of the original blast source. Further, the curves appear to be converging to a single value.

The static impulse parameter was automatically collected by the code. The static impulse along the axis of minimum curvature (Figure 5.1-3) shows a general increase with the increase in the ellipticity at each grid point. The curve for the near cylindrical case almost doubles in value for the static impulse than the spherical case for each grid point.

The static impulse along the axis of maximum curvature (Figure 5.1-4) decreases dramatically with the increase in ellipticity. For the near cylindrical case, the decrease is approximately a tenth of the value of the spherical case at the point where the near cylindrical curve begins, which is much less than the doubling of the static increase seen on the radial axis. Again, each curve tends to the same ordinate value as the shock front moves further from the origin.

On comparing the density profiles from each ellipticity, the density curves along the radial axis for each case had the same shape for the same time step. The density value at each grid point of each curve increased as the ellipticity increased. The large density value just outside the initial blast region due to the formation of the shock decreases in initial magnitude as the ellipticity increases. In each scenario, the jump of the density value across the shock front decreases as the shock travels further from the origin.

The density increase at the origin, indicative of the secondary shock, grows to a greater value for the spherical case and decreases with increase in ellipticity. The density curves along the height axis indicate a decrease in the amount of mass increase at the shock front as the ellipticity increases. The curves at each equivalent time step have similar shapes except for the case of a near cylindrical initial blast source. In this case, the shock front is always smoothed. Additionally for this case, the initial mass collection appears to return to the region of the blast source by the rarefaction wave which makes the secondary shock.

Again the density increase at the origin grows to a largest value for the spherical case and decreases with an increase in ellipticity.

Each velocity vector's curves along each axis again resembled each other in shape however along the radial axis, the magnitude increased with an increase in ellipticity and along the height axis, the magnitude decreased with increasing ellipticity.

The peak radial velocity increased by about 120% on the radial axis when comparing the spherical case to the near cylindrical case. The first flow reversal occurs at the 200th time step for the near cylindrical case and the 250th time step in the spherical case.

The peak radial velocity in the near cylindrical case increased by about 200% on the radial axis when compared to the spherical case. The first flow reversal occurs at the 100th time step for the near cylindrical case and the 200th time step for the spherical case.

The peak height velocity decreased to 75% on the height axis when comparing the near cylindrical case to the spherical case. The first flow reversal occurs at the 100th time step for the near cylindrical case and the 250th time step for the spherical case.

The height velocity component decreased to 50% on the height axis when comparing the near cylindrical case to the spherical case. The first flow reversal occurs at the 150th time step for the near cylindrical case and the 200th time step for the spherical case.

This indicates a strong flow along the radial or minor axis of the initial blast source which increases with the increase in increased ellipticity. Additionally, formation of the secondary shock indicated by the reversal of the flow direction begins earlier with an increased ellipticity.

The dynamic impulse along the axis of minimum curvature (Figure 5.1-5) shows an increase in the dynamic impulse with an increase in blast source ellipticity. This accumulates to almost an order of magnitude greater value for the near cylindrical curve, when compared to the spherical case. This is a dramatic increase in this damage factor.

The dynamic impulse along the axis of maximum curvature (Figure 5.1-6) shows a minimal change for all the curves except the near curve from the near cylindrical case when at the intermediate distance. Each curve has a sharp decrease in the dynamic impulse in the later section of the intermediate range however, this drop occurs at a further distance with an increase ellipticity. Though this may be surprising as the greater ellipticity has a larger value, recall that these curves have been scaled which causes the apparent abnormality.

These four cases with an initial overpressure of 19 throughout the blast source show a strong directional influence to the degree of ellipticity. There is evidence of an increase in the potential damage on the axis of minimum curvature between the spherical shaped source and source shaped like a cylinder.

5.2 The Comparison of the Four Different Ellipticities for $\Delta p = 8$

The five gas parameters are again compared for the four ellipticity cases simulated. The peak pressure, dynamic impulse and static impulse as functions of distance are also presented.

Having allowed this series of simulations to proceed an additional re-scaling than those simulations with an initial overpressure of 19, the secondary shock is seen to detach from the origin though it does not become a contributing factor in the progression of the primary shock towards a spherical symmetry.

The peak pressure values are again compared along the axis of either the maximum curvature of the ellipsoid (Figure 5.2-1) and the axis of the minimum curvature of the ellipsoid (Figure 5.2-2). The curves show a similar progression as seen for the case of the overpressure of 19. However, the curves show a stronger convergent trend in the far field as the calculation is carried through an additional re-scaling.

Along the axis of minimum curvature, the peak pressure values again are greater for a larger ellipticity for the duration of the simulation. Again, for the near cylindrical case at the distance where the plateau ceases, the peak pressure is approximately 2.5 times greater than the peak pressure for the spherical case.

Considering the plateau region, for an initial overpressure at a ratio of 8, it is expected that the pressure ratio at the shock front is 3 which is the value seen. Thus with a moderate or large ellipticity, in the intermediate distance, there is a much greater pressure than seen for an initially spherical blast source and the peak pressure is that expected for a normal shock with similar physical initial conditions.

The peak pressure along the axis of maximum curvature (the height axis) has a trend of a decreasing peak pressure value with increasing ellipticity. The decrease appears to be less between each ellipticity than on the other axis however, this is attributed to scaling the length by the length of the initial minor axis.

It is quite evident from both figures showing the maximum pressure curves, that the curves tend to converge in the far field. It is again apparent that the curves tend to the curve of maximum pressures for the spherical case as the distances increases.

The static impulse on the axis of minimum curvature (Figure 5.2-3) shows that all curves have a large initial region of a shallow slope. There is an increase in the static impulse with an increase in ellipticity. There is again almost a doubling of the static impulse between the spherical case and the near cylindrical case.

The static impulse on the axis of maximum curvature (Figure 5.2-4) requires the reader to remember that the axis has been scaled with the initial length of the ellipsoid in the radial direction. Noting this, the trend is again to have a lower static impulse with a greater ellipticity. The spherical case is about twice as large at any distance as the near cylindrical case.

The saw like pattern seen at the ends of each curve on the preceding figures are caused by the inadequacies of the automatic recording algorithms. The changes in the values being recorded are very slight and by re-scaling, some information is not fully recorded for certain grid points. However, by averaging the values on the saw tooth section of the code the correct trend is seen.

The normalized density profile curves which were plotted for each ellipticity in the previous sections had the same shape for the same time step along the radial axis. The density value at each grid point for each profile increased as the ellipticity increased. The initial density increase at the position immediately past the interface, decreases in initial magnitude as the ellipticity increases. In each scenario, the density jump across the shock front decreases as the shock travels further from the origin.

The density increase at the origin, indicative of the secondary shock, grows to a greater value for the spherical case and decreases with every increase in ellipticity.

The normalized density profile curves which were plotted for each ellipticity in the previous sections had along the height axis, a decrease in the size of the density increase at the shock front as the ellipticity increases. The profiles at each equivalent time step have similar shapes except for the case of a near cylindrical initial blast source. In this case, the shock front is always smoothed. Additionally for this case, the initial large density increase appears to return into the region of the blast source by the rarefaction wave making the secondary shock.

Again the density increase for both axes at the origin is greatest for the spherical case and decreases with every increase in ellipticity.

Each velocity vector's profiles along each axis as seen in the figures discussed in the previous sections for the various ellipticities, resembled each other in shape. However, along the radial axis, the magnitude increased with an increase in ellipticity and along the height axis, the magnitude decreased with increasing ellipticity.

The peak radial velocity increased by about 120% on the radial axis when comparing the spherical case to the near cylindrical case. The first flow reversal occurs at the 200th time step for the near cylindrical case and the 250th time step in the spherical case.

The peak radial velocity increased by about 200% on the radial axis when comparing the near cylindrical case to the spherical case. The first flow reversal occurs at the 100th time step for the near cylindrical case and the 200th time step for the spherical case.

The peak height velocity decreased to 75% on the height axis when comparing the near cylindrical case to the spherical case. The first flow reversal occurs at the 100th time step for the near cylindrical case and the 250th time step for the spherical case.

The height velocity component decreased to 50% on the height axis when comparing the near cylindrical case to the spherical case. The first flow reversal occurs at the 150th time step for the near cylindrical case and the 200th time step for the spherical case.

This indicates a strong flow along the radial or minor axis of the initial blast source which increases with the increase in increased ellipticity.

Additionally, the formation of the secondary shock indicated by the reversal of the flow direction begins earlier with an increased ellipticity.

The dynamic impulse along the axis of minimum curvature (Figure 5.2-5) shows a steady increase with respect to the increase in the ellipticity. There is almost an order of magnitude difference between the values for the spherical case and the values for the near-cylindrical case.

The dynamic impulse along the axis of maximum curvature (Figure 5.2-6) shows a decrease with an increase in ellipticity. Noting the effects of scaling, the near-cylindrical case has a large rate of decrease which is slowed until the formation of the shock front. In the intermediate region, the decrease is proportional to the ellipticity, with a magnitude difference between the spherical case and the values for the near-cylindrical case.

These four cases with an initial overpressure of eight throughout the blast source show again a strong directional influence of the degree of ellipticity.

5.3 Discussion

The parameter profiles discussed in the previous two sections, show the progression of a blast wave created by the volumetric explosion of an ellipsoidal source. A verification of the code is made by comparing the spherical results of this study with results from a similar source of other studies. Additionally, the pertinent trends of the flow parameters are now given.

The peak pressure curve for the case of an overpressure of 19 was plotted together with curves representing results by Brode [12] and Bach et al. [15] (Figure 5.3-1). Their simulations were also for volumetric explosions, however the initial overpressure ratio was 22. Their curves which had been normalized (as discussed in Appendix A) were adjusted to this study by using the characteristic length of the spherical case (the length of the minor axis of the blast source). The difference in magnitude between the values for Brode's and Bach's curves and the curve of this study is due to the difference in assumptions for the calculation of the equivalent energy of the initial blast source. Both Brode and Bach used energy equivalent to a hot sphere, whereas the blast source in this study used an equivalent energy originating from a cold sphere. Taking into account this difference, the curves are all very close in value.

The shock front progression on each axis proceeded as seen in Brode's [12] study. A blast wave progresses outward and a rarefaction wave progresses inward. This occurs repeatedly on each axis.

The secondary shock has been examined in depth by Brode. It was shown that a point of coalescence occurs for the primary and secondary shock.

This point was only available for a hot sphere with an initial overpressure ratio of 2003 starting from similarity conditions. Not only is there no equivalent data for the intermediate shock strengths examined, but from the analysis of the pressure profiles of the case with the spherical source and an overpressure of eight, the distance between the primary and secondary shock fronts appear to be increasing, similar to Guirao's [16] work. That is, for weak and intermediate shocks, the secondary shock front may not coalesce with the primary shock front.

The tertiary shock seen forming in this study agrees with the observation by Brode that the repeated formation of an outgoing shock wave and a rarefaction wave should occur, though with a decreasing strength upon each new formation.

Noting the greater magnitude of the primary shock than the secondary shock at any one point, the analysis of damage due to a blast wave will centre on the primary shock front alone.

Examining the ellipticity, one quickly notices the shape of the initial blast source at each axis. On the minor or radial axis, the curvature is least. On the major or height axis, the curvature is greatest. It is believed in agreement with Chiu et al. [17], that the curvature, indicative of the rate of transverse energy of the shock at a point, is an excellent indication of the type of blast wave progression to expect.

Given the greater curvature on the height axis, which is accentuated with a greater ellipticity, the decay rate of the blast wave is greater. For the near cylindrical case (ellipticity of ten), the decay rate was great enough to reduce the impact of the blast wave along the height axis to an acoustic or weak shock level.

This trend is seen even at a slight ellipticity of 1.5, where the peak overpressure and static impulse increased by a factor of 1.1 on the curve of minimum curvature for most of the intermediate region. This value increased by a factor of 1.5 for an ellipticity of three and to a maximum factor of 2.5 for an ellipticity of ten. On average the increase is a factor of 2 for an ellipticity of ten, through the intermediate region.

Each non-spherical case appeared to converge to the values from the spherical case. This agrees with the deduction that given a great enough distance, any initial blast region shape should appear as if originating from a sphere. The increase in ellipticity did extend the region through which the blast front had a much greater effect in the peak overpressure. This is particularly noticeable in the from of a plateau seen in the curves for ellipticity of three and ten. This effectively gives a range over which a fairly constant and large pressure would cause much greater damage due to the shape of the initial blast region.

It is believed that the plateau region is caused by the extended length of the initial ellipsoid which has a negligible curvature. This effectively acts like a normal shock along the radial axis. For a normal shock the initial overpressure would create such a plateau magnitude. The length of the plateau appears to be determined by the curvature of the interface. The plateau length is approximately 0.5, 2.5 and 9 times greater than the spherical case for the increasing ellipticities respectively.

The dynamic impulse showed different percentage increments with the change in the ellipticity. For the ellipticity of three, there was an increase of 200 % and an increase of 500 % and 1000 % for the ellipticities of three and ten respectively.

When the initial overpressure of the exploding source was reduced to eight, the change in progression of the blast waves on each axis was similar. Again, the axis where the curvature was initially minimum (the minor or radial axis) is examined as this is the axis for maximum potential damage.

The peak overpressure and static impulse showed a similar increase with the increase in ellipticity. Average increased values of 130 %, 150 % and 200 % are again seen in the intermediate region for the ellipticities of 1.5, 3, and 10 respectively.

The plateau region, measured as described previously, had increases of 2.6, 5.0 and 12 times greater than the spherical case for the increasing ellipticities respectively. These increments are greater than for the case with an initial overpressure of 19.

It is apparent that spherical symmetry is approached for the pressure value in the far field when the shock is weak.

The dynamic impulse showed again slightly greater values of increase with the increase in ellipticity. For the ellipticity of 1.5, there was an increase of 200 % and an increase of 500 % and 1000 % for the ellipticities of three and ten respectively.

Though the respective magnitudes of each of the flow parameters are smaller given an initial overpressure of eight, the region of influence of each of the parameters is greater. As suggested by Courant and Friedrichs [42] and Chiu et al. [17], the degree of directionality increases with a decrease in the strength of the initial blast.

For each series of simulations, the maximum pressure values on the axis of minimum curvature, it is observed that in agreement with Bach [32], the equivalency or energy scaling does not apply to non-ideal blast waves. The energy of the wave in the far field depends on its energy dissipation history as well as on the initial conditions of the wave itself.

By allowing the initial conditions to include the shape of the blast source and if one were to assume that the work done by the blast source is the same for a constant volume of homogeneous gas, then the shape of the blast source will logically redistribute this energy accordingly though the sum total will be the same. Hence in the near cylindrical case, a weak shock wave on one axis, and a strong shock wave on the other axis are observed. It is only in the extreme far field that non-ideal blast wave overpressures and impulses show far field equivalency.

Additionally, the ellipticity effect is most pronounced in the intermediate field. The decay rate of the shock front is closely associated with the curvature of the surface of the initial blast source. In other words, a shallow curvature is capable of greater destruction in the intermediate region than the shock front originating from a sharp curvature.

5.4 Conclusion

The present study used the flux corrected transport as a valuable tool for the analysis of ellipsoidal blast waves. It is seen that the shock front was sharper than from a typical low order scheme and the algorithm was more robust than a high order scheme. Further, it is seen that energy equivalence is inadequate for defining the shock wave parameters resulting from an ellipsoidal blast source given the dependence upon the initial shape.

Given a volumetric explosion of an ellipsoidal blast source, at given initial conditions, the resulting blast wave on the initially minor axis will be much greater than the explosion of the corresponding spherical source. This would extend through the intermediate region and would cause a ninefold increase in overpressure, a sixfold increase in static impulse, and up to a twentyfold increase in dynamic impulse.

In accidental explosions, where the blast waves are in general weak, asymmetry is an important factor and should be taken into consideration in the assessment of blast damage and risk evaluation. The degree of ellipticity is found to dramatically affect the parameters used for blast damages calculations.

The units of the graphs permit easy scaling to other initial volumes and interpolation to other ellipticities. This scaling does not extrapolate or interpolate to other atmospheres. This unavoidable limitation is due to the inability to determine a priori the work done by the blast front.

Chapter 6

Recommendations for Future Research

A number of recommendations for future research which would improve the data obtained in this study and expand the scope of this study have been noted while completing this study.

First, the computer though powerful has been superceded by much more powerful machines. Though 10,000 grid points were used in the calculation, this represented only 100 grid points along an axis. This is deemed inappropriate as most one dimensional work is presently being analysed using 1000 grid points.

To alleviate this problem, the code could be ported to a large vector processing computer or the new generation RISC computers. This would improve the accuracy especially by decreasing the number of times a particular simulation would have to be re-scaled.

Though much effort was made in finding acceptable high order and low order diffusion equations, not all code be examined. The FCT method is extremely amenable to changes in difference algorithms, both low-order and high-order, which through testing new code may result in greater accuracy for this model.

To generalize the code to examine gas distributions of any shape, the extension to three dimensions should be made. This would provide information into the safety features of irregularly shaped high pressure storage vessels.

For presentation effects, especially with the advent of three dimensional graphics capabilities, the graphs and tables presented in this study could be transfigured into a real time video format. This would provide a dramatic visualization of the effects of a blast wave generated by an accidental explosion.

Lastly, and most importantly, most gas cloud explosions are not volumetric. To provide a complete simulation, the code itself should be extended to non-reactive gases with specific heat ratios different from the ambient air value. Then, after accomplishing this modification, the extension to reactive gas clouds burning in the detonative or deflagrative modes or if confined, subject to a volumetric explosion should be made.

REFERENCES

[1] O.M.F. Elbahar and M.M. Kamel, "Analysis of a Damage Scenario and Potential Hazards of Liquified Gaseous Fuel Carriers in Inland Waterways", International Colloquium on Dynamics of Explosions and Reactive Systems (11th), Warsaw, Poland, (1987).

[2] J. Ribovich, "Blast Hazard of Vapourized Nitromethane", Annals N.Y. Acad. Sci. 152, (1968), 776.

[3] G.J. Piermarini, S. Black and P.J. Miller, "Effects of Pressure on the Thermal Decomposition and Chemical Reactivity of HMX, RDX, and Nitromethane", 19'th International Annual Conference of ICT, 15, (1988).

[4] Wildon Fickett and William C. Davis, "Detonation", University of California press, Berkely, (1979).

[5] B. Zed'dovich and P. Raizer, "Physics of Shock Waves and High-Temperature Hydrodynamic Phenomena"', Academic Press NY,

(1967).

[6] Wilfred E. Baker, "Explosions in Air", University of Texas Press, Austin, (1973).

[7] J. Von Neumann and R.D. Richtmyer, "Journal of Applied Physics", 21, No. 3, (1950), 232.

[8] G.G. Bach and J.H. Lee, "An Analytical Solution for Blast Waves", AIAA, J. 8, (1970), 271.

[9] G.B. Whitham, "On the Propagation of Weak Shock Waves", J. Fluid Mech. 1, Part 3, (1956), 290.

[10] H.L. Brode, "Numerical Solutions of Spherical Blast waves", "Journal of Applied Physics", vol 26, no 6, (1955), 766.

[11] H.L. Brode, "Blast Wave from a Spherical Charge", Vol 2, No. 2, "The Physics of Fluids", (1959), 217.

[12] H.L. Brode, P-582, "The Blast from a Sphere of High Pressure Gas", The RAND Corporation, California, (1955).

[13] Myron N. Plooster, "Shock Waves from Line Sources. Numerical Solutions and Experimental Measurements", Vol 13, No. 11, "The Physics of Fluids", (1970), 2665.

[14] R.D. Richtmyer and K.W.Morton, "Difference Methods for Initial Value Problems", 2nd Edition, Sections 12.9& 13.9, Interscience, New York, (1967).

[15] G.G. Bach, K.W. Chiu, and J.H. Lee, "Contributions to the Propagation of Non-Ideal Blast Waves, I. Far Field Equivalency", 5th Int. Coll., "Gasdynamics of Explosions and Reactive Systems", Bourges, France (1975).

[16] C.M. Guirao, G.G. Bach and J.H.S. Lee, "On the Scaling of Blast Waves from Fuel-Air Explosives", presented at 6'th International Symposium on Military Applications of Blast Simulation, Cahors, France, (1976).

[17] K.W. Chiu, J.H. Lee and R. Knystautas, "The Blast Waves from Asymmetrical Explosions", J. Fluid Mech., 82, (1977), 193.

[18] J. Brossard, S. Hendrickx, J.L. Garnier, A. Lannoy, and J.L. Perrott,

"Air Blast from Unconfined Gaseous Detonations", "Dynamics of Shock Waves, Explosions and Detonations", 9th', American Institute of Aeronautics and Astronautics, Inc, N.Y., (1984).

[19] I.G. Currie, "Fundamental Mechanics of Fluids", McGraw-Hill Inc., (1974).

[20] Lord Raleigh, Proc. Roy Soc. A84, 287, (1910).

[21] G.I. Taylor, Proc. Roy Soc. A84, 371, (1910).

[22] Courant, Friedrichs, and Lewy, Math. Ann. 100, 32, (1928).

[23] Robert D. Richtmyer, "Difference Methods for Initial-Value Problems", Interscience Publishers, Inc., New York, (1957).

[24] K.W. Morton, "Stability and Convergence in Fluid Flow Problems", Proc. Roy. Soc. (London), 4, 323 (1971), 237.

[25] Peter Lax and Burton Wendroff, "Systems for Conservation Laws", "Communications of Pure and Applied Mathematics". Vol. XIII, (1960), 217.

[26] C.K. Chu, "Computational Fluid Dynamics", Colombia University Press, N.Y., N.Y. (1968).

[27] Patrick Roache, "Computational Fluid Dynamics", Albuquerque, Hermose Press, (1976).

[28] F. H. Harlow, "Hydrodynamic Problems Involving Large Fluid Distortions", J. Assoc. Comp., Mach., vol. 4, (1957), 137.

[29] F.W. Vogenitz, G.A. Bird, J.E. Broadwell, and H. Rungaldier, "AIAA Paper 68-6", presented at the AIAA 6th Aerospace Science Meeting, January 22-24, (1968).

[30] A. N. Brooks and T.J.R. Hughes, "Streamline Upwind/Petrov-Galerkin Formulations for Convection Dominated Flows with Particular Emphasis on the Incompressible Navier-Stokes Equations", Computer Methods in Applied Mechanics and Engineering 32, North-Holland Publishing Company, (1982) 199.

[31] J. P. Boris and David L. Book, "Journal of Computational Physics", 11 (1973), 38.

[32] J. P. Boris, David L. Book and K. Hain, "Journal of Computational Physics", 18 (1974), 248.

[33] J. P. Boris and David L. Book, "Journal of Computational Physics", 20 (1975), 397.

[34] S. T. Zalesk, "Journal of Computational Physics", 31 (1979), 335.

[35] S. T. Zalesk, "Advances in Computer Methods for Partial and Differential Equations", 4 (1981), 126.

[36] Heinz-Otto Kreiss, "Numerical Methods for Solving Time-Dependent Problems for Partial Differential Equations", Les Presses de l'Universite de Montreal, Montreal, 1978.

[37] Heinz-Otto Kreiss and Joseph Oliger, "Tellus", XXIV, (1972), 199.

[38] V.V. Rusanov, "Calculation of Interaction of Non-Steady Shock Waves with Obstacles", J. Comp. Math. Math. Phys. USSR, No. 2, (1962).

[40] Antoni K. Oppenheim,"Introduction to Gasdynamics of Explosions",

Springer-Verlag, New York, (1970).

[41] S.R. Brinkley and J.G. Kirkwood, "Theory of the Propagation of Shock Waves", Phys. Rev., 71, (1947), 606.

[42] R. Courant and K.O. Friedrichs, "Supersonic Flow and Shock Waves", Interscience Publishers, Inc., New York, (1948).

[43] Y. Kurihara, Mon. Weather Rev. 93 (1965), 33.

[44] A.K. Oppenheim, J. Kurylo, L.M. Cohen, and M.M. Kamel, "Proceedings of the 11th International Symposium on Shock Tubes and Waves", (1978), 465.

[45] J. Crank and P. Nicholson, "A Practical Method for Numerical Integration of Solutions of Partial Differential Equations of Heat Conduction Type", Proc Cambridge Philos. Soc. 43 (1947), 50.

Time Step	Time (seconds)
0	0.000000D+00
10	0.201691D-03
20	0.364892D-03
30	0.519790D-03
40	0.671185D-03
50	0.821813D-03
60	0.974314D-03
70	0.112982D-02
80	0.128771D-02
90	0.144745D-02
100	0.160860D-02
110	0.177112D-02
120	0.210198D-02
130	0.243532D-02
140	0.277311D-02
150	0.311572D-02
160	0.346362D-02
170	0.381765D-02
180	0.417842D-02
190	0.454578D-02
200	0.491977D-02
210	0.530070D-02
220	0.568877D-02
230	0.650150D-02
240	0.734490D-02
250	0.821485D-02
260	0.910947D-02
270	0.100280D-01
280	0.109696D-01
290	0.119322D-01
300	0.129152D-01
310	0.149797D-01
320	0.171232D-01
330	0.193186D-01
340	0.215563D-01
350	0.238311D-01
360	0.261383D-01
370	0.284749D-01
380	0.308378D-01

Table 4.2.1-1 Time for Each Time Step, P=19, E11=3

Time Step	Time (seconds)
0	0.000000D+00
1	0.366600D-04
2	0.573330D-04
3	0.777211D-04
4	0.971906D-04
5	0.115441D-03
20	0.360665D-03
50	0.841642D-03
100	0.168975D-02
150	0.316176D-02
200	0.514811D-02
250	0.821293D-02
300	0.130513D-01
319	0.150027D-01
320	0.151069D-01

Table 4.2.2-1 Time for Each Time Step, $\Delta P = 19$, E11 = 1.5

Time Step	Time (seconds)
0	0.000000D+00
1	0.366600D-04
2	0.573349D-04
3	0.781392D-04
4	0.977115D-04
5	0.116637D-03
20	0.363083D-03
50	0.810056D-03
100	0.234890D-02
150	0.393928D-02
200	0.607365D-02
250	0.102905D-01
299	0.140011D-01
300	0.141002D-01

Table 4.2.3-1 Time for Each Time Step, ΔP = 19, Ell = 10

Time Step	Time (seconds)
0	0.000000D+00
1	0.366600D-04
2	0.573330D-04
3	0.777210D-04
4	0.971909D-04
5	0.115442D-03
20	0.362125D-03
30	0.857229D-03
100	0.175326D-02
150	0.311510D-02
200	0.521552D-02
250	0.940509D-02
300	0.144761D-01

Table 4.2.4-1 Time for Each Time Step, ΔP = 19, Ell = 1

Time Step	Time (seconds)
0	0.000000D+00
1	0.366600D-04
2	0.592301D-04
3	0.814743D-04
4	0.102320D-03
5	0.122327D-03
20	0.407026D-03
50	0.945454D-03
100	0.188034D-02
150	0.305817D-02
200	0.515161D-02
250	0.744357D-02
300	0.126724D-01
350	0.195579D-01
400	0.320204D-01
429	0.394969D-01
430	0.397567D-01

Table 4.3.1-1 Time for Given Time Step, $\Delta P = 8$, Ell = 3

Time Step	Time (seconds)
0	0.000000D+00
1	0.366600D-04
2	0.592301D-04
3	0.814743D-04
4	0.102320D-03
5	0.122326D-03
20	0.405747D-03
50	0.973127D-03
100	0.197721D-02
150	0.326647D-02
200	0.557645D-02
250	0.911630D-02
300	0.146402D-01
350	0.229912D-01
400	0.356715D-01
429	0.432150D-01
430	0.434771D-01

Table 4.3.2-1 Time for Given Time Step, ΔP = 8, Ell = 1.5

Time Step	Time (seconds)
0	0.000000D+00
1	0.366600D-04
2	0.592301D-04
3	0.814744D-04
4	0.102763D-03
5	0.123321D-03
20	0.402900D-03
50	0.931212D-03
100	0.275922D-02
150	0.468103D-02
200	0.728224D-02
250	0.123236D-01
300	0.202708D-01
350	0.326559D-01
379	0.400887D-01
380	0.403475D-01

Table 4.3.3-1 Time for Given Time Step, ΔP = 8, Ell = 10

Time Step	Time (seconds)
0	0.000000D+00
1	0.366600D-04
2	0.592304D-04
3	0.814746D-04
4	0.102320D-03
5	0.122327D-03
20	0.408262D-03
50	0.993686D-03
100	0.205132D-02
150	0.317732D-02
200	0.560640D-02
250	0.872977D-02
300	0.143583D-01
350	0.227760D-01
400	0.354820D-01
419	0.404156D-01
420	0.406765D-01

Table 4.3.4-1 Time for Given Time Step, $\Delta P = 8$, $E11 = 1$

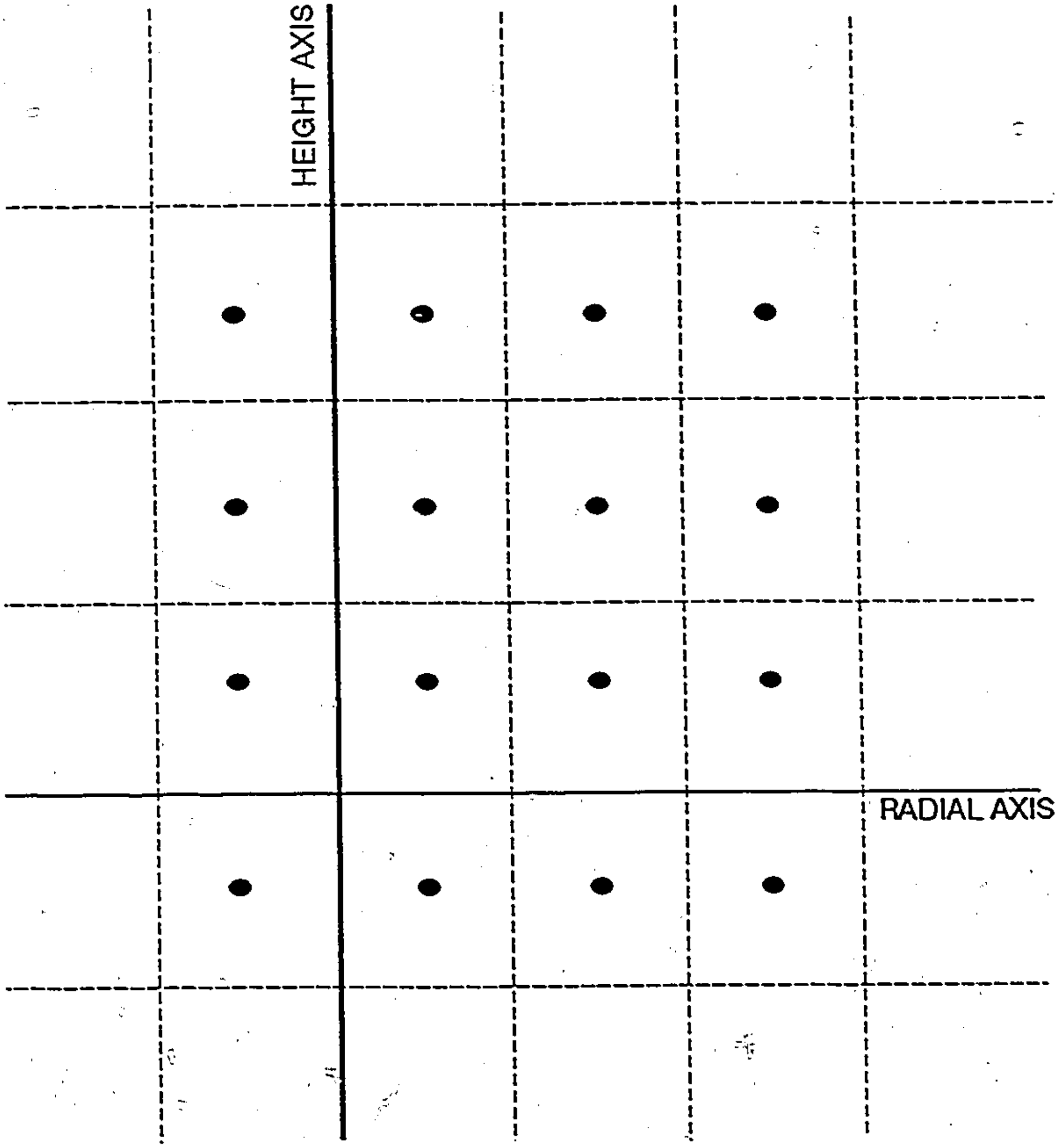

Figure 3.5-1 The Grid Mapping

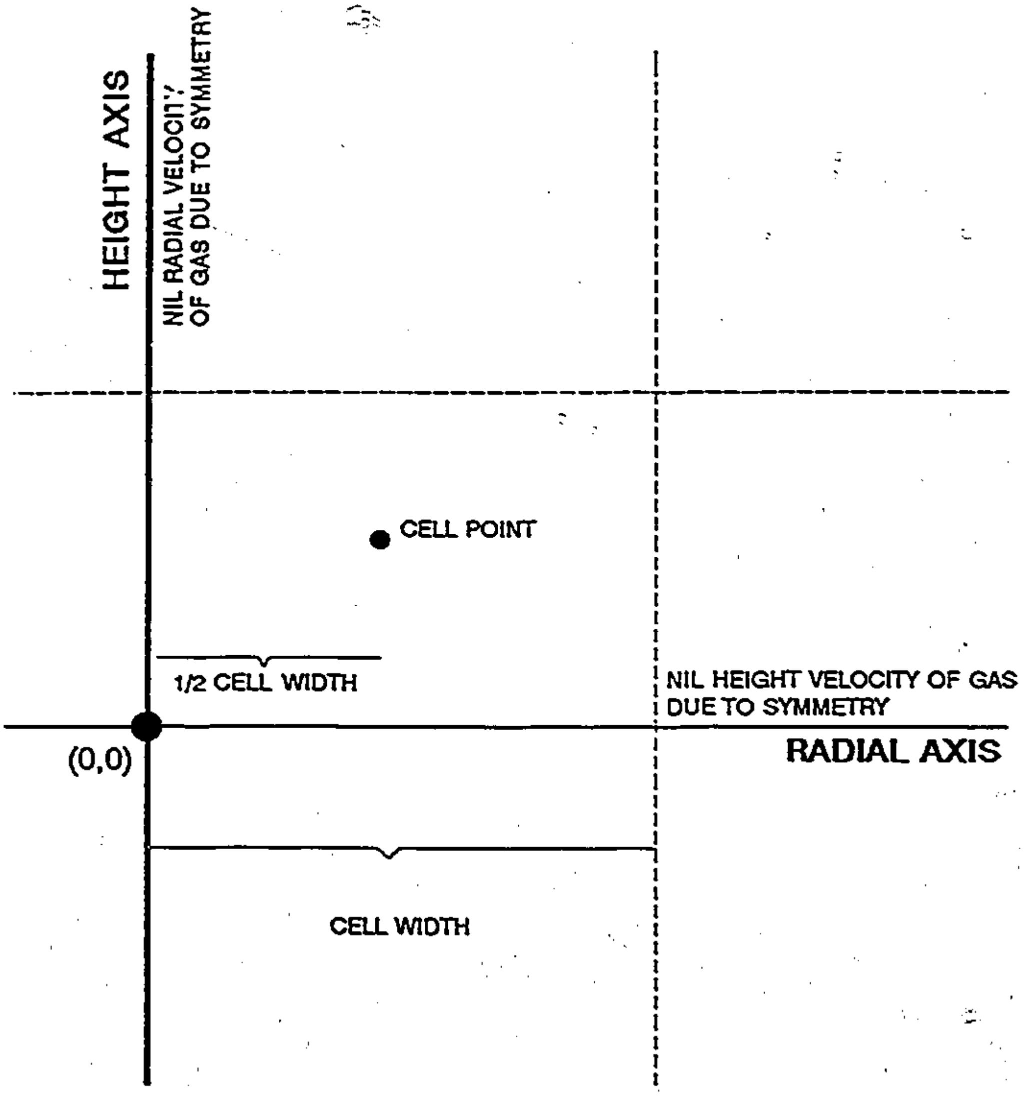

Figure 3.5-2 Cell Structure

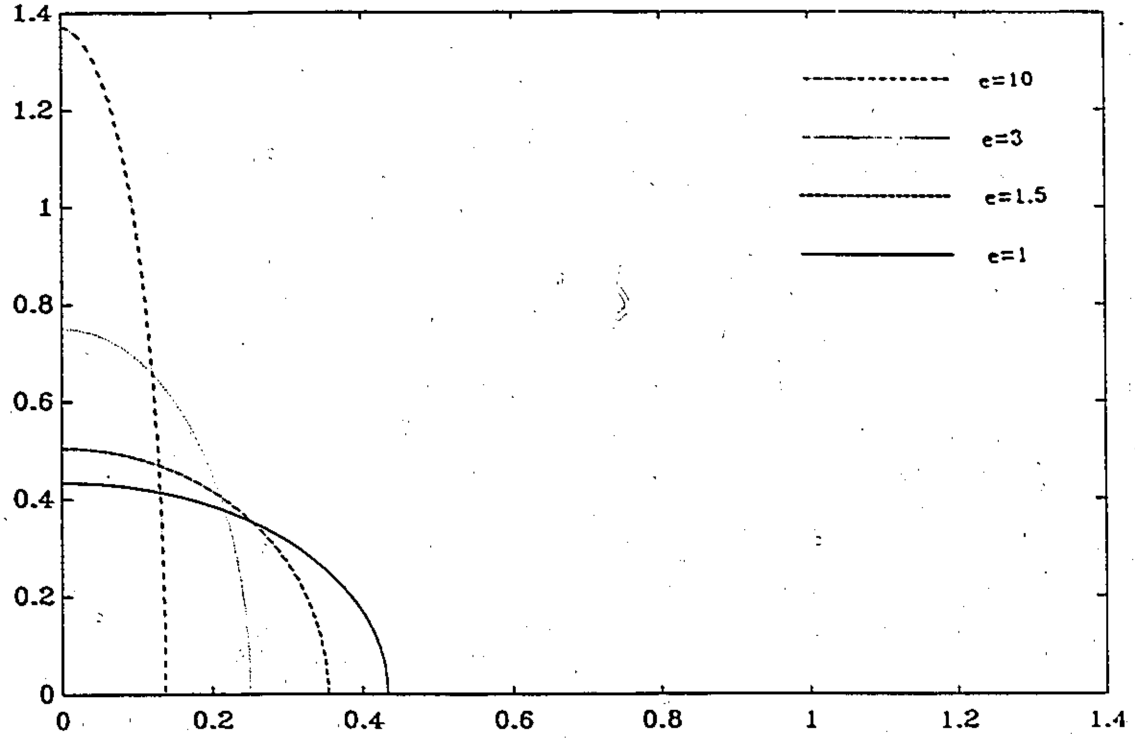

Figure 4.2-1 Comparison of Ellipsoids

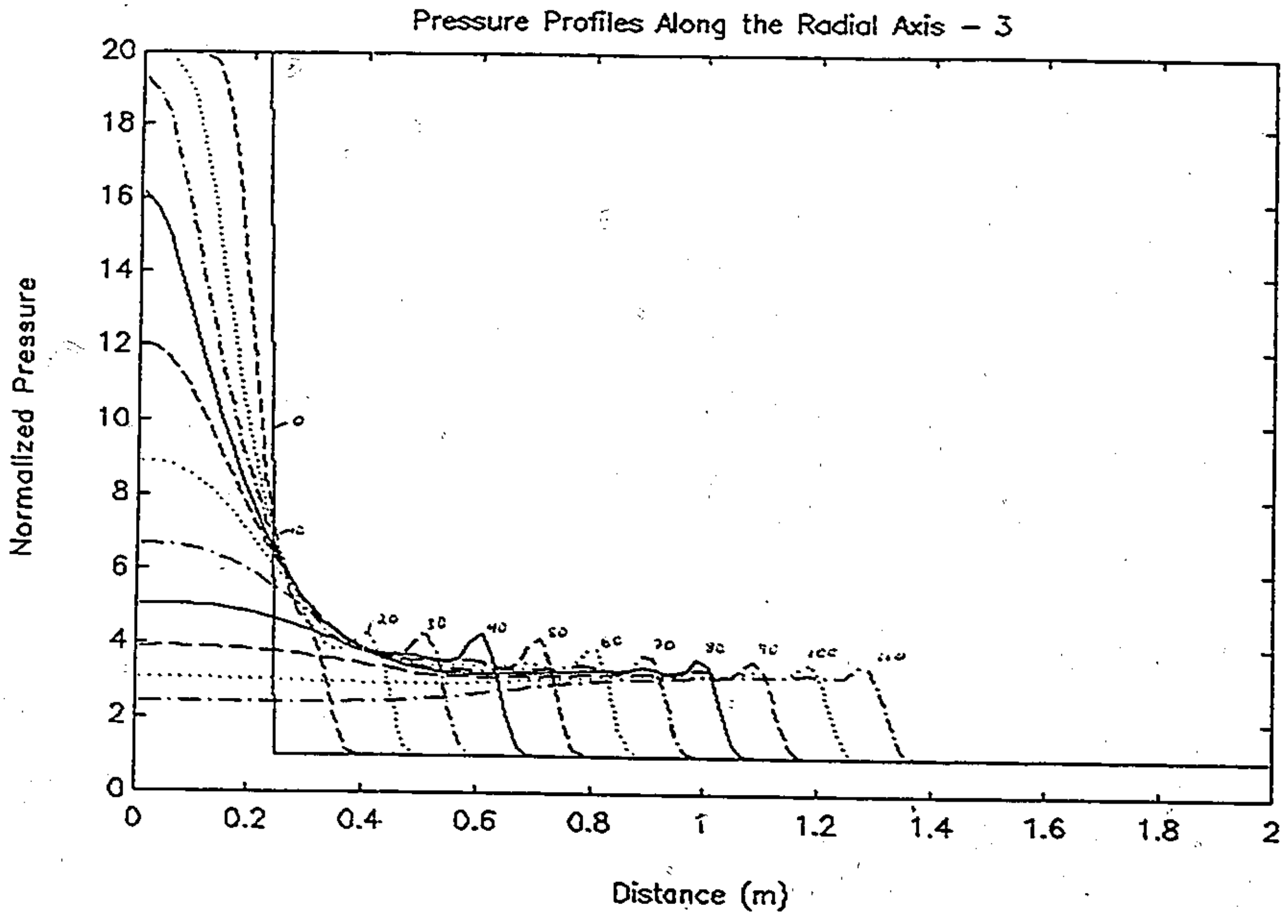

Figure 4.2.1-1 Radial Pressure Profiles, ΔP = 19, E11 = 3, Scale = 1, a

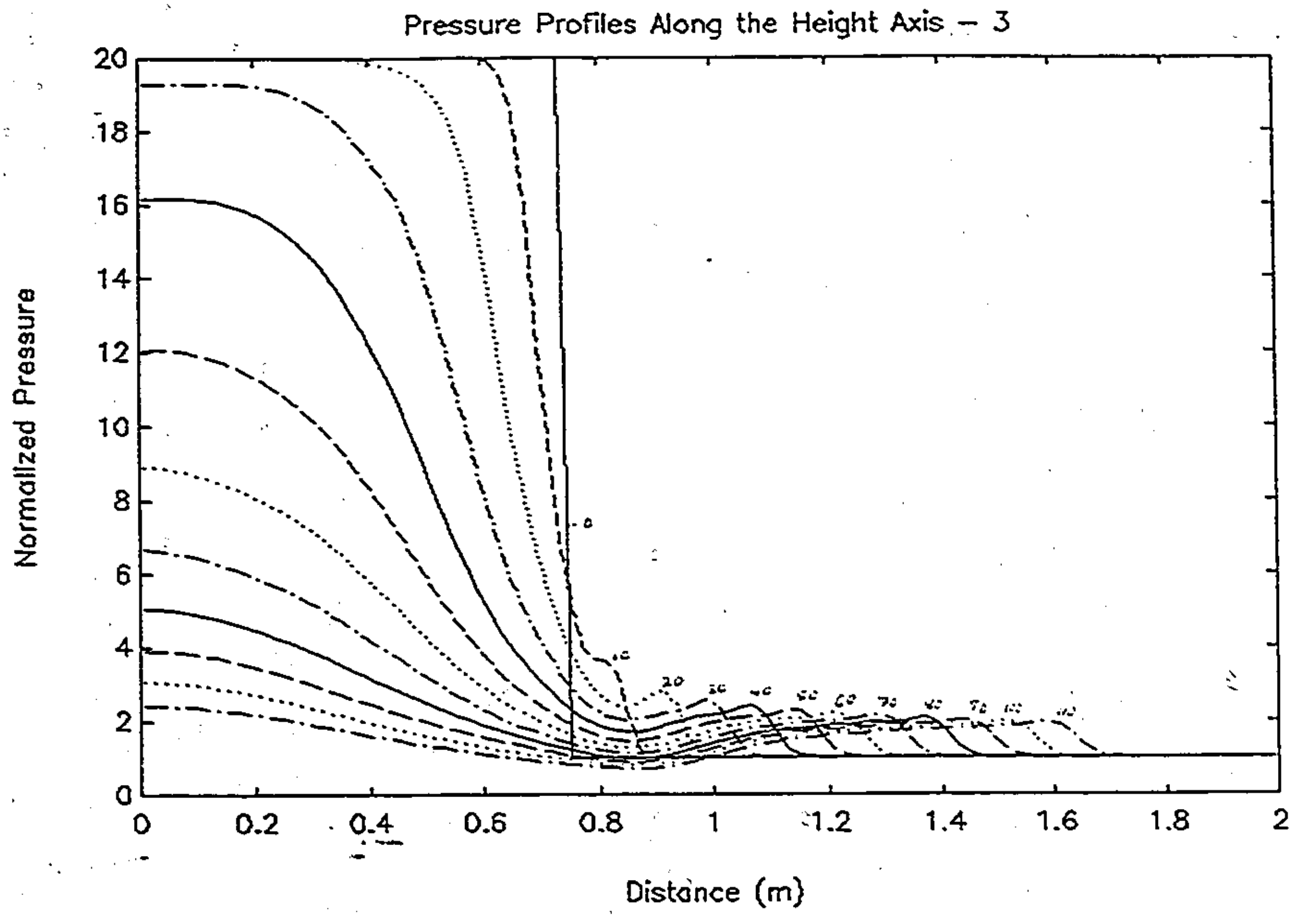

Figure 4.2.1-2 Height Pressure Profiles, ΔP = 19, E11 = 3, Scale = 1, a

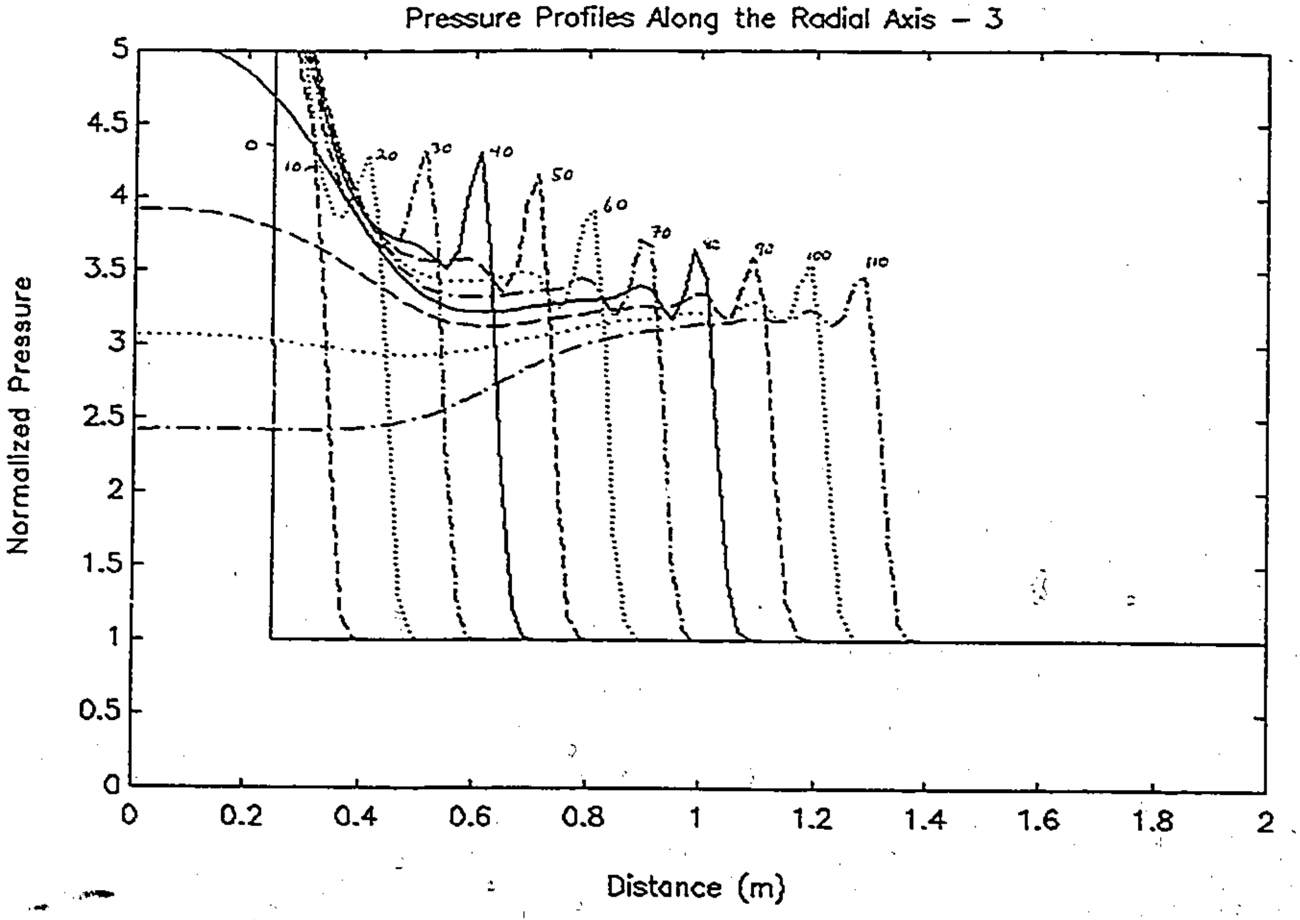

Figure 4.2.1-3 Radial Pressure Profiles, ΔP = 19, E11 = 3, Scale = 1, b

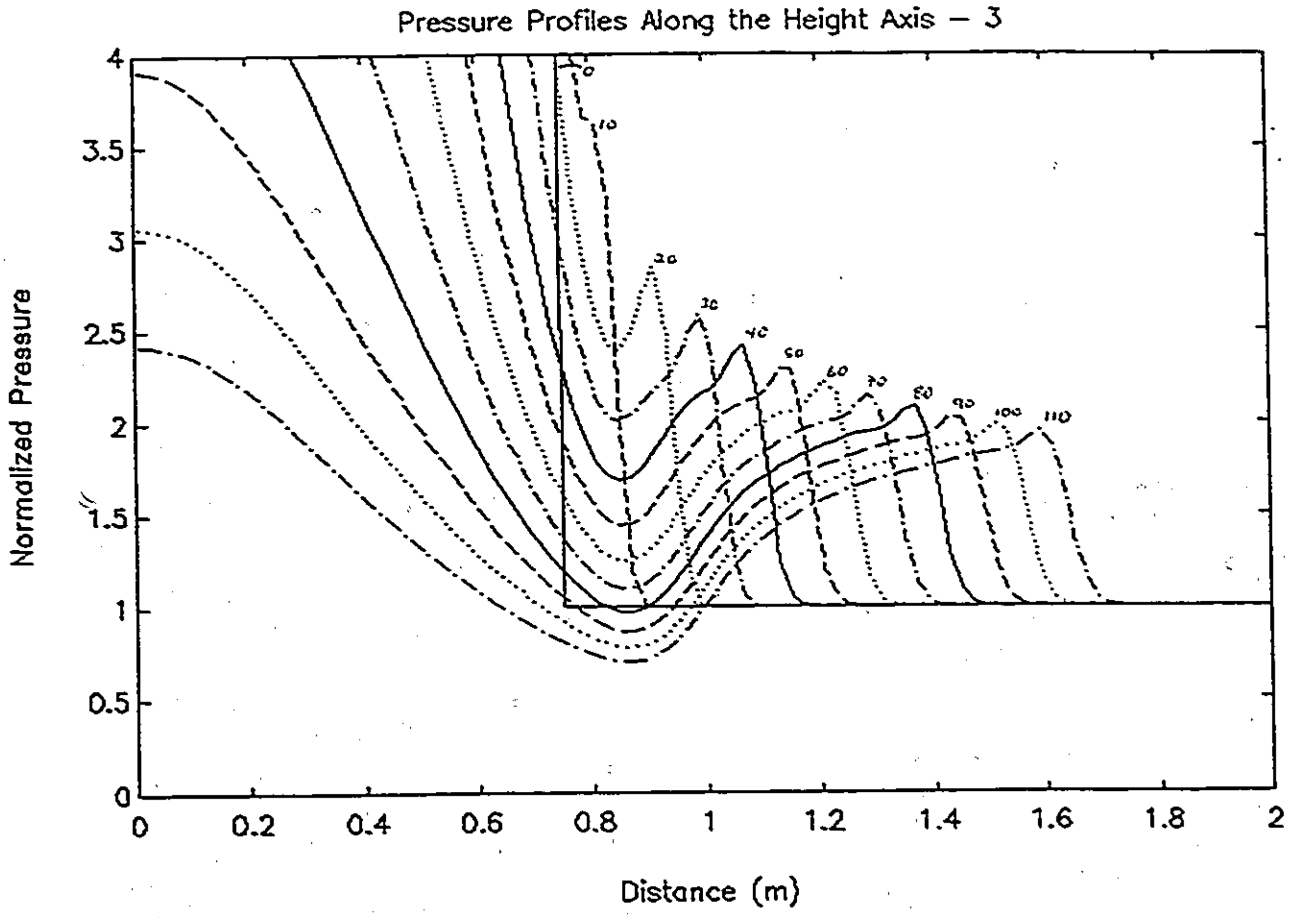

Figure 4.2.1-4 Height Pressure Profiles, ΔP = 19, Ell = 3, Scale = 1, b

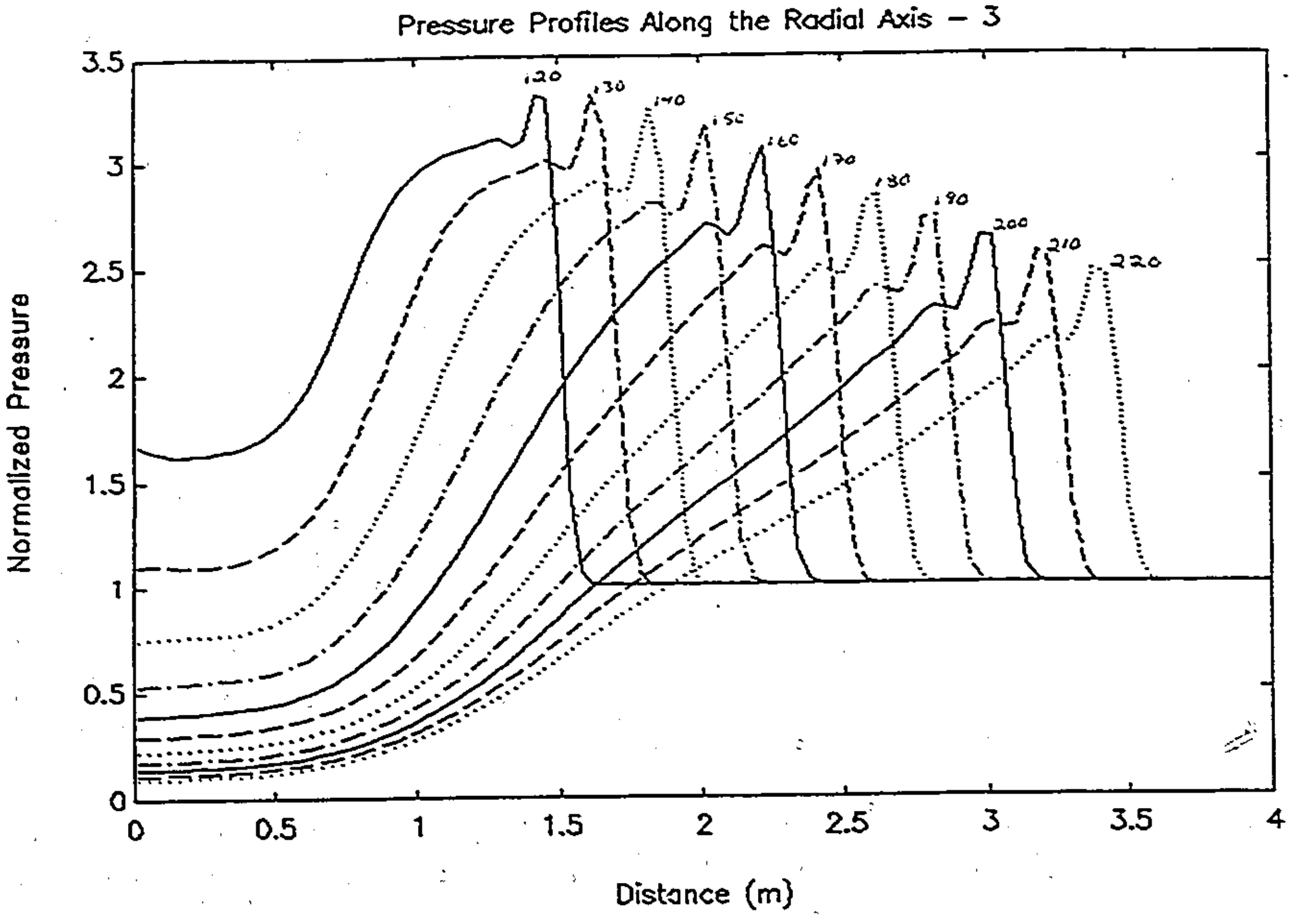

Figure 4.2.1-5 Radial Pressure Profiles, ΔP = 19, Ell = 3, Scale = 2

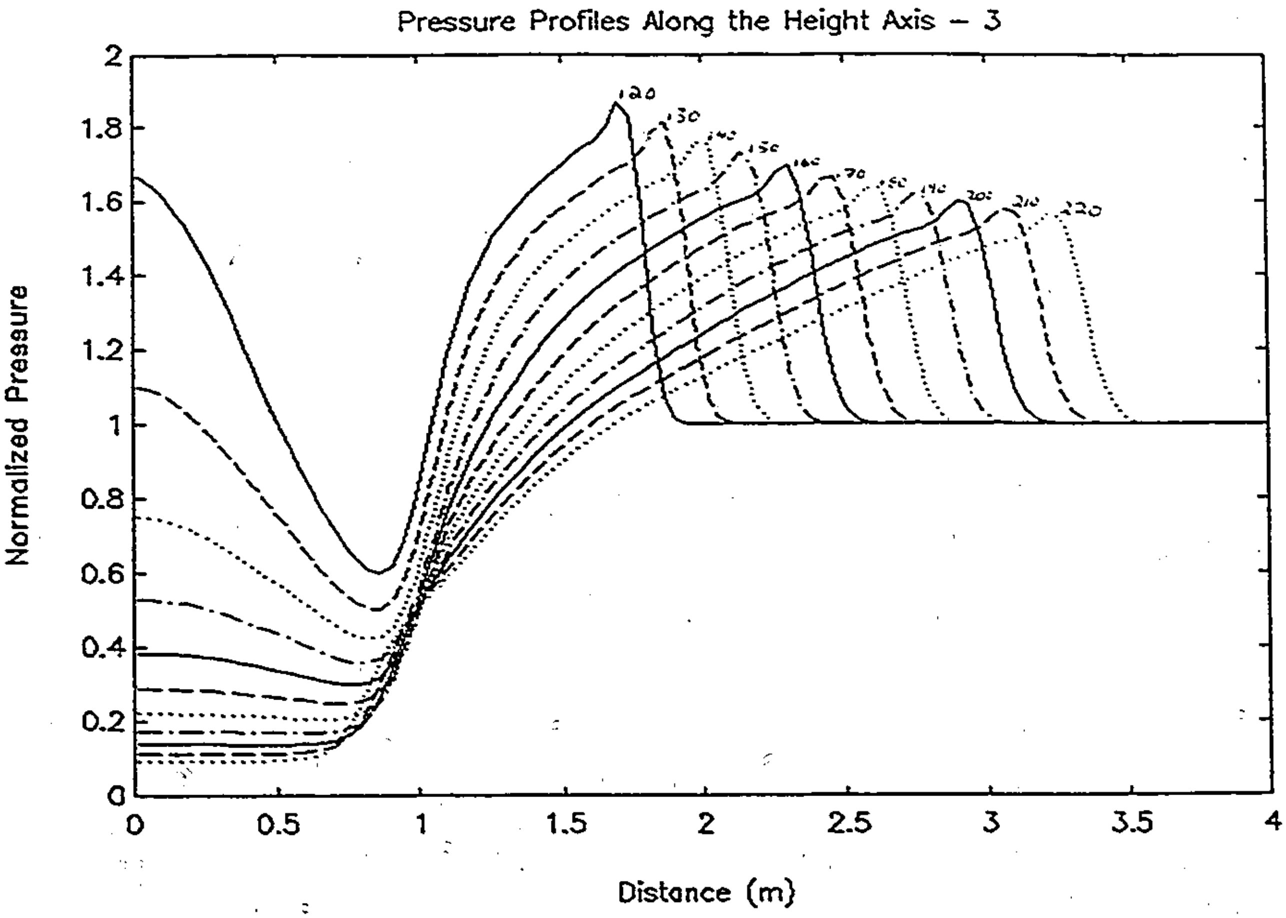

Figure 4.2.1-6 Height Pressure Profiles, ΔP = 19, E11 = 3, Scale = 2

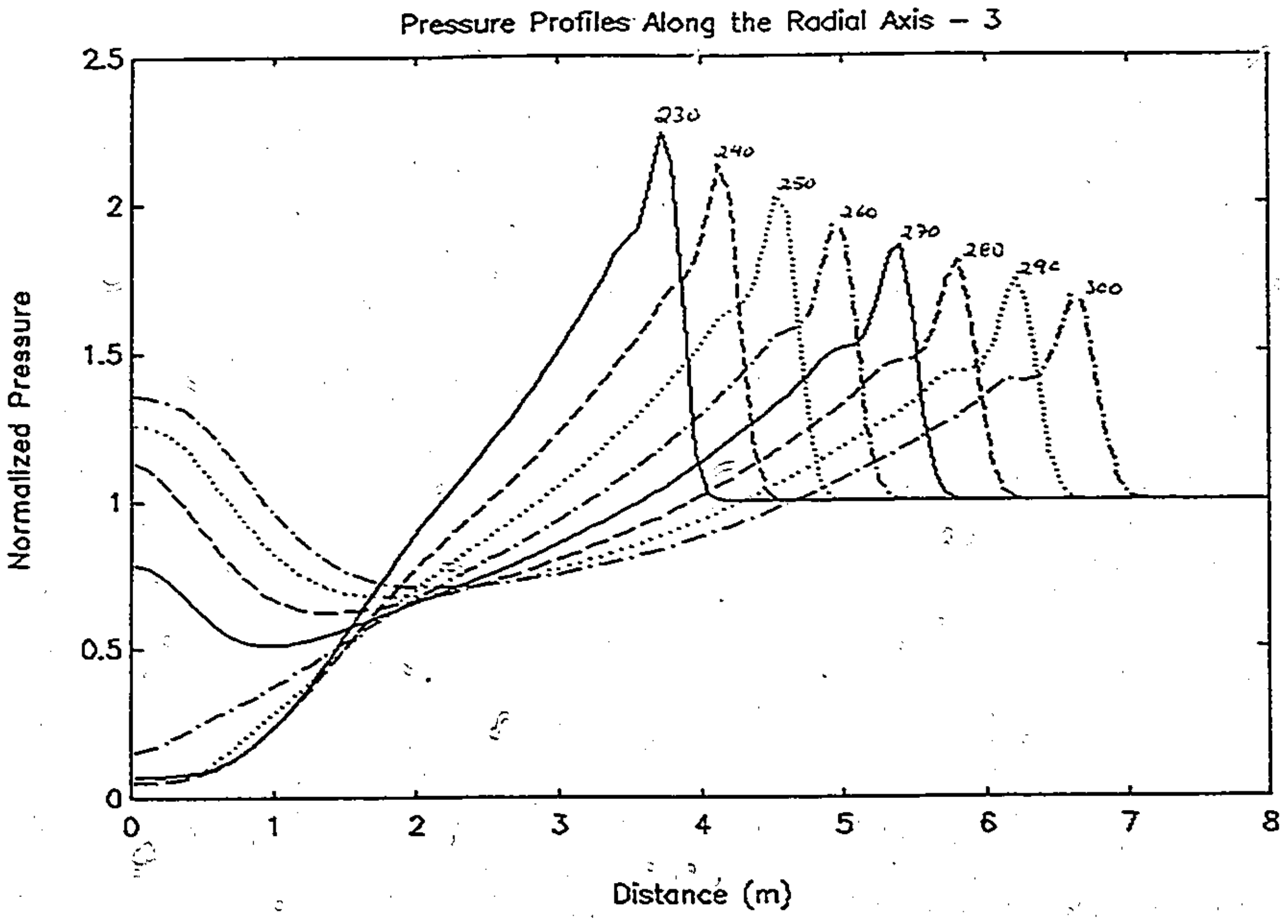

Figure 4.2.1-7 Radial Pressure Profiles, ΔP = 19, Ell = 3, Scale = 3

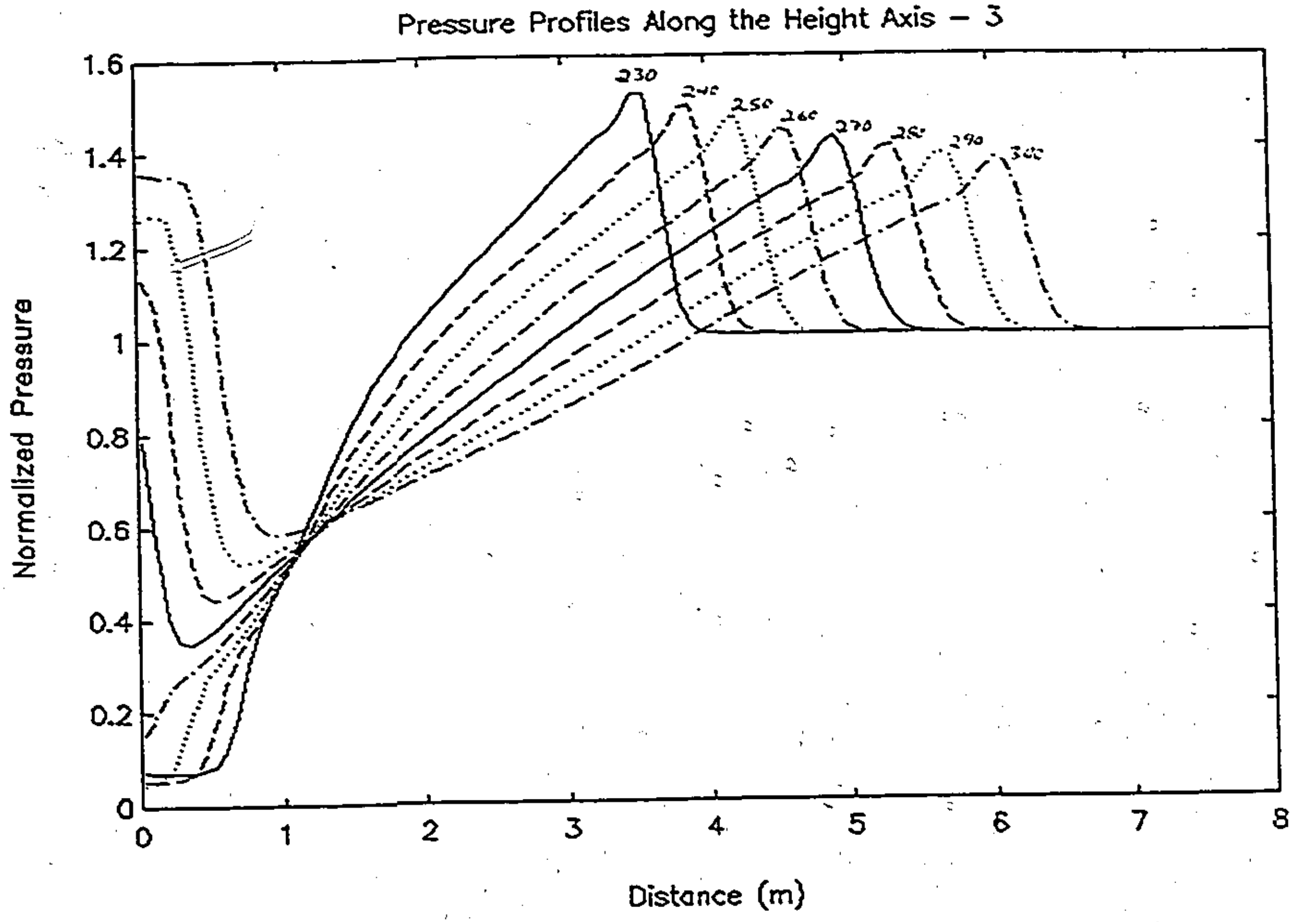

Figure 4.2.1-8 Height Pressure Profiles, ΔP = 19, Ell = 3, Scale = 3

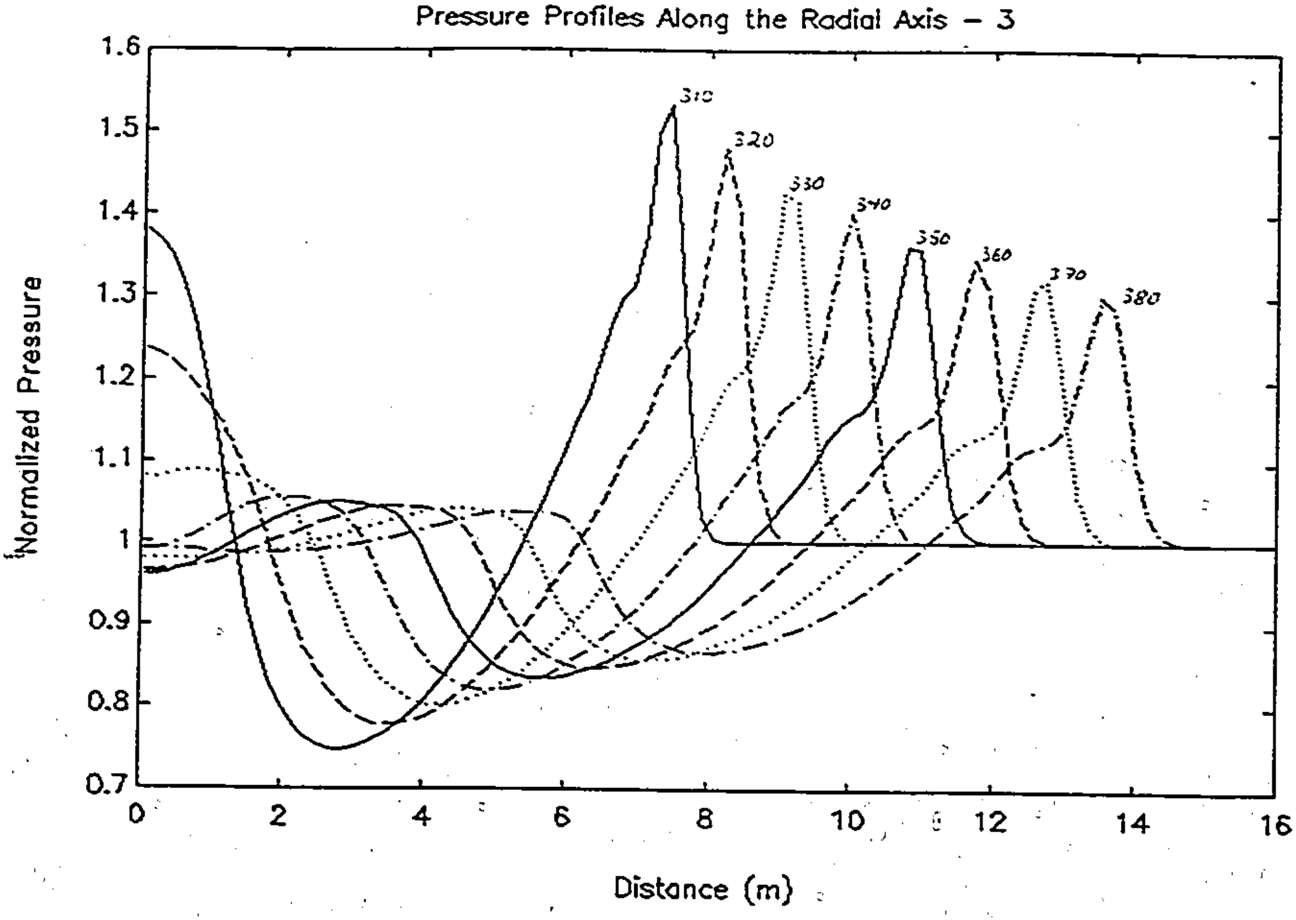

Figure 4.2.1-9 Radial Pressure Profiles, ΔP = 19, Ell = 3, Scale = 4

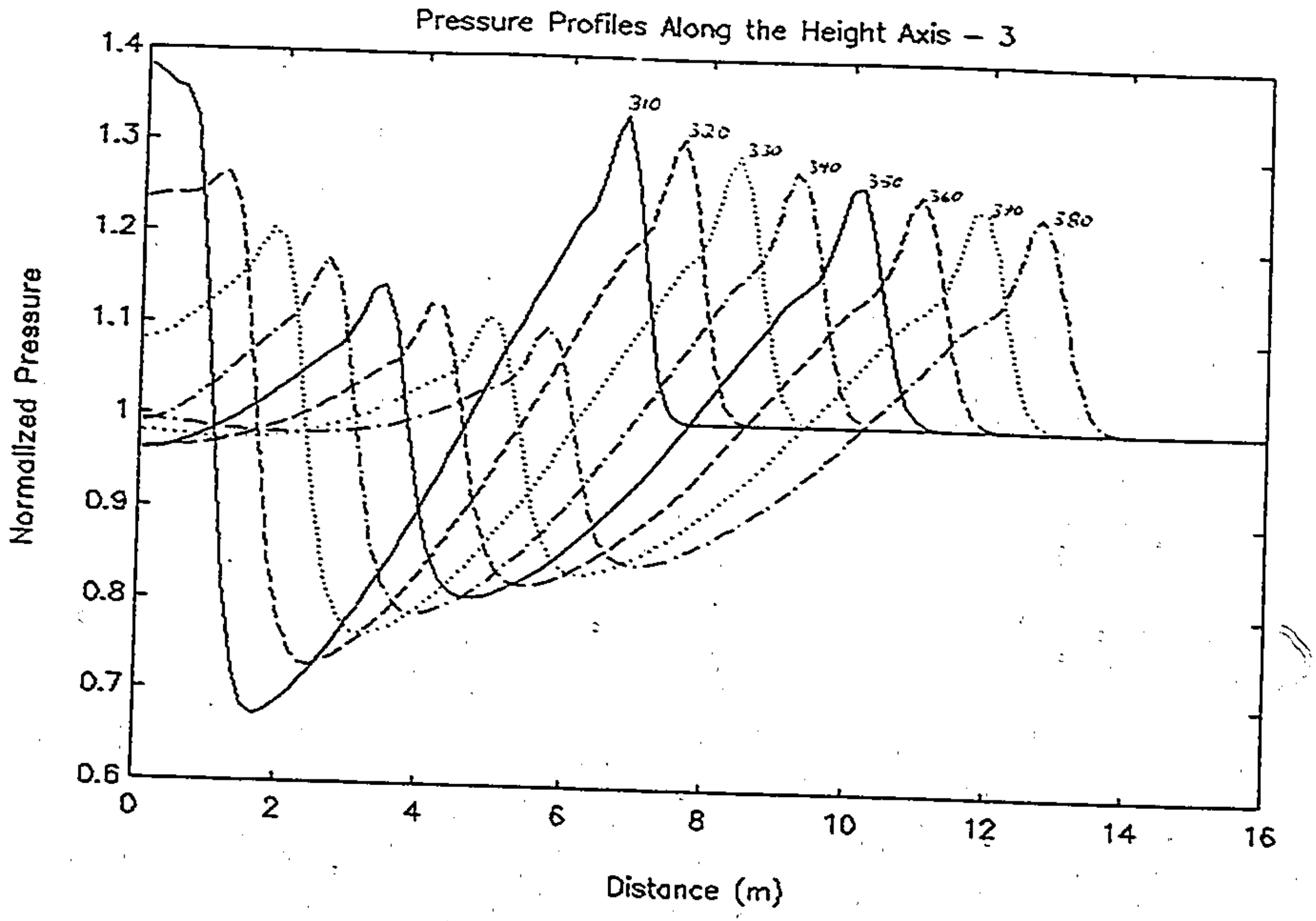

Figure 4.2.1-10 Height Pressure Profiles, ΔP = 19, Ell = 3, Scale = 4

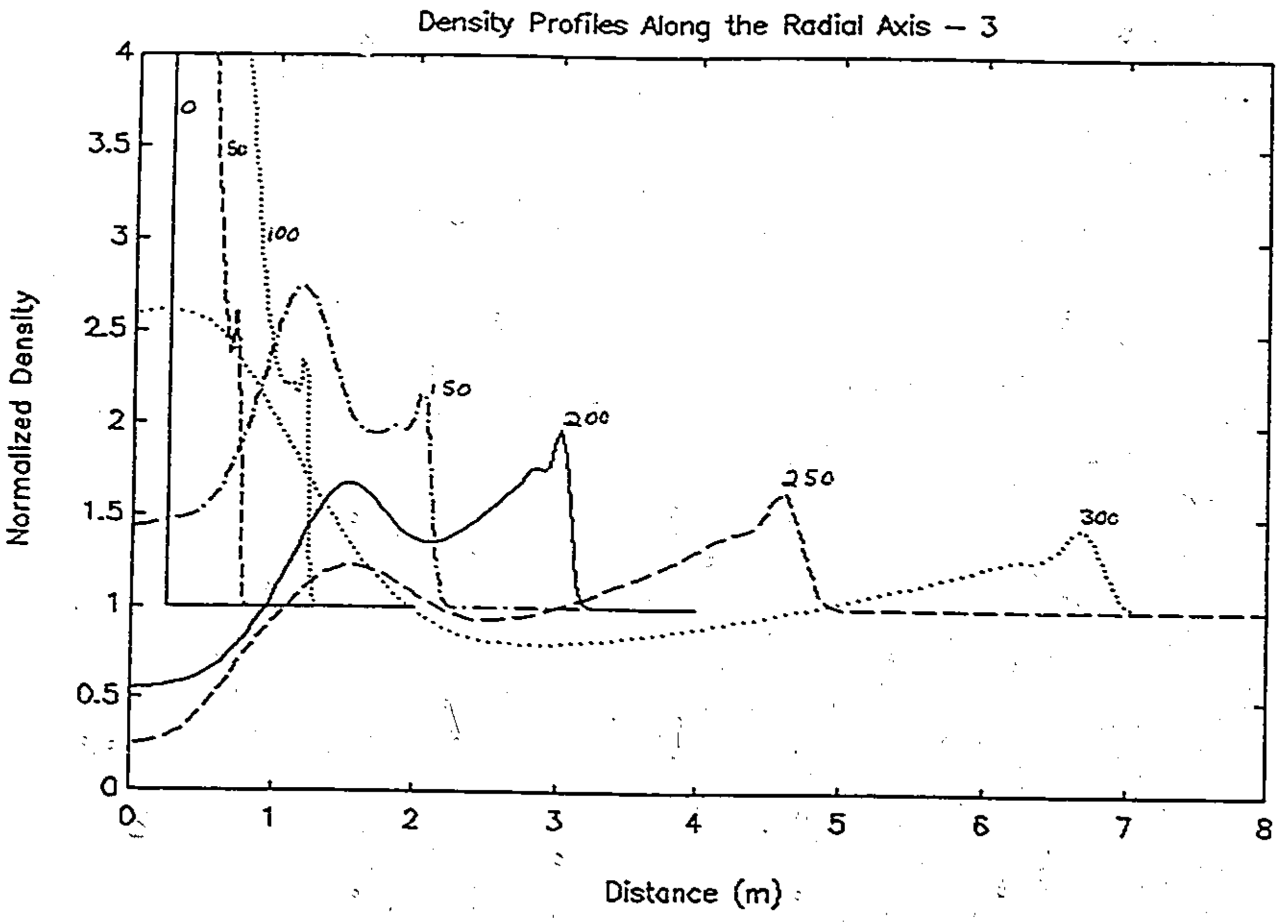

Figure 4.2.1-11 Radial Density Profiles, ΔP = 19, Ell = 3

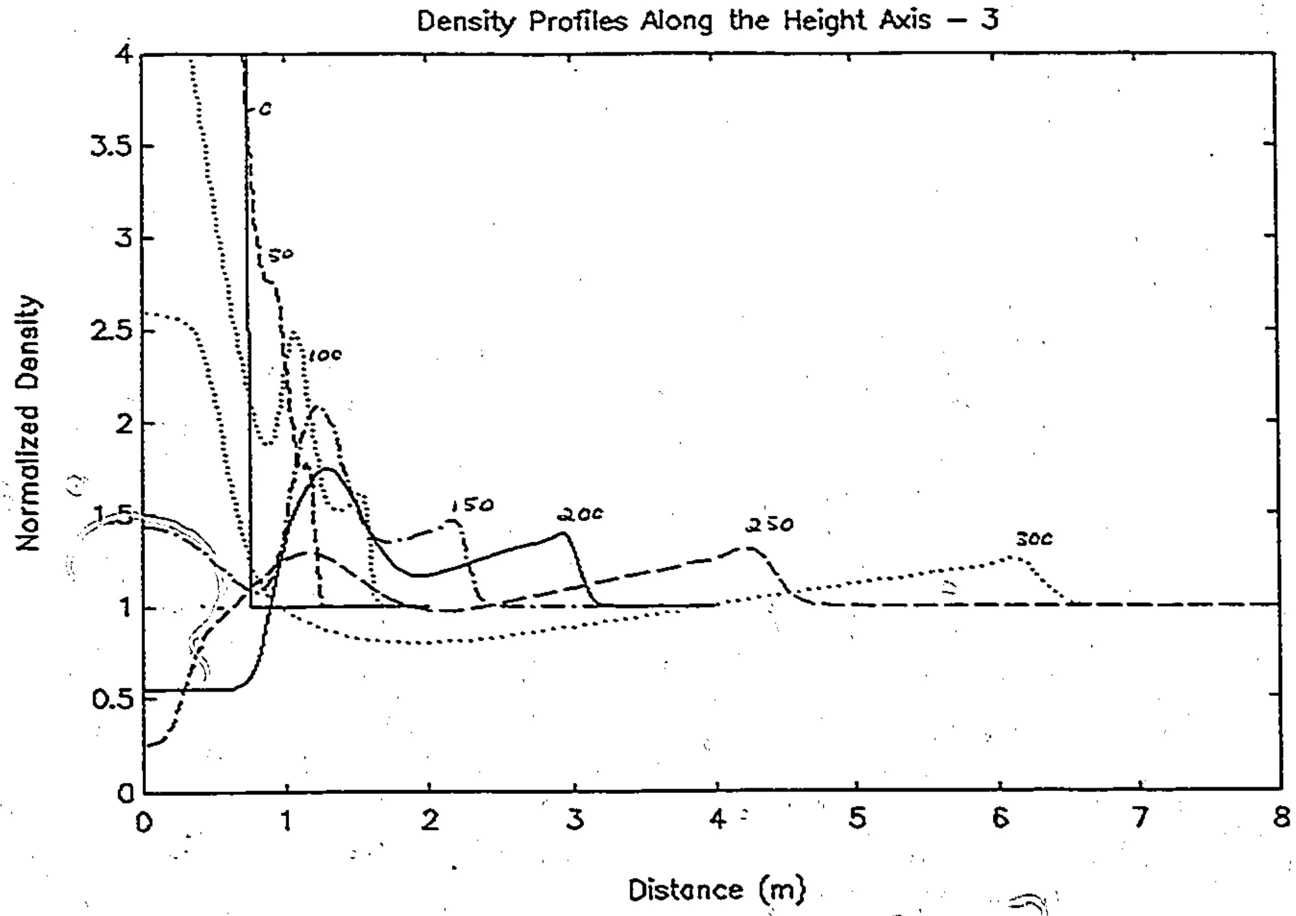

Figure 4.2.1-12 Height Density Profiles, ΔP = 19, Ell = 3

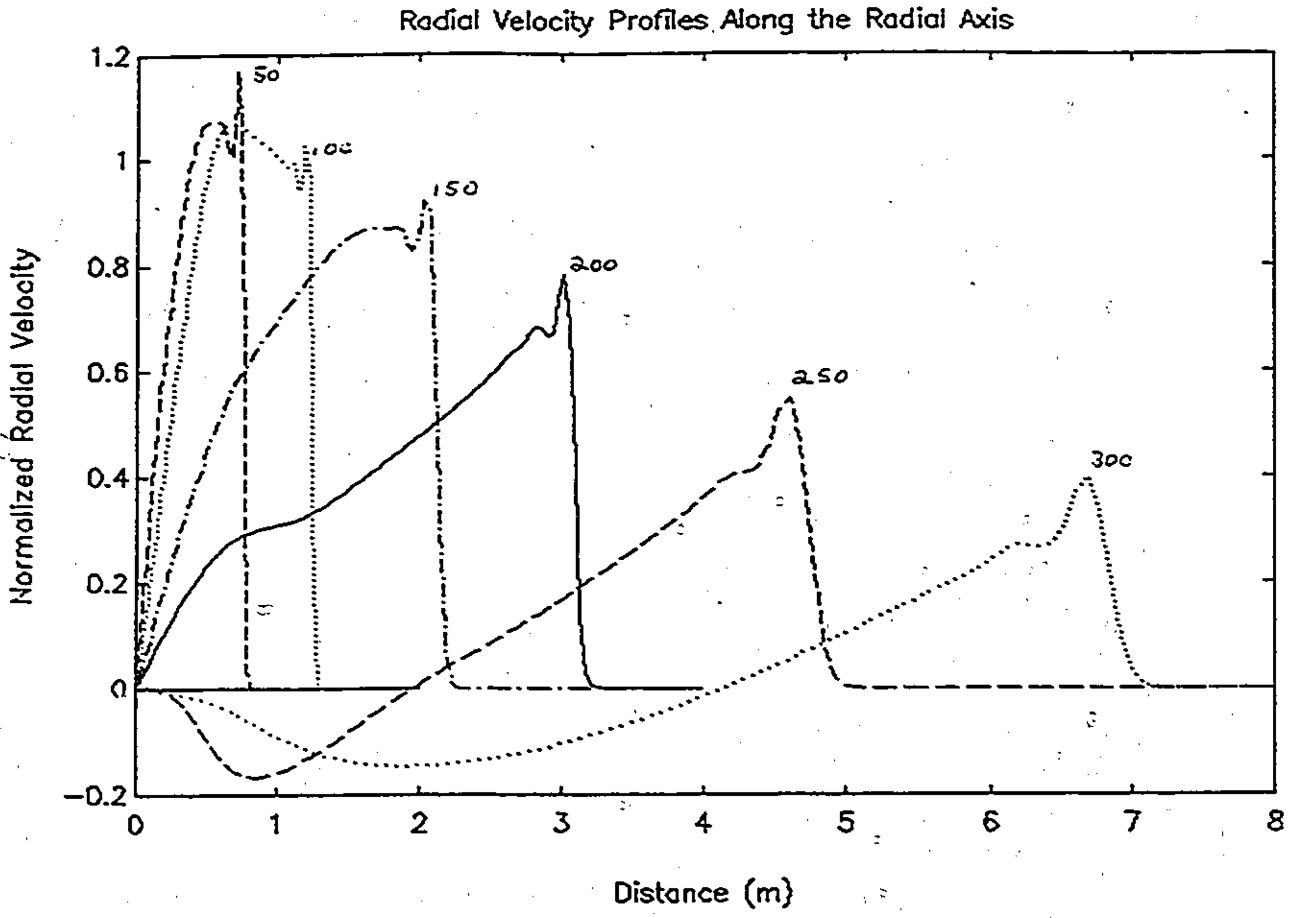

Figure 4.2.1-13 Radial Velocity Radial Profiles, ΔP = 19, Ell = 3

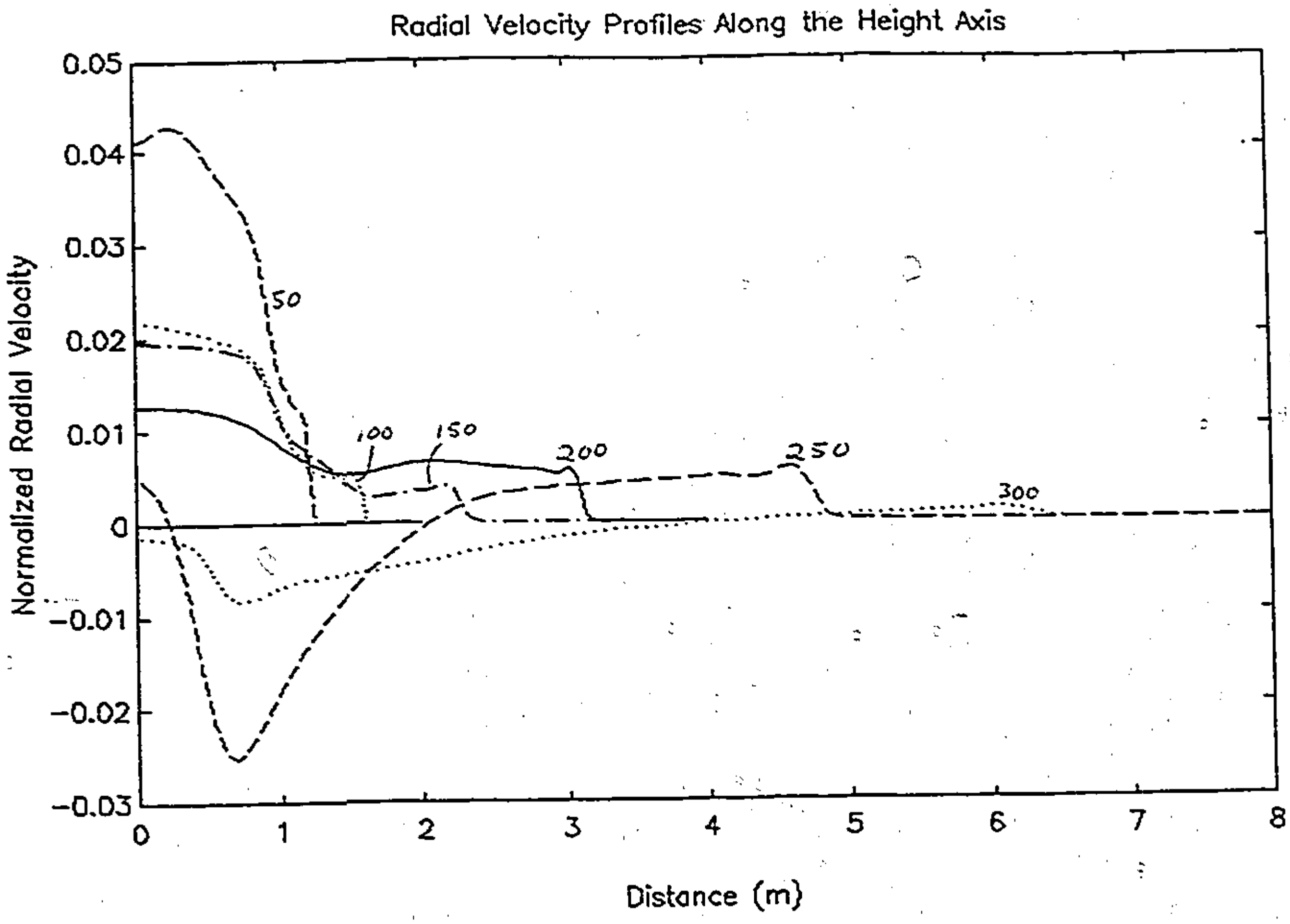

Figure 4.2.1-14 Radial Velocity Height Profiles, ΔP = 19, Ell = 3

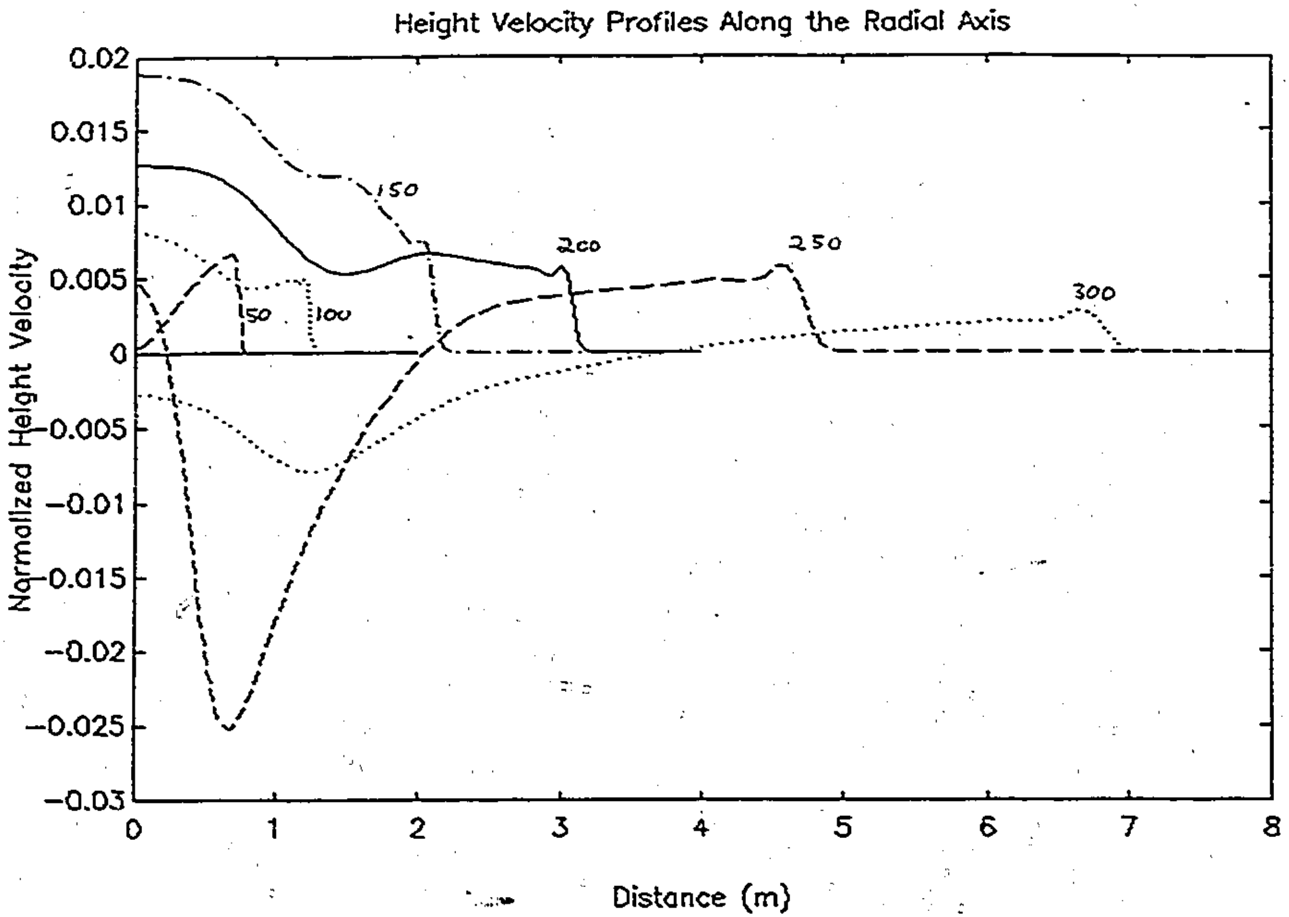

Figure 4.2.1-15 Height Velocity Radial Profiles, ΔP = 19, E11 = 3

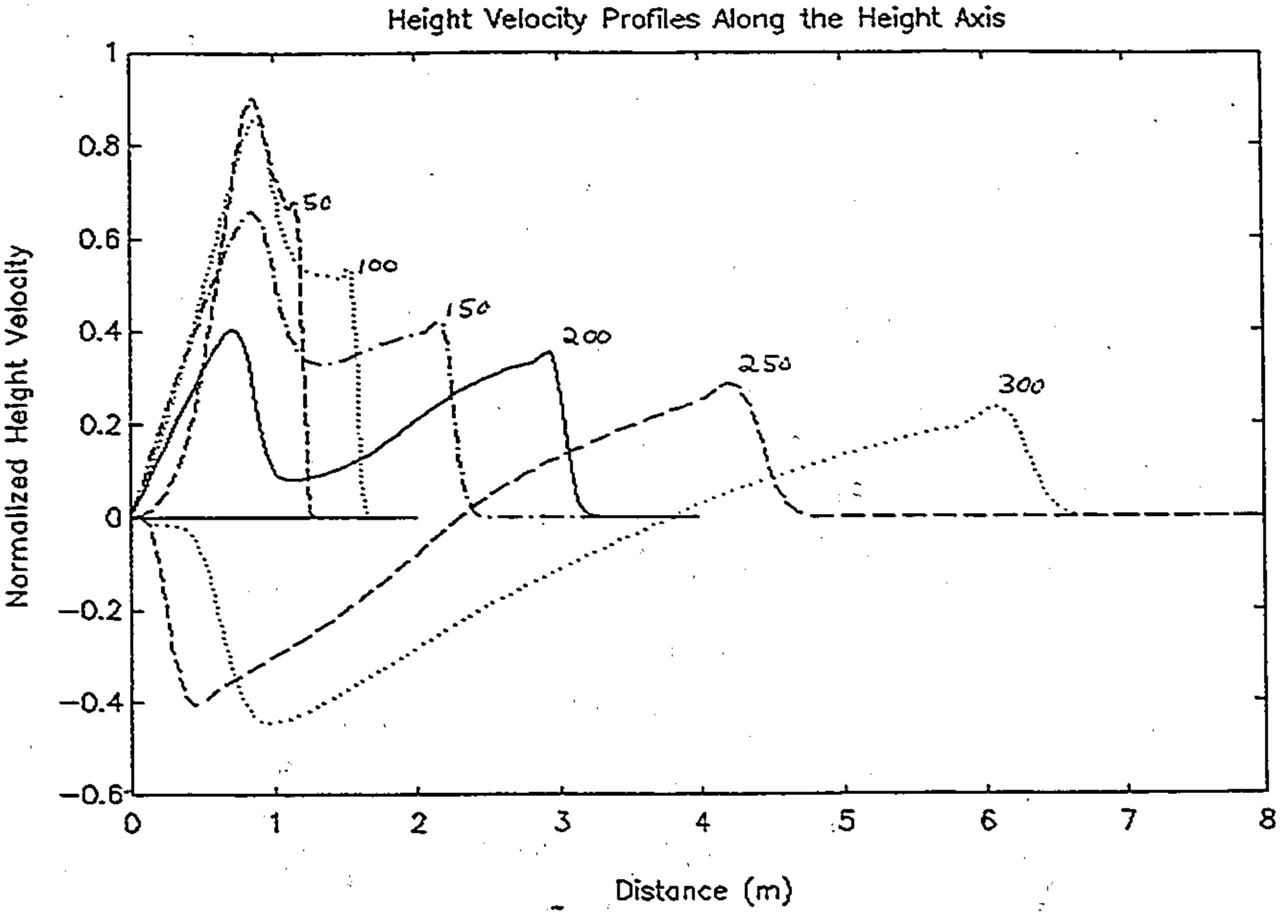

Figure 4.2.1-16 Height Velocity Height Profiles, ΔP = 19, E11 = 3

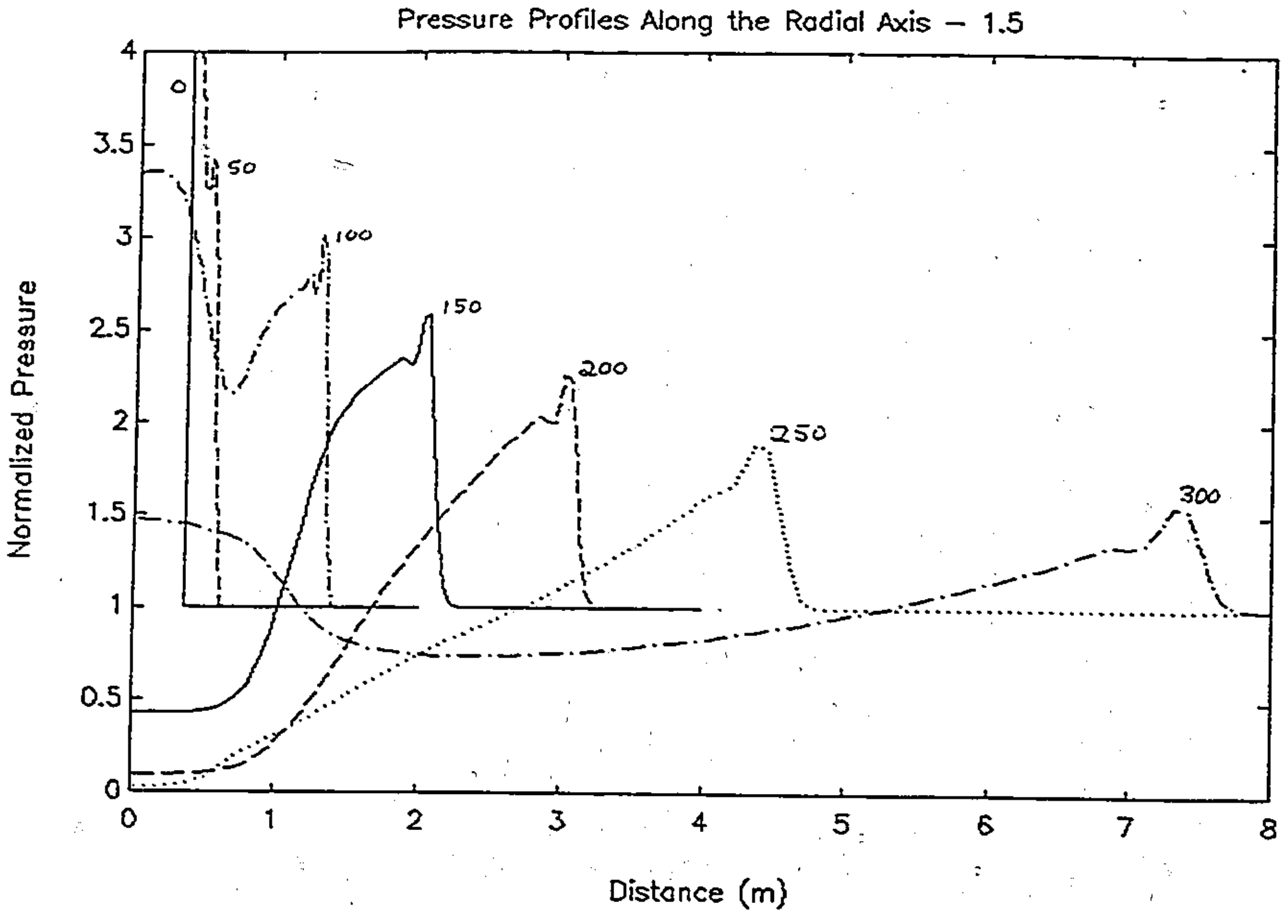

Figure 4.2.2-1 Pressure Radial Profiles, ΔP = 19, Ell = 1.5

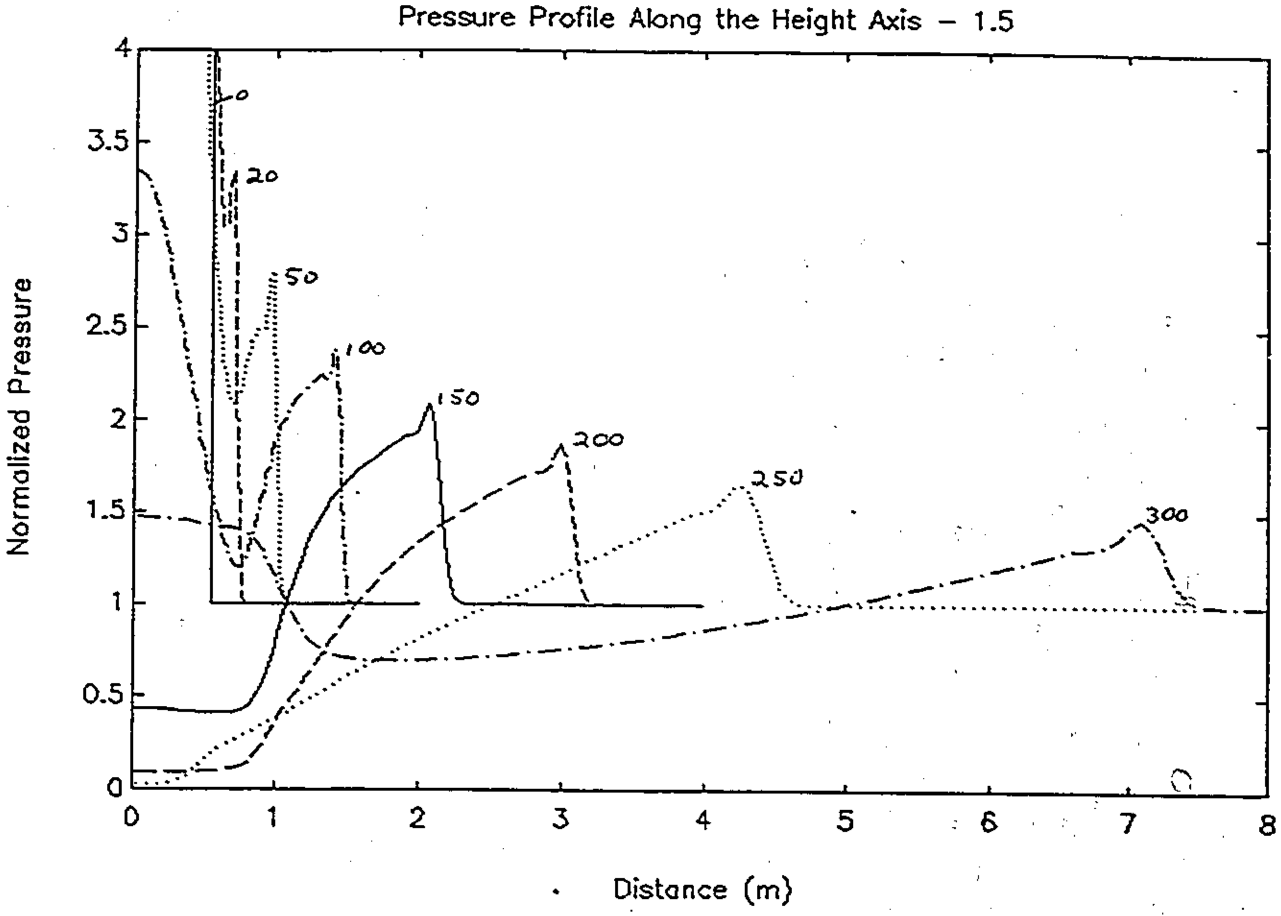

Figure 4.2.2-2 Pressure Height Profiles, ΔP = 19, E11 = 1.5

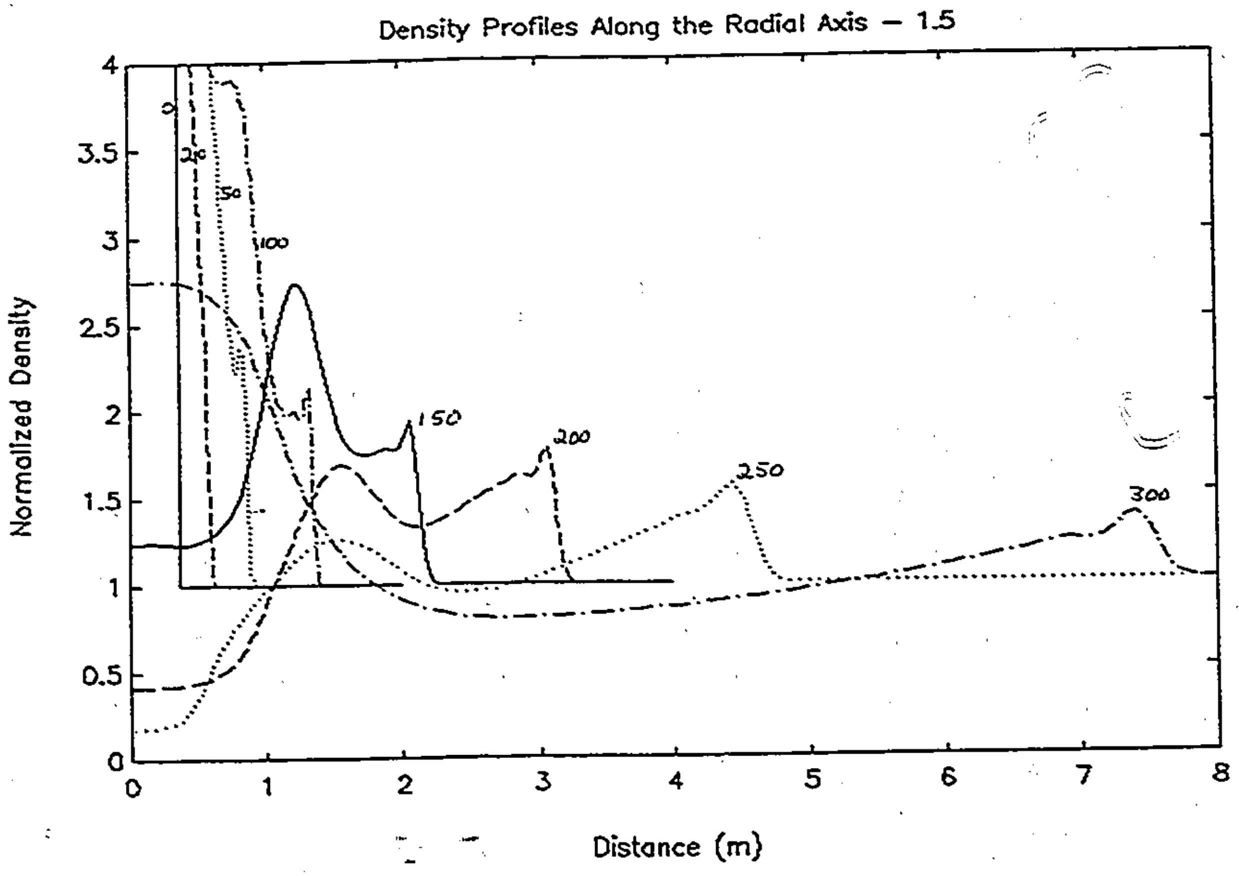

Figure 4.2.2-3 Radial Density Profiles, ΔP = 19, Ell = 1.5

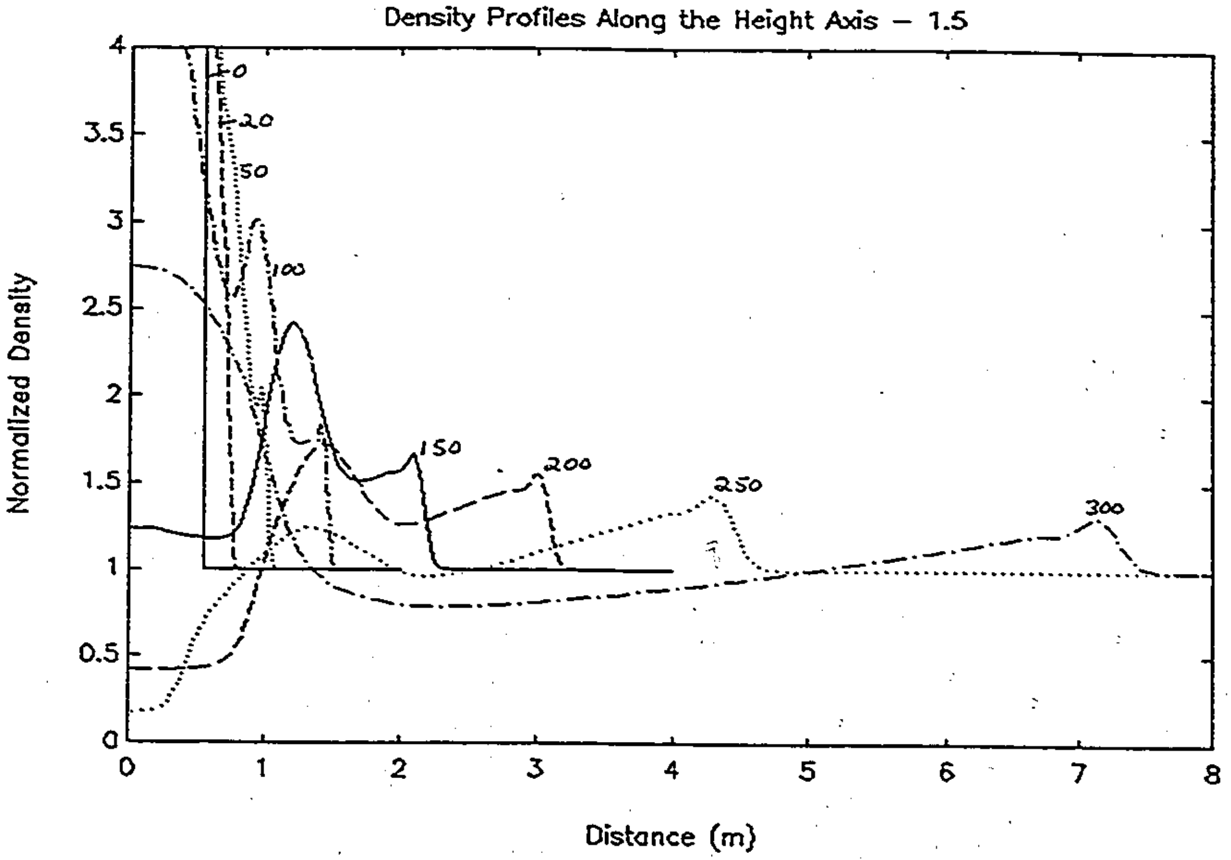

Figure 4.2.2-4 Height Density Profiles, ΔP = 19, E11 = 1.5

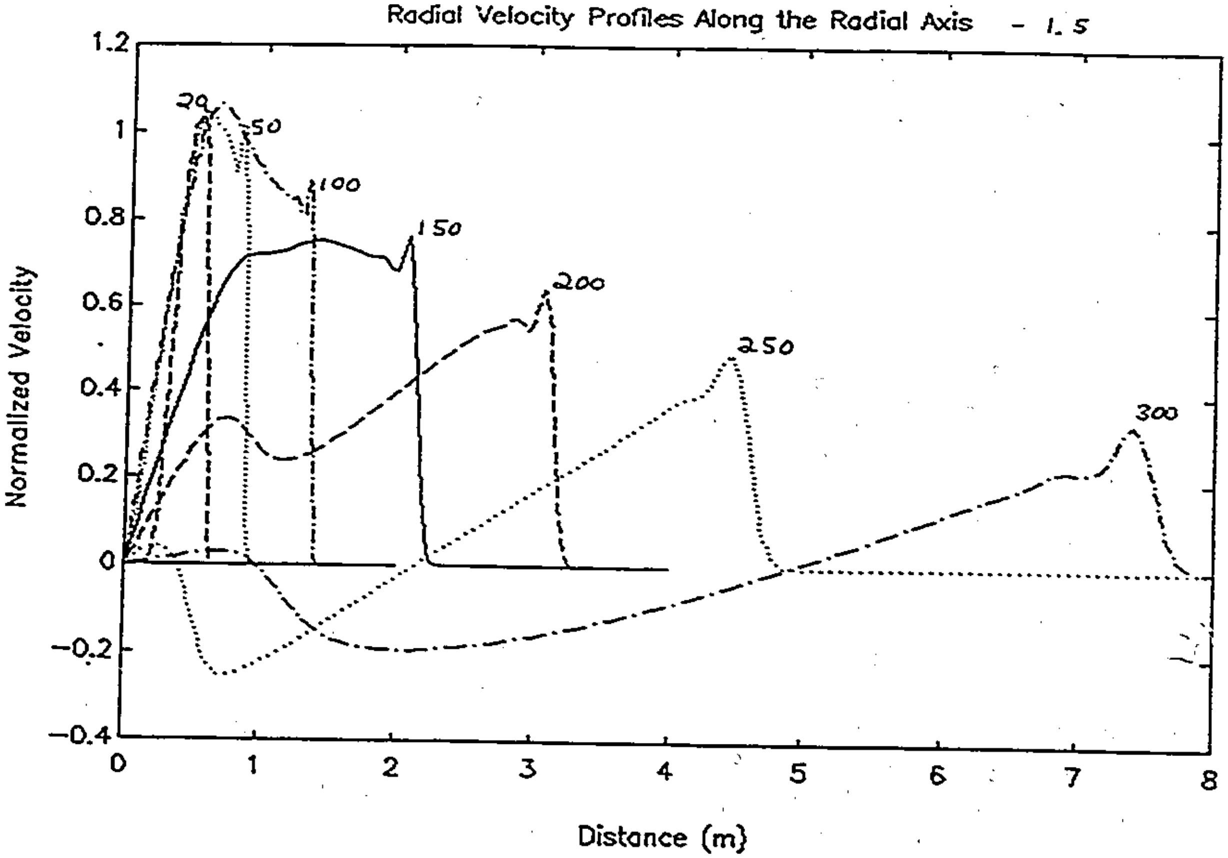

Figure 4.2.2-5 Radial Velocity Radial Profiles, ΔP = 19, Ell = 1.5

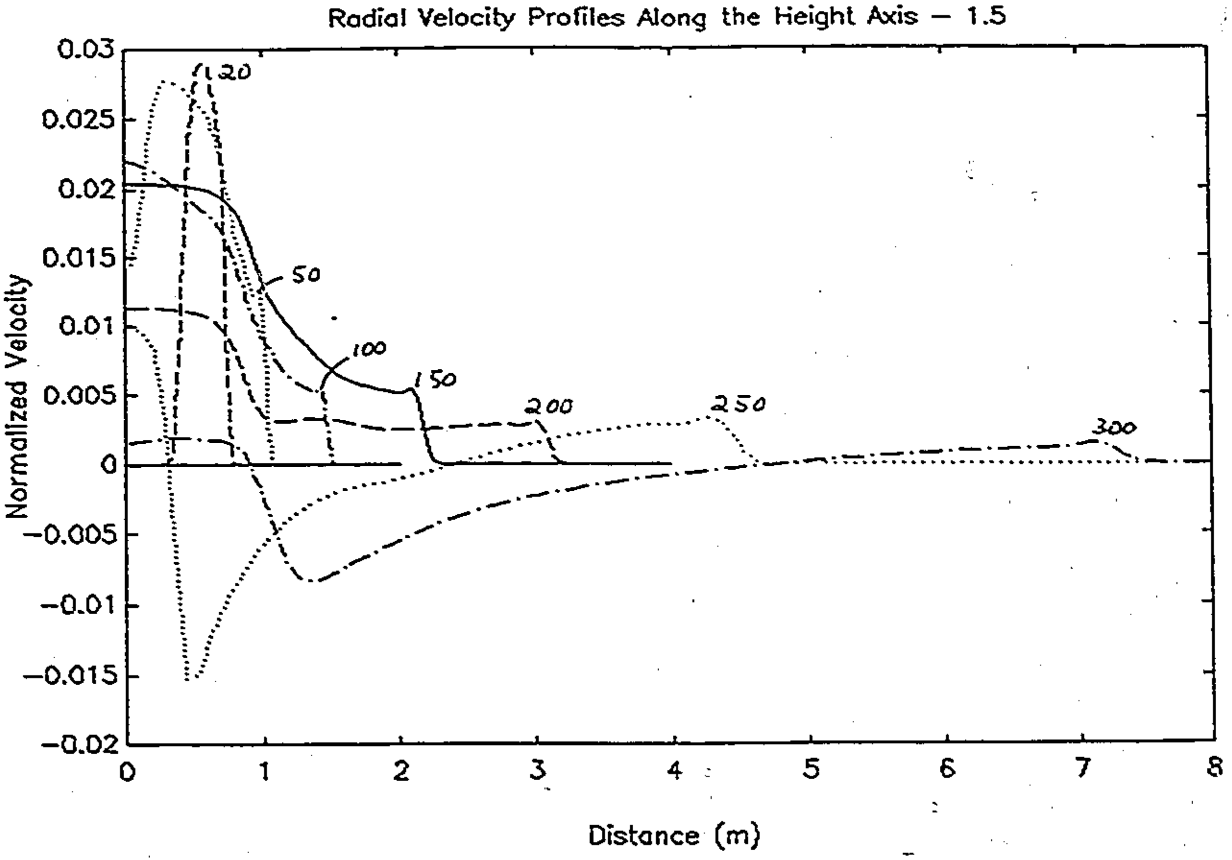

Figure 4.2.2-6 Radial Velocity Height Profiles, ΔP = 19, Ell = 1.5

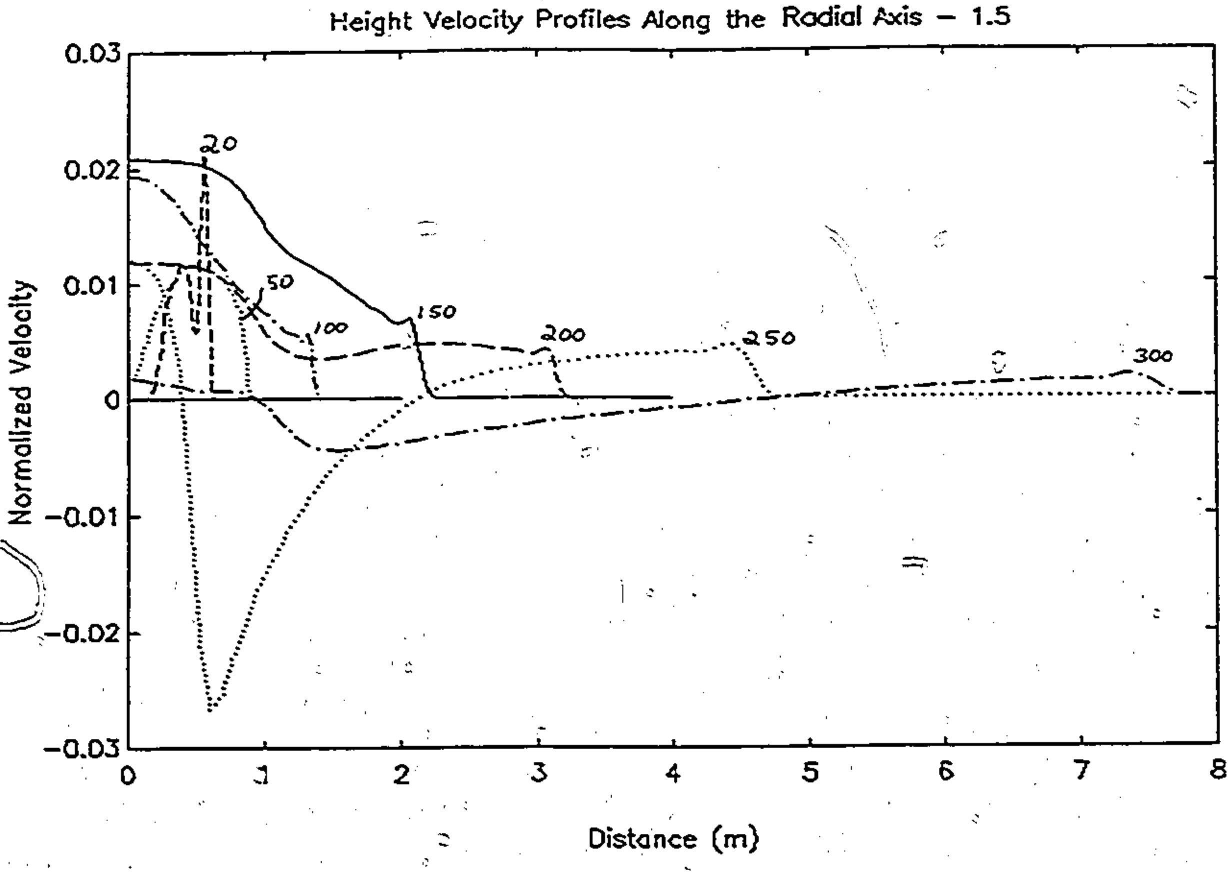

Figure 4.2.2-7 Height Velocity Radial Profiles, ΔP = 19, Ell = 1.5

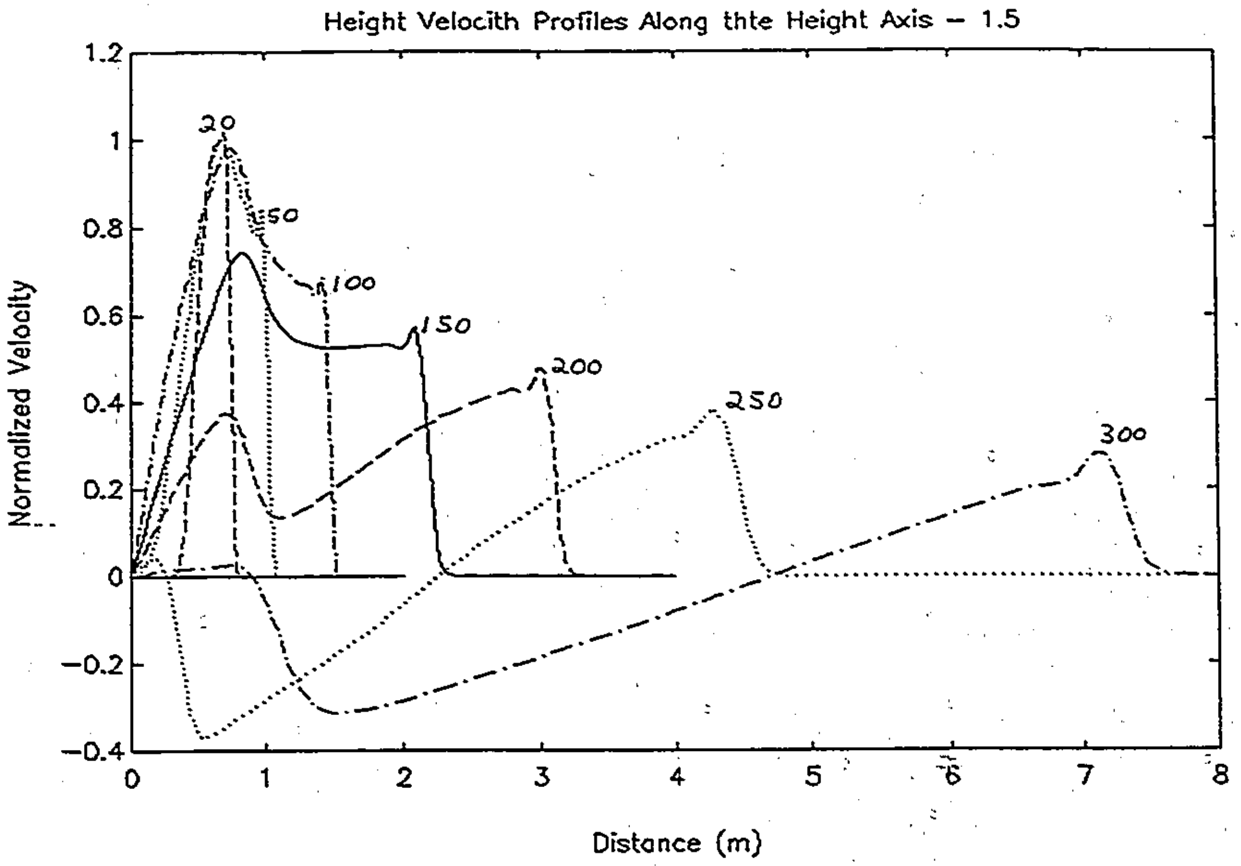

Figure 4.2.2-8 Height Velocity Height Profiles, ΔP = 19, Ell = 1.5

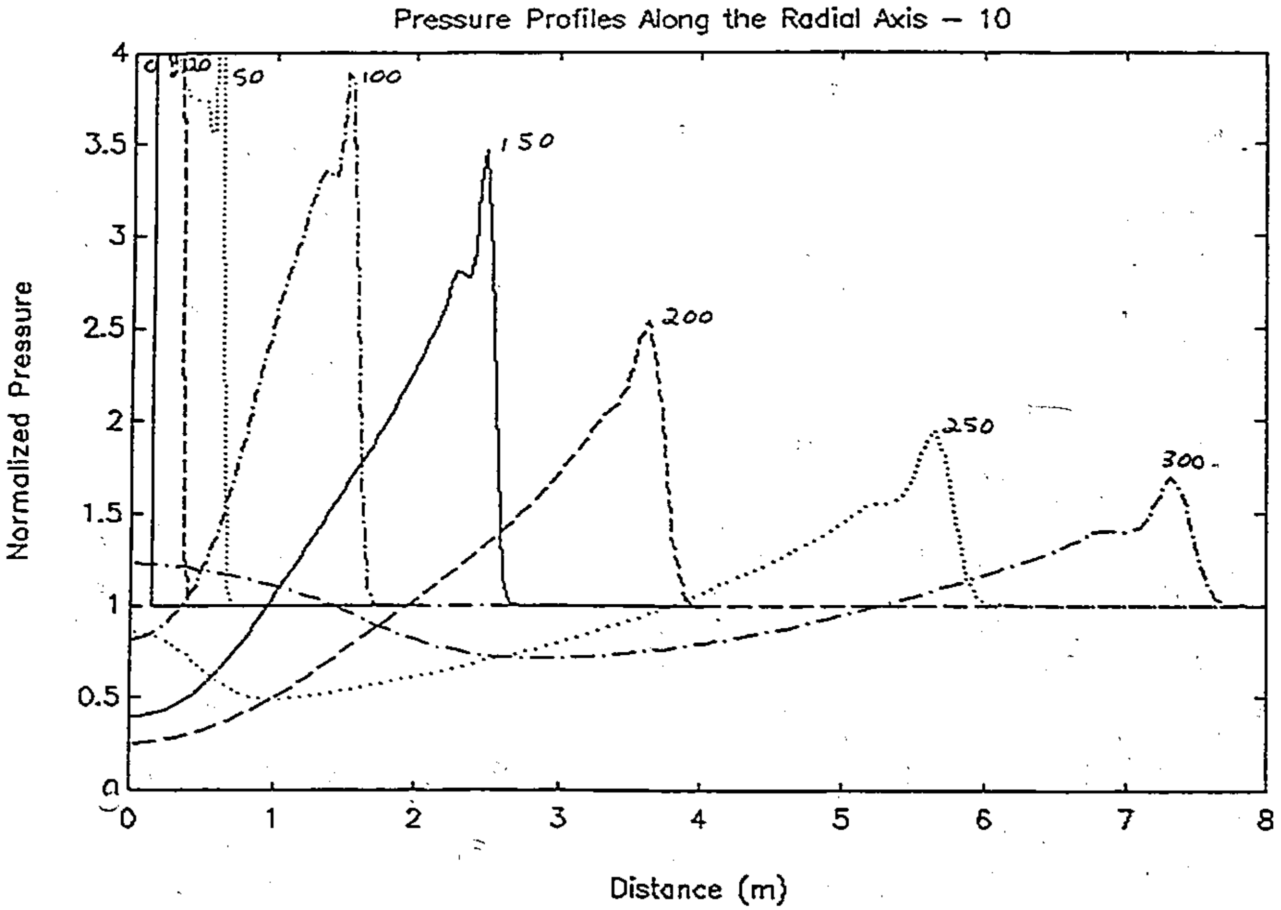

Figure 4.2.3-1 Pressure Radial Profiles, ΔP = 19, E11 = 10

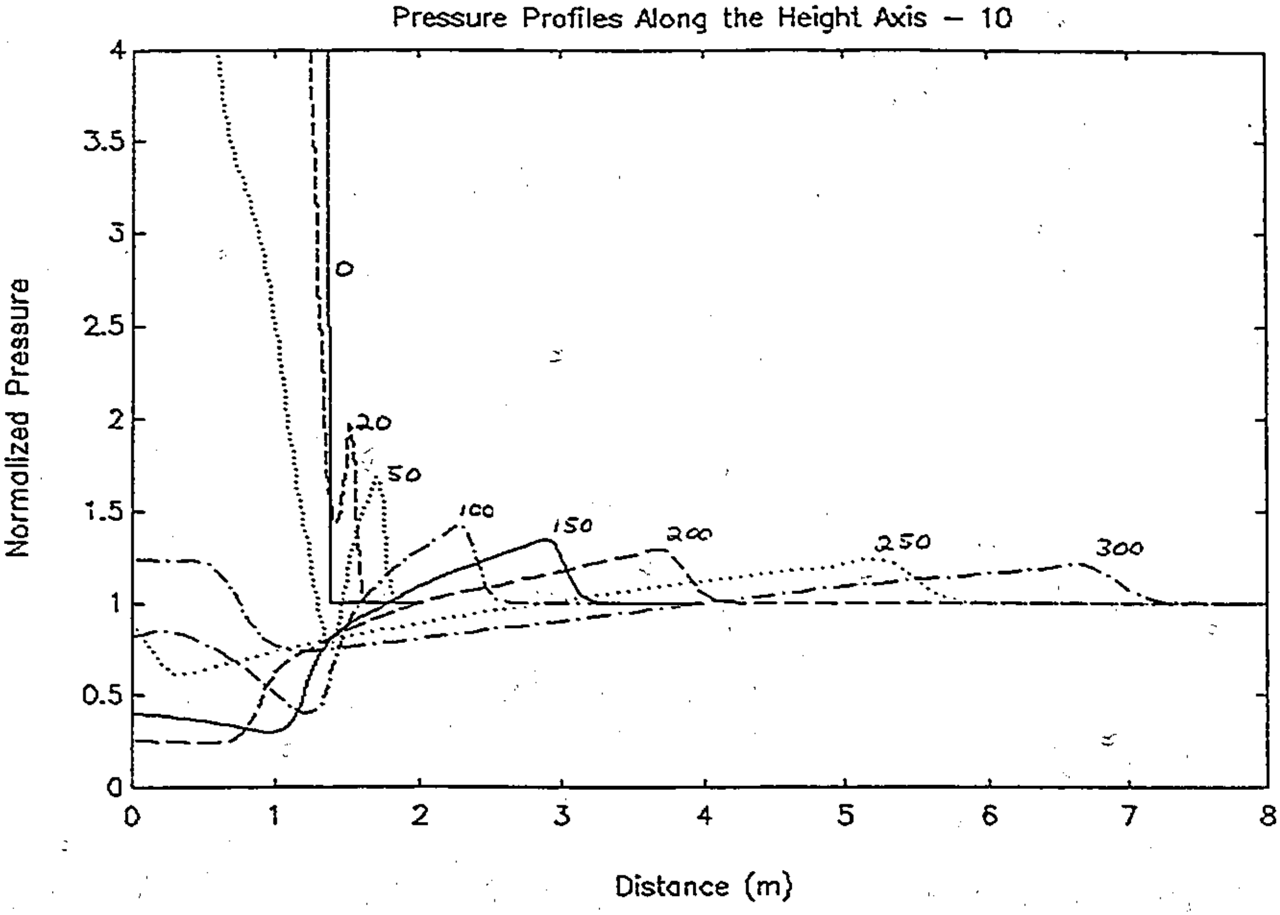

Figure 4.2.3-2 Pressure Height Profiles, ΔP = 19, Ell = 10

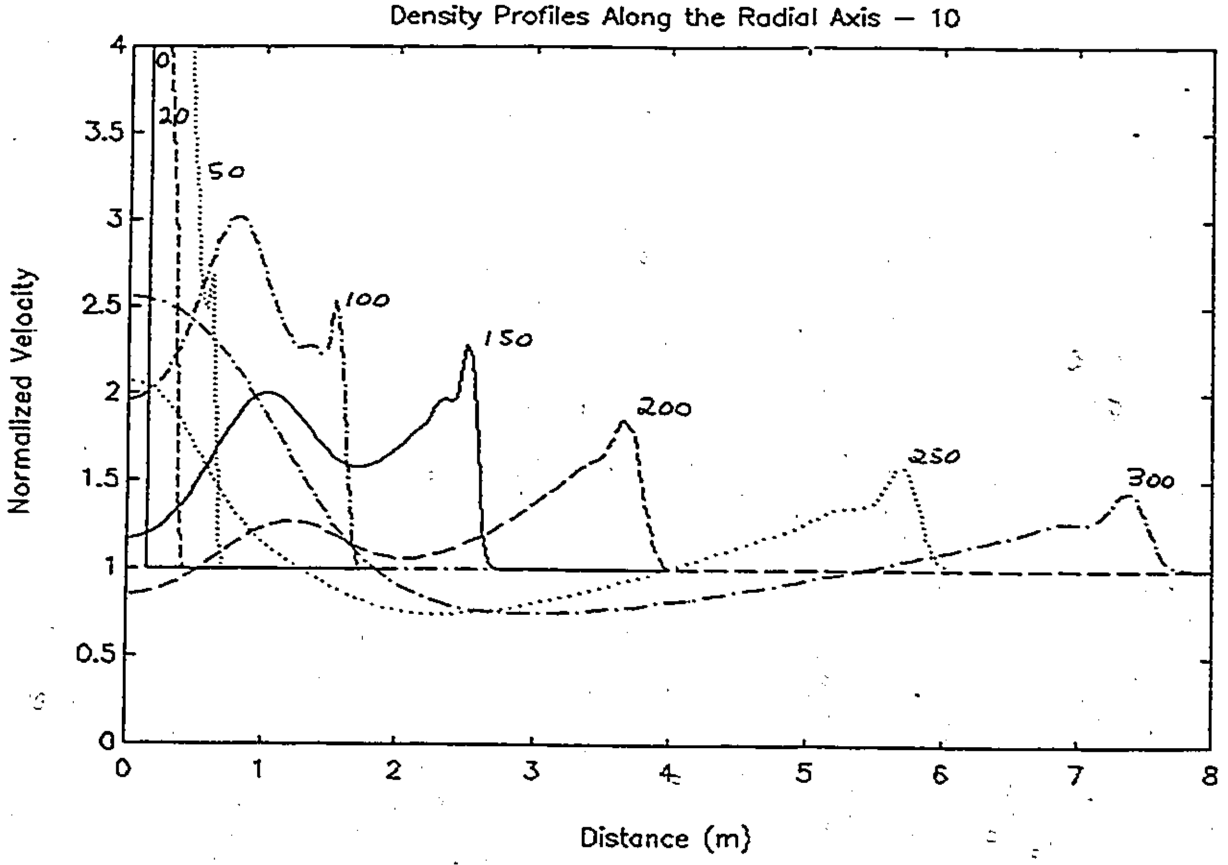

Figure 4.2.3-3 Radial Density Profiles, ΔP = 19, E11 = 10

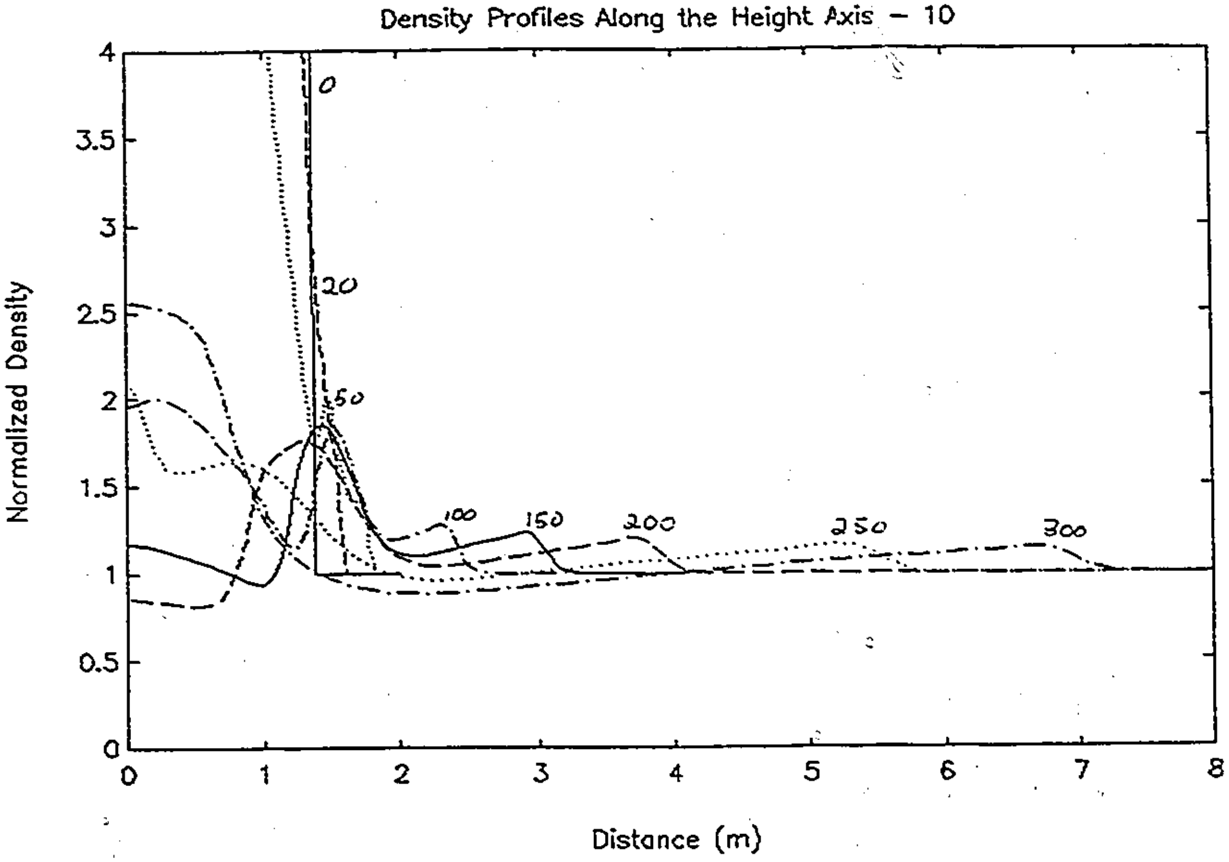

Figure 4.2.3-4 Height Density Profiles, ΔP = 19, Ell = 10

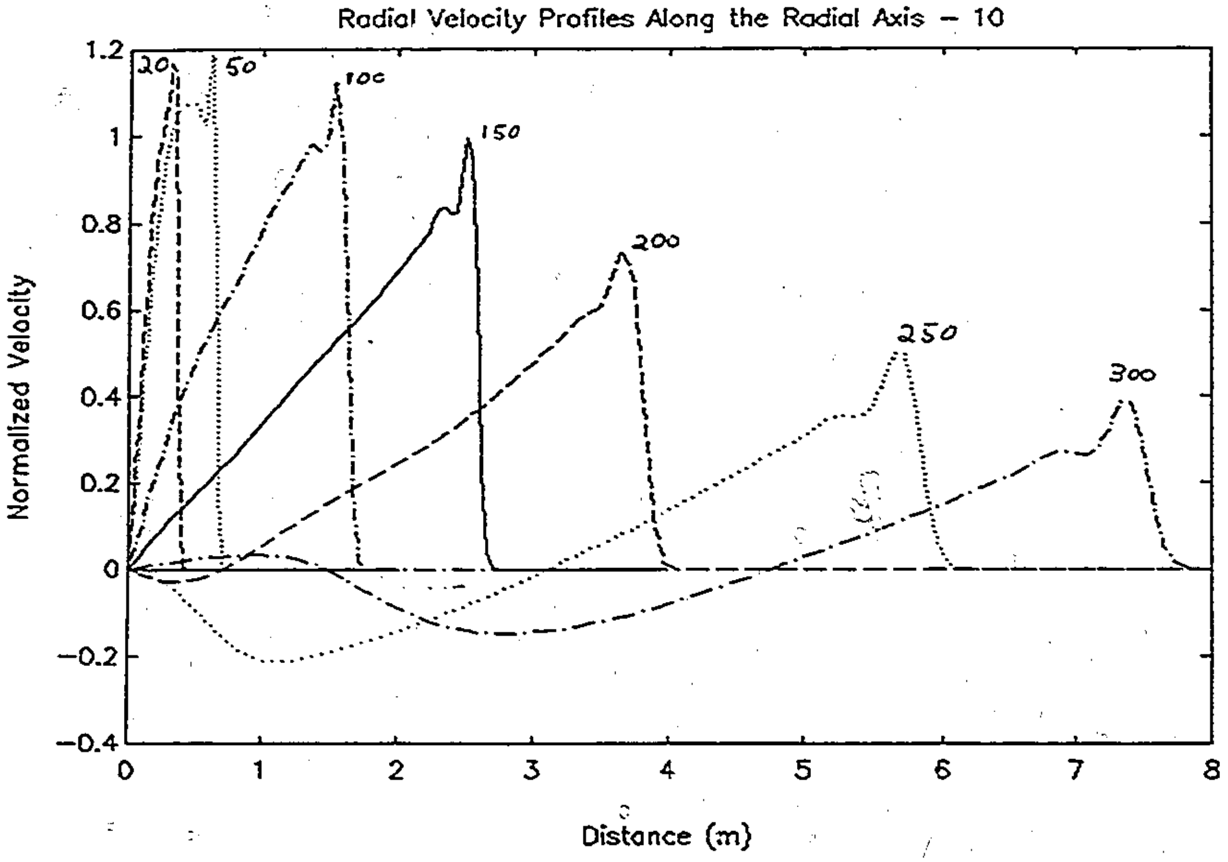

Figure 4.2.3-5 Radial Velocity Radial Profiles, ΔP = 19, E11 = 10

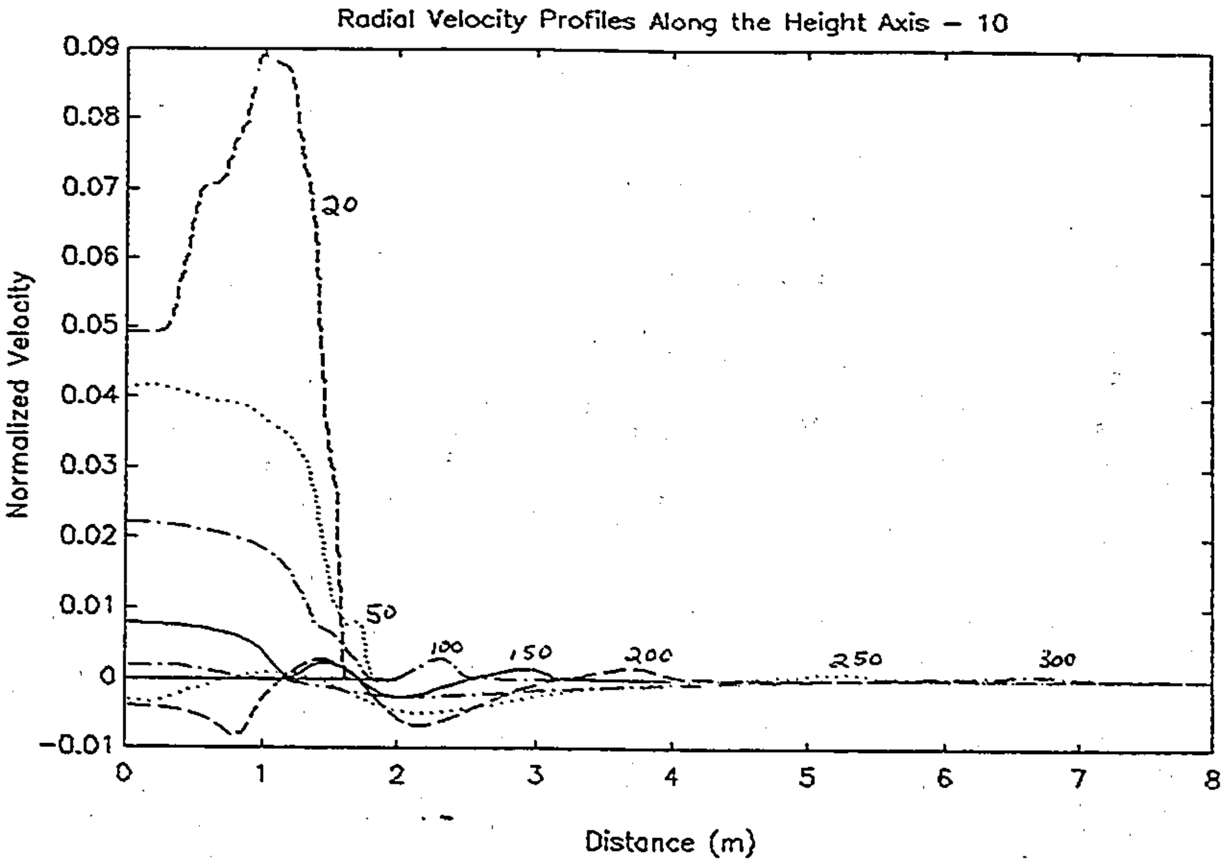

Figure 4.2.3-6 Radial Velocity Height Profiles, ΔP = 19, E11 = 10

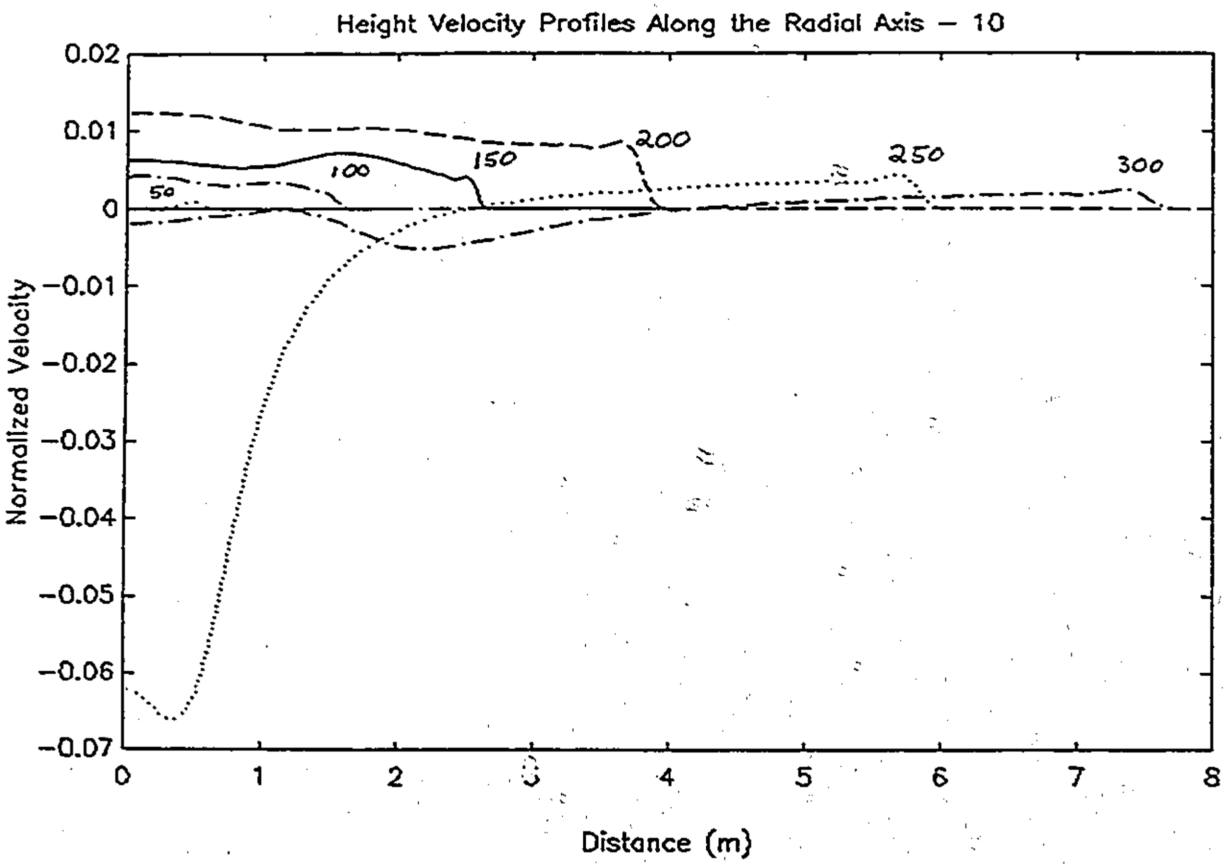

Figure 4.2.3-7 Height Velocity Radial Profiles, ΔP = 19, Ell = 10

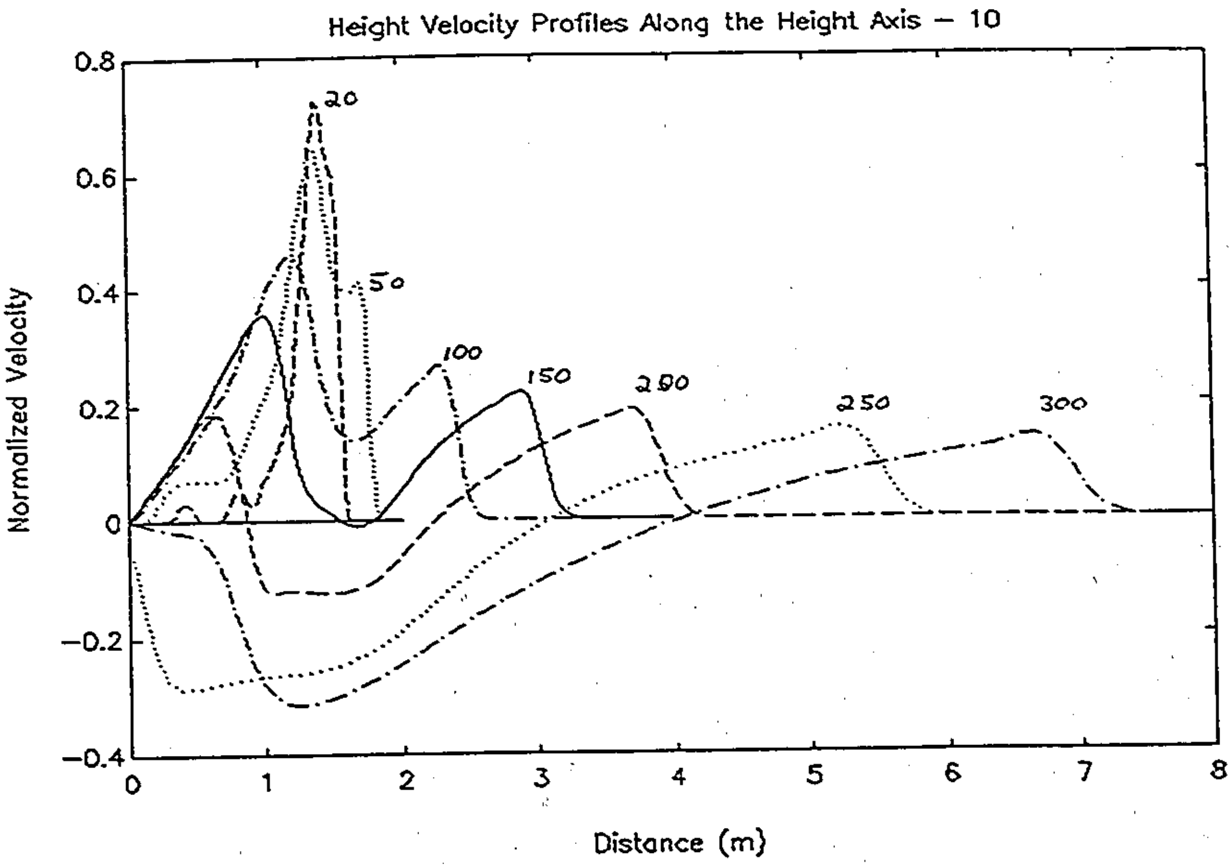

Figure 4.2.3-8 Height Velocity Height Profiles, ΔP = 19, Ell = 10

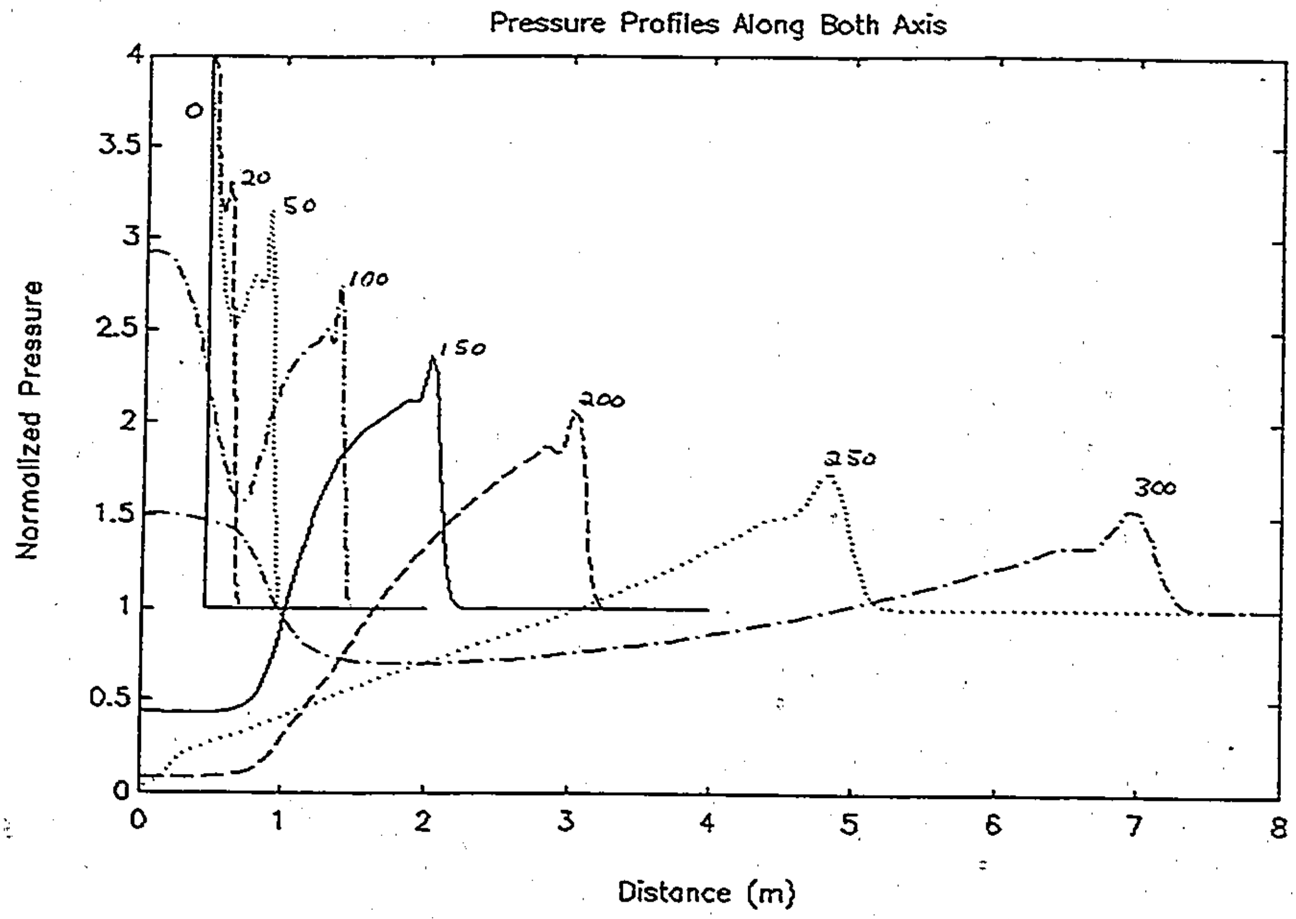

Figure 4.2.4-1 Pressure Profiles, ΔP = 19, E11 = 1

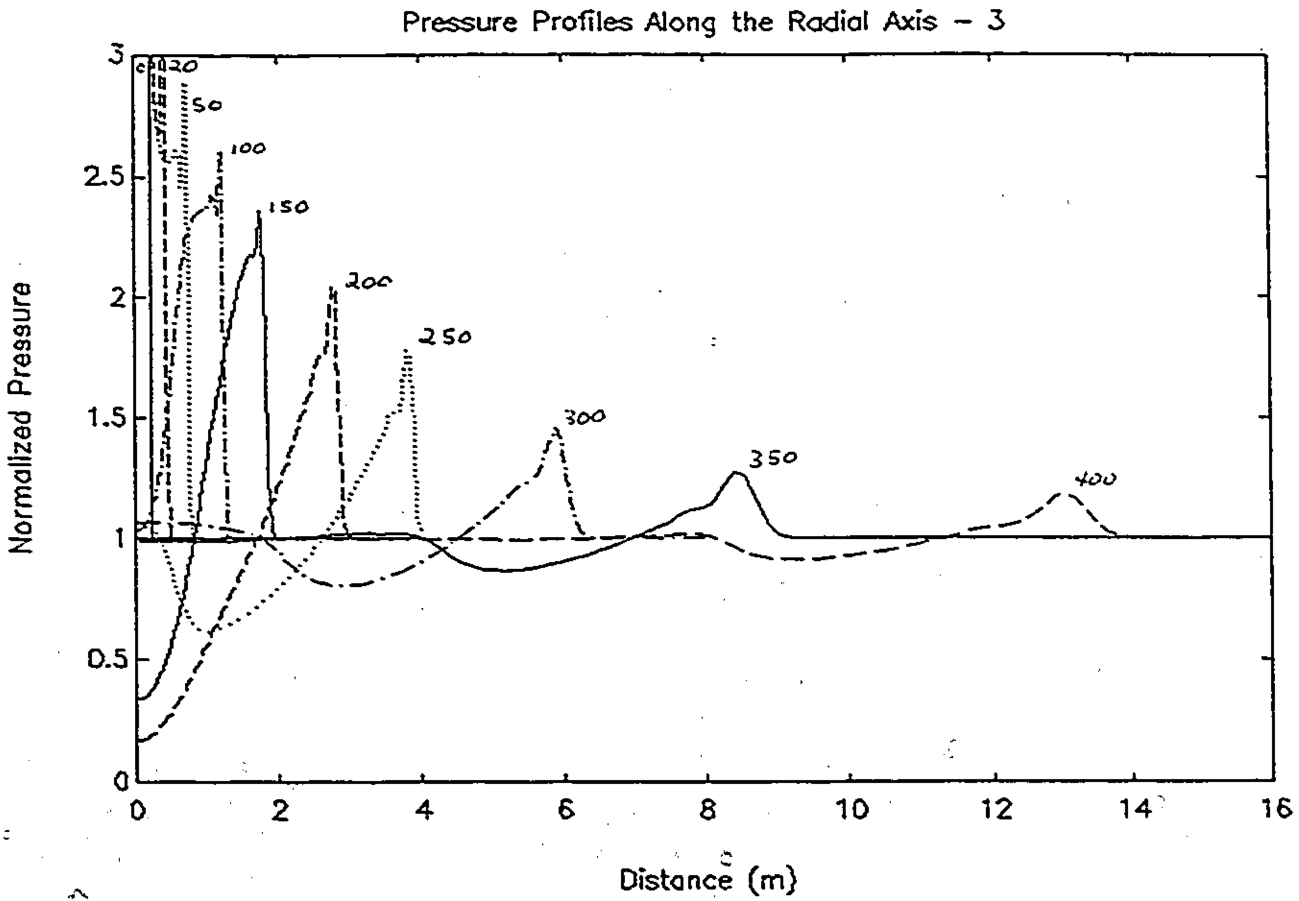

Figure 4.3.1-1 Radial Pressure Profiles, ΔP = 8, E11=3

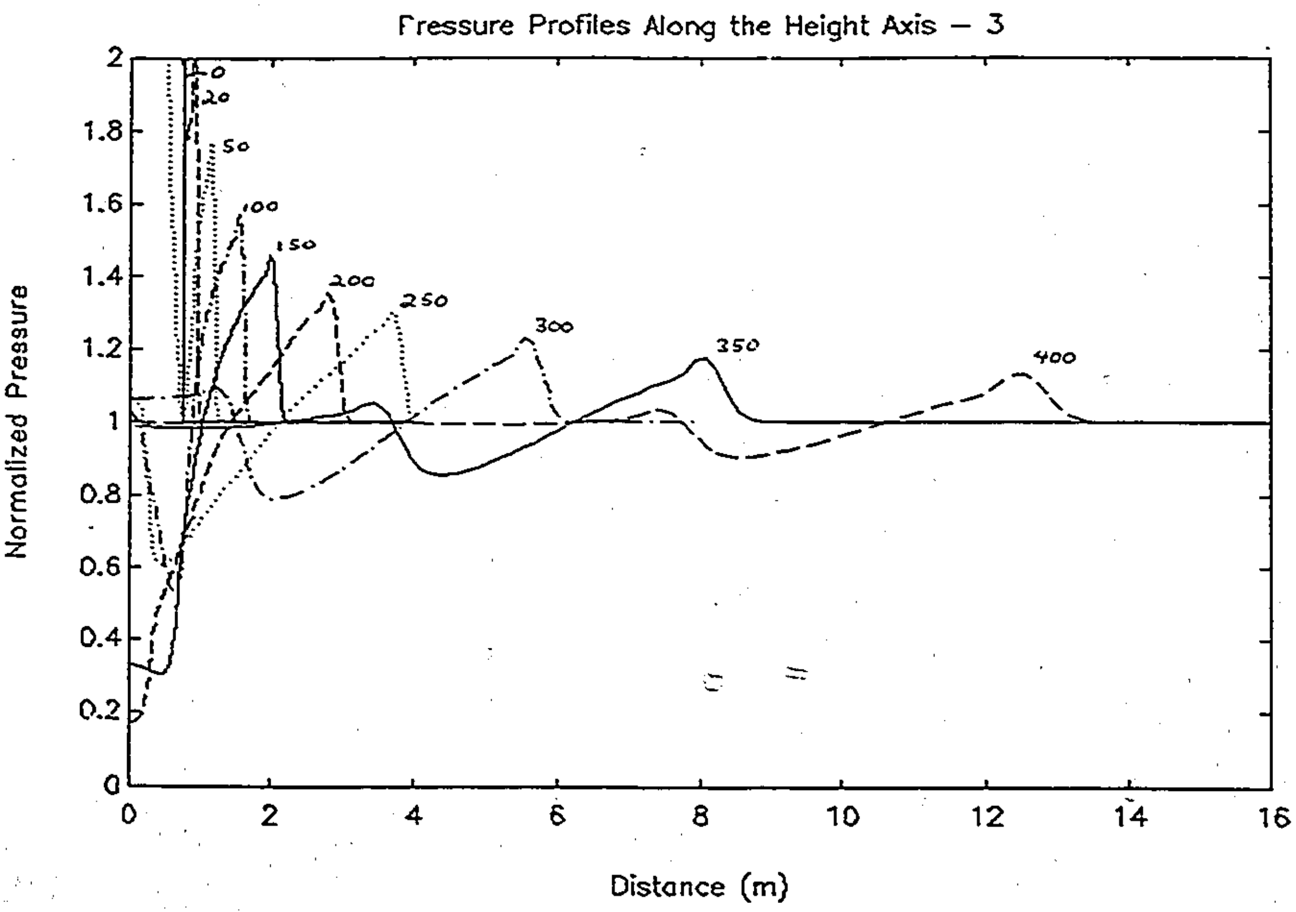

Figure 4.3.1-2 Height Pressure Profiles, ΔP = 8, E11=3

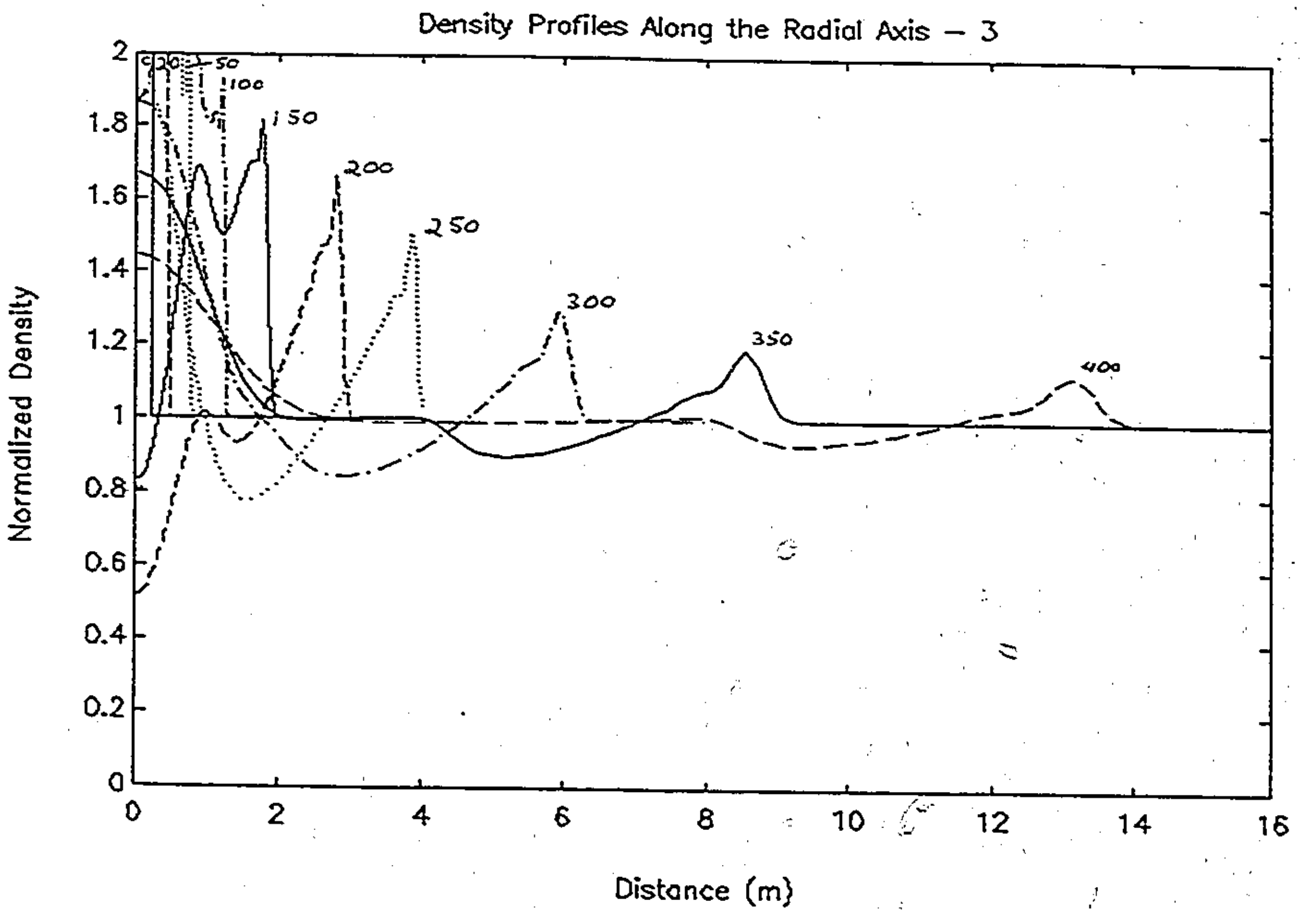

Figure 4.3.1-3 Radial Density Profiles, ΔP = 8, E11=3

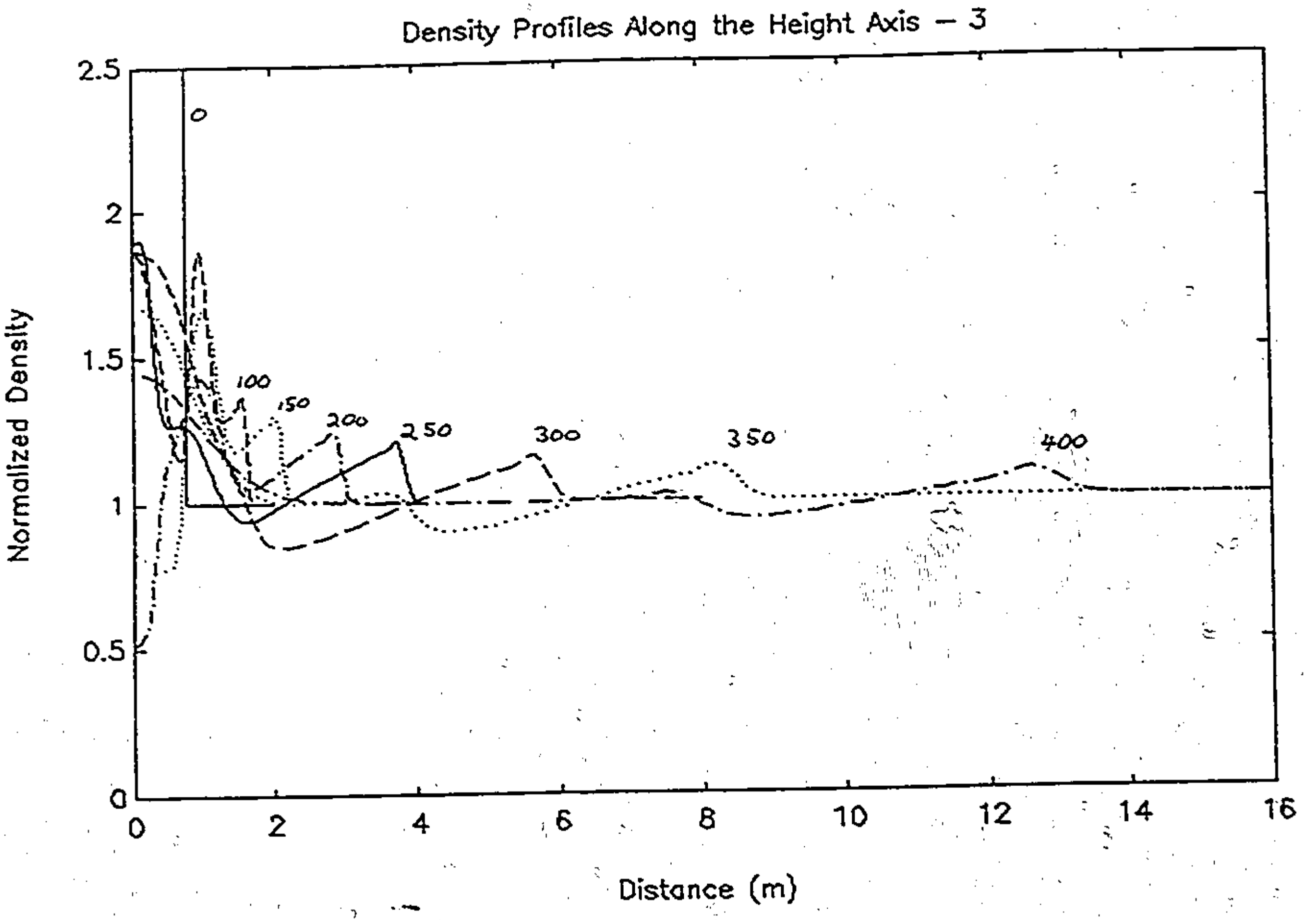

Figure 4.3.1-4 Height Density Profiles, ΔP = 8, E11=3

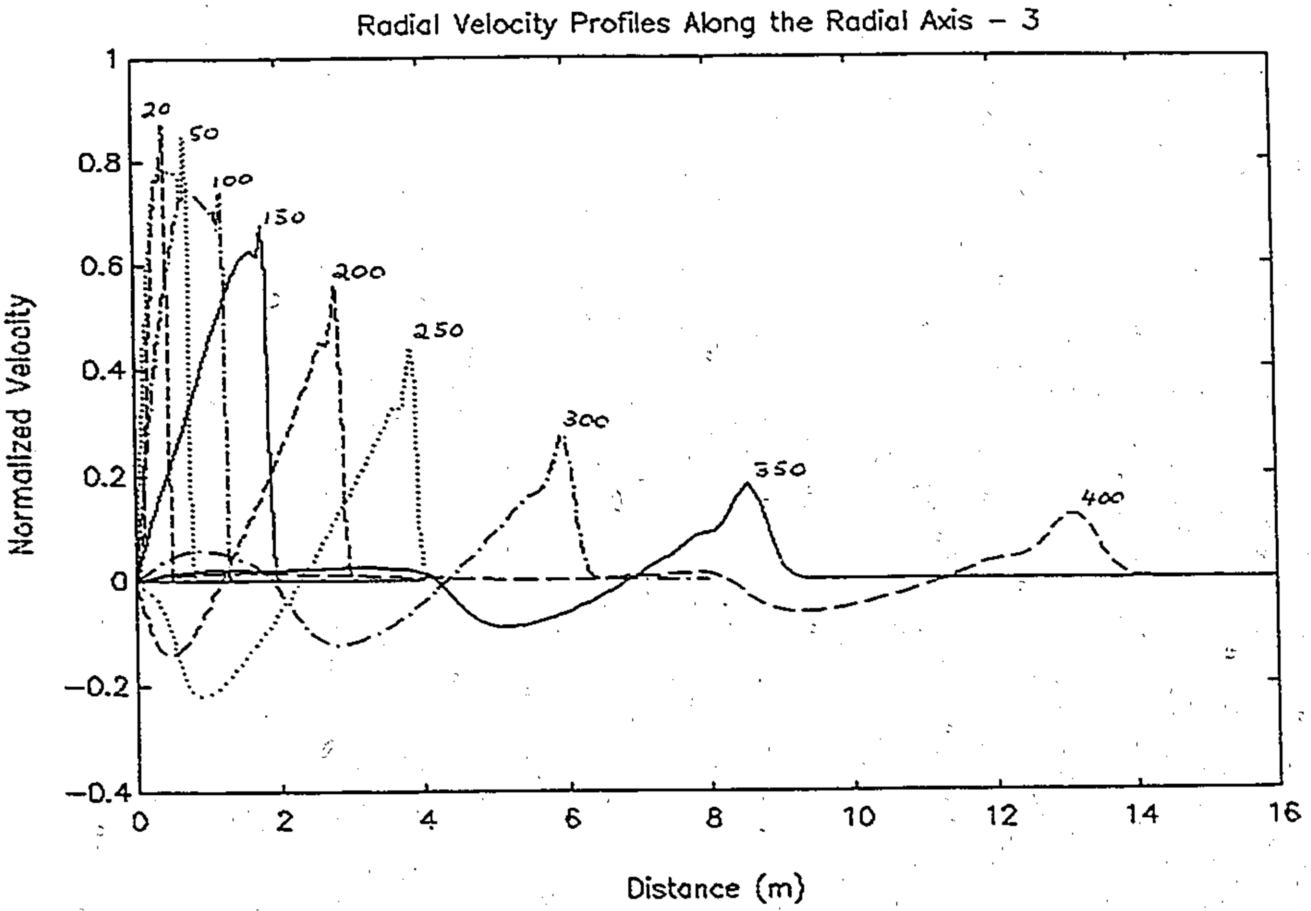

Figure 4.3.1-5 Radial Velocity Radial Profiles, ΔP = 8, Ell=3

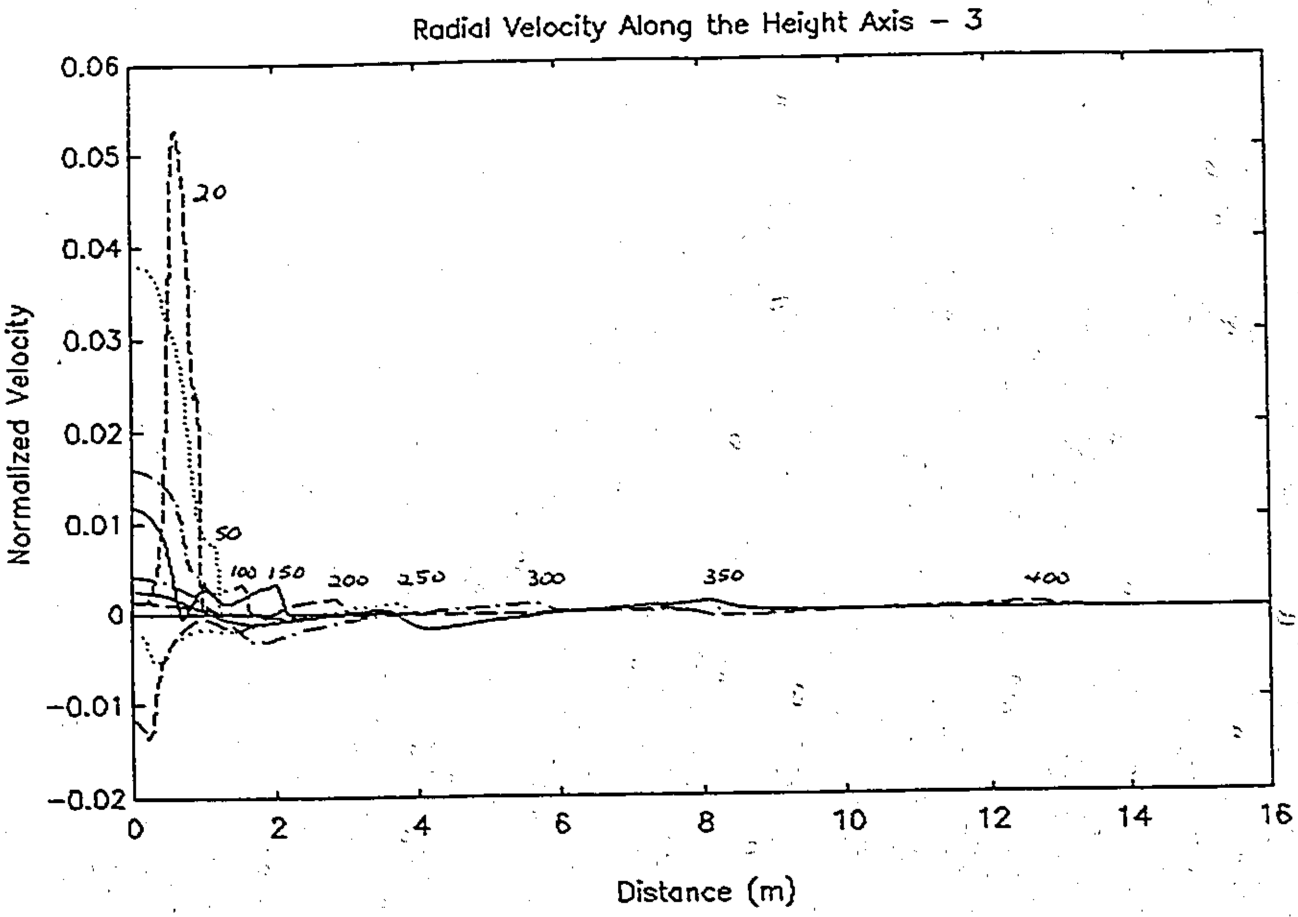

Figure 4.3.1-6 Radial Velocity Height Profiles, ΔP = 8, Ell=3

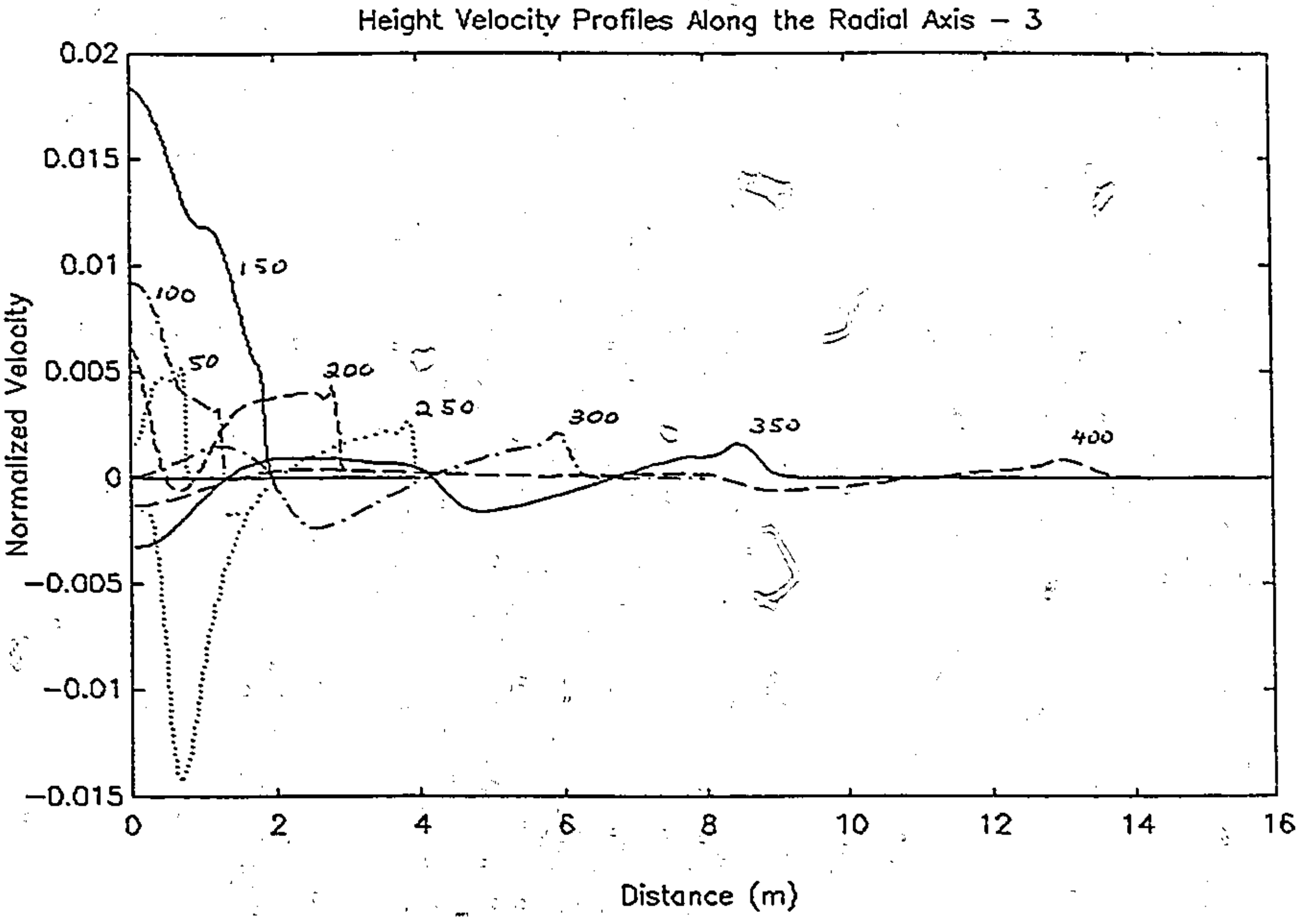

Figure 4.3.1-7 Height Velocity Radial Profiles, ΔP = 8, E11=3

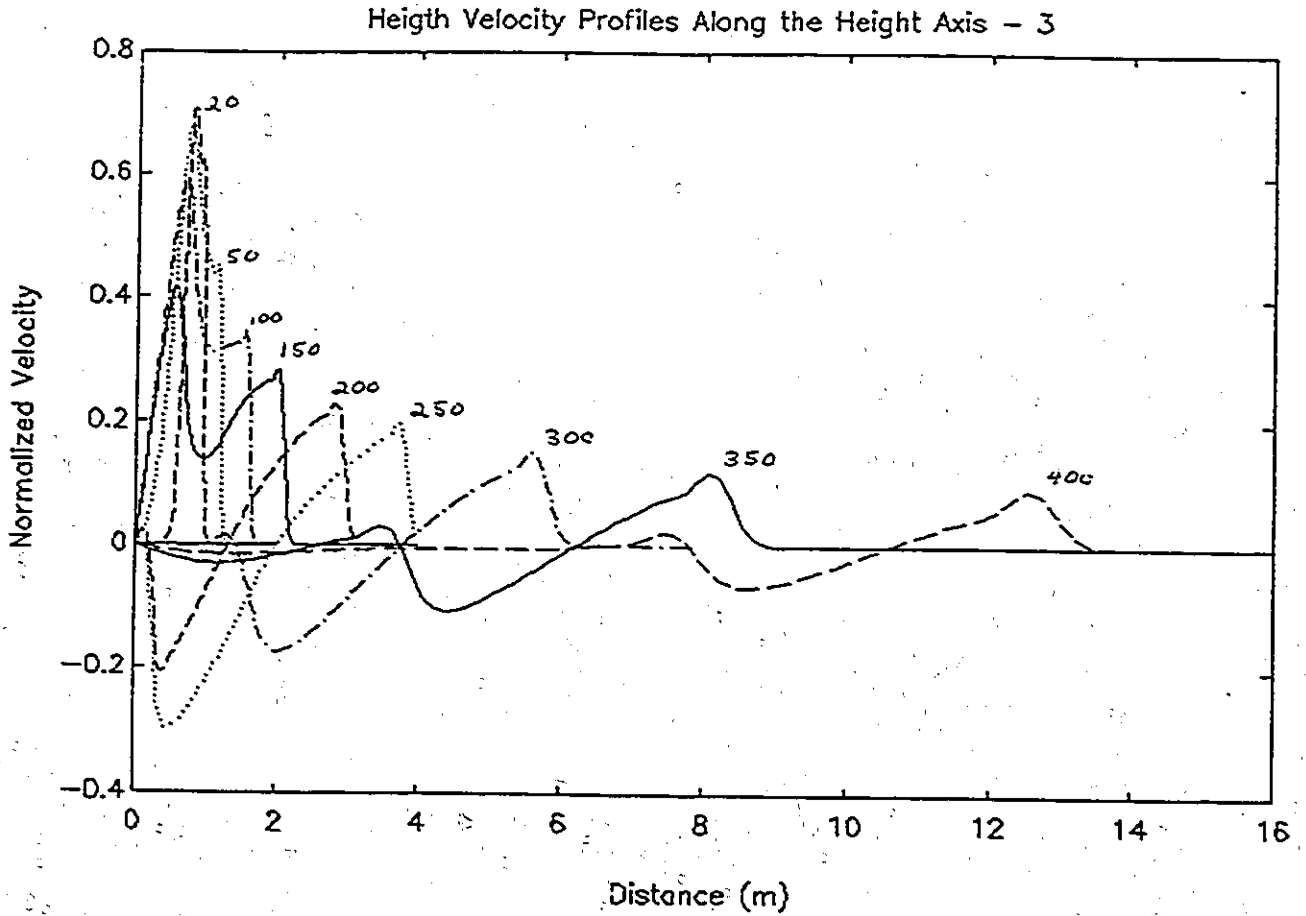

Figure 4.3.1-8 Height Velocity Height Profiles, ΔP = 8, E11=3

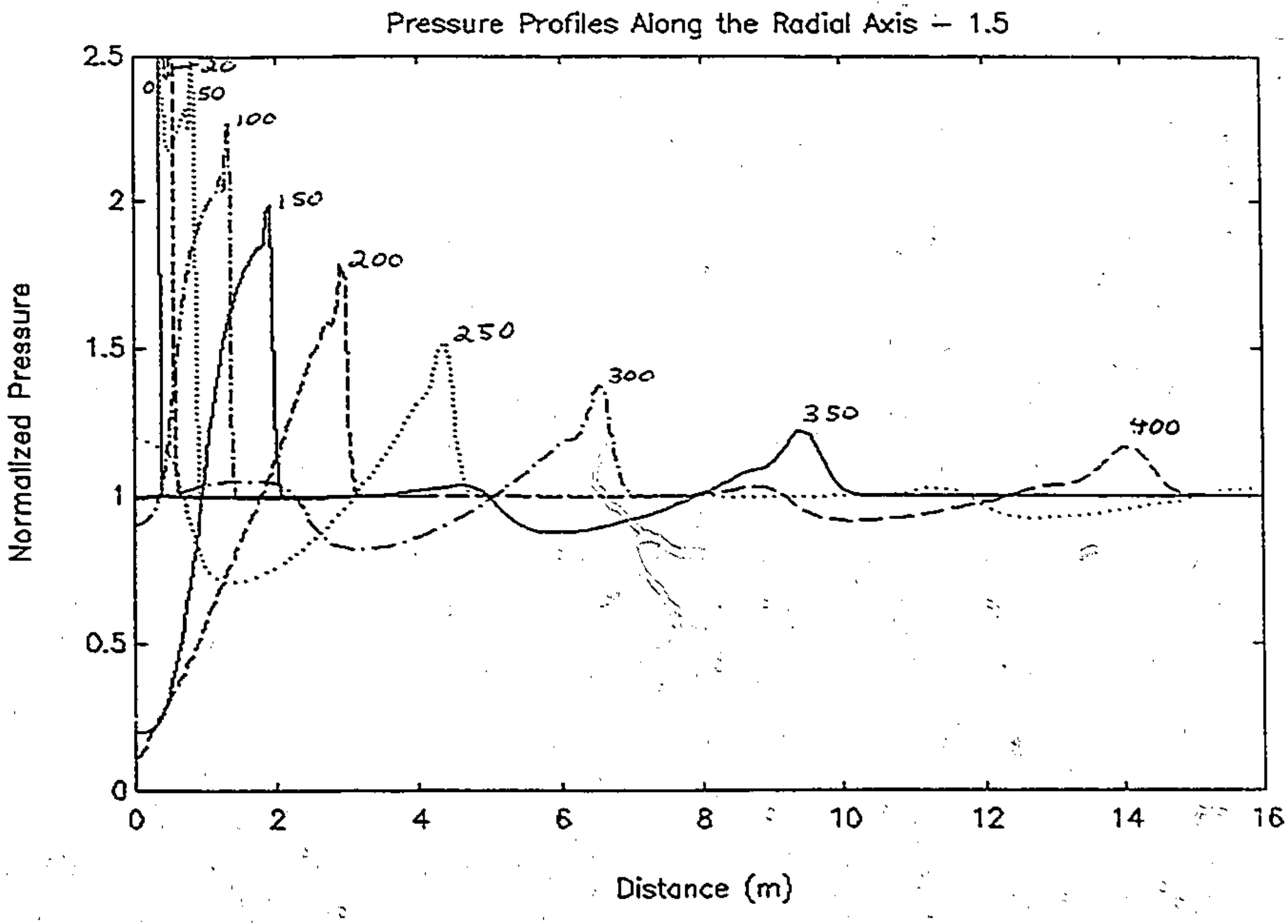

Figure 4.3.2-1 Pressure Radial Profiles, ΔP = 8, Ell=1.5

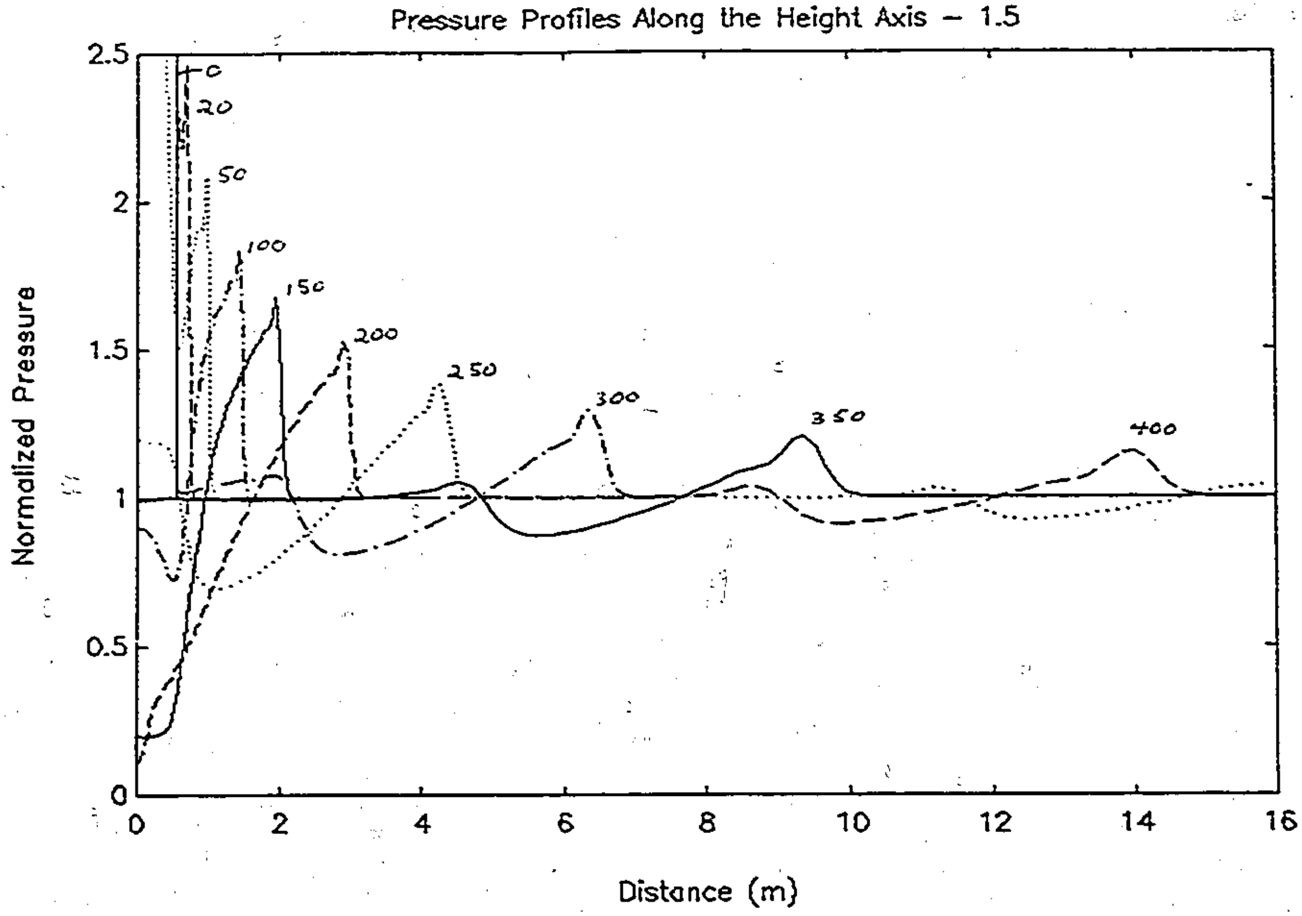

Figure 4.3.2-2 Pressure Height Profiles, ΔP = 8, E11=1.5

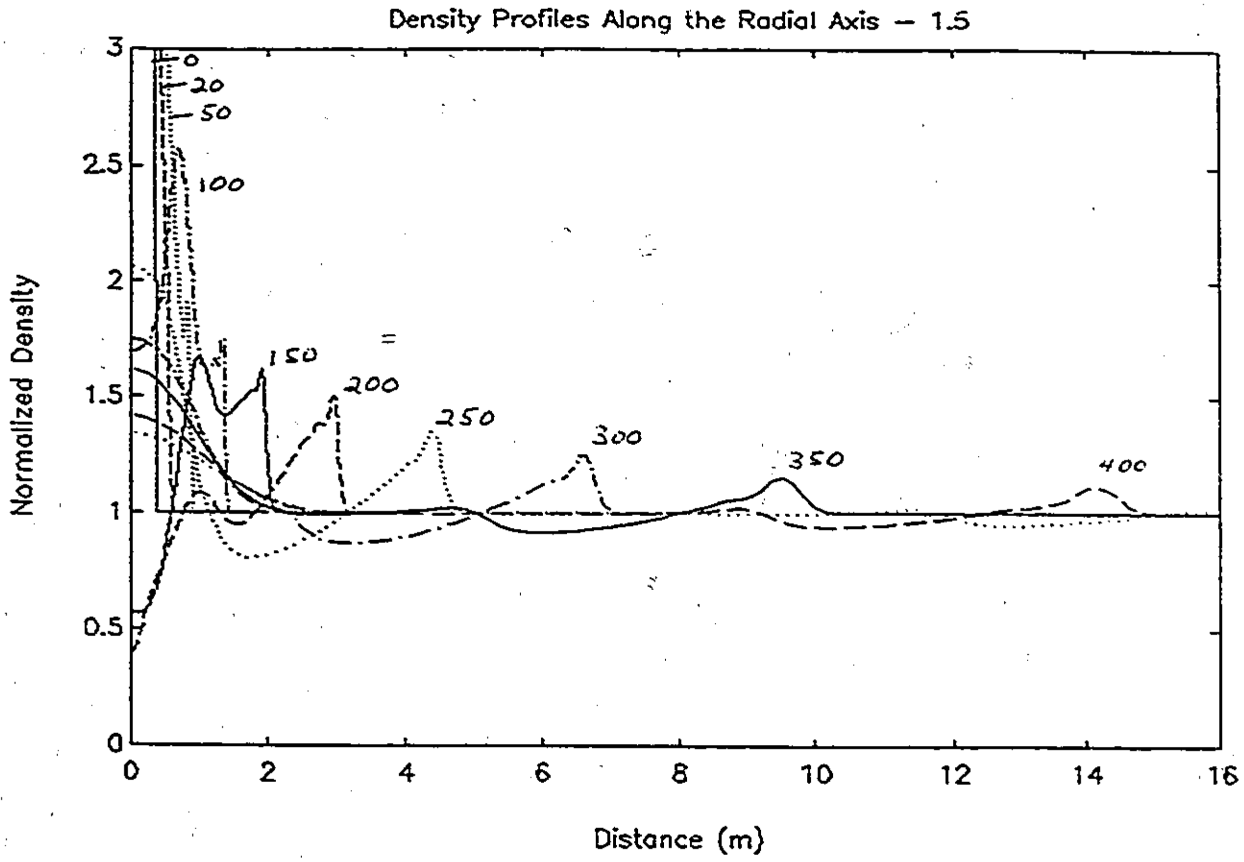

Figure 4.3.2-3 Radial Density Profiles, ΔP = 8, Ell = 1.5

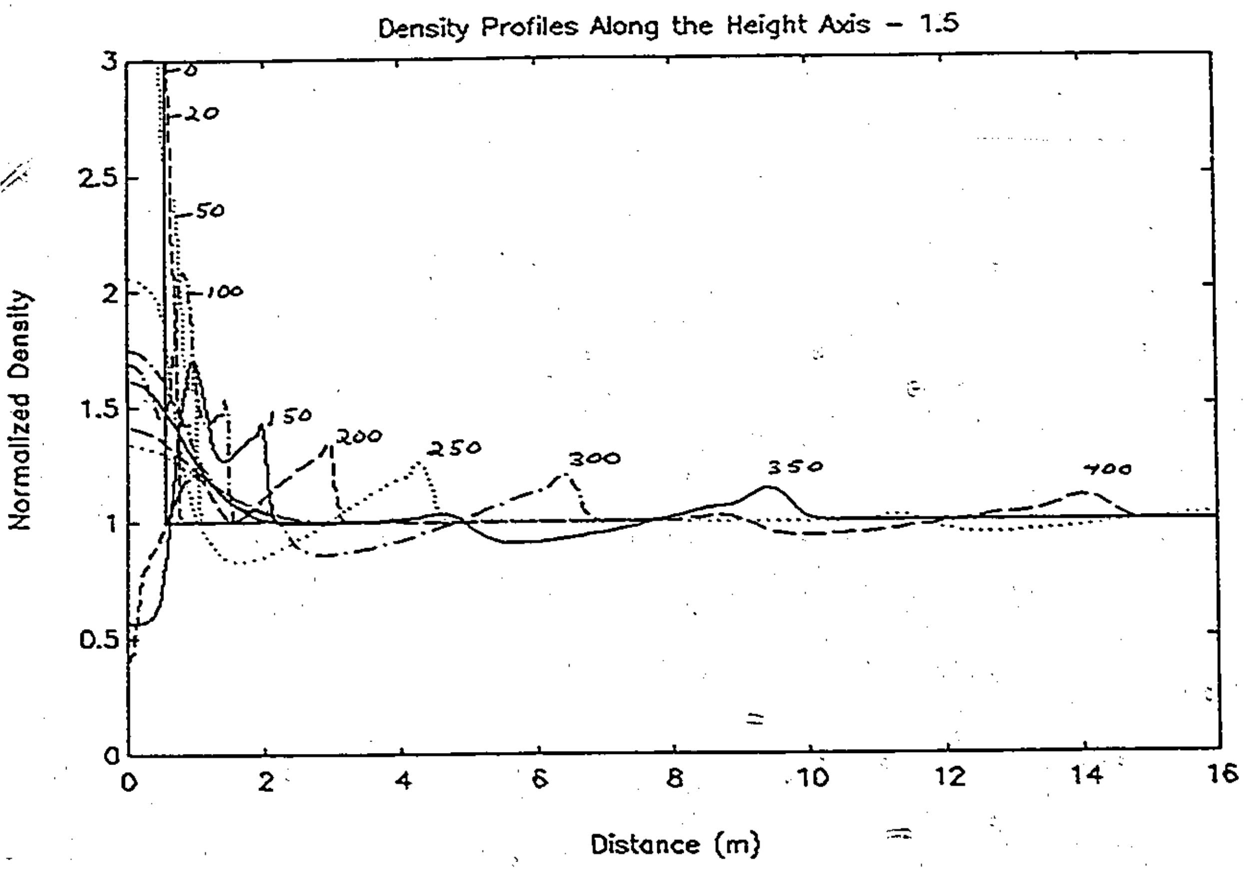

Figure 4.3.2-4 Height Density Profiles, ΔP = 8, Ell = 1.5

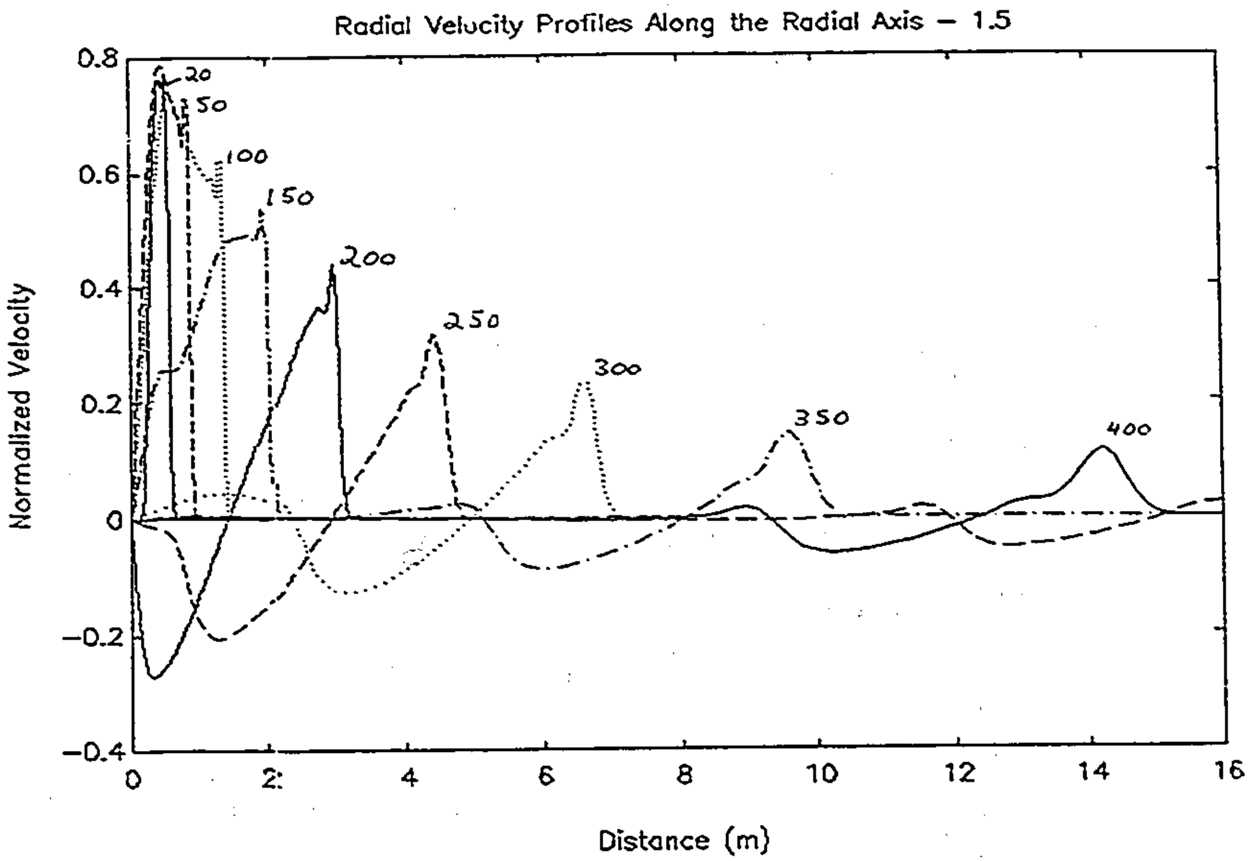

Figure 4.3.2-5 Radial Velocity Radial Profiles, ΔP = 8, Ell = 1.5

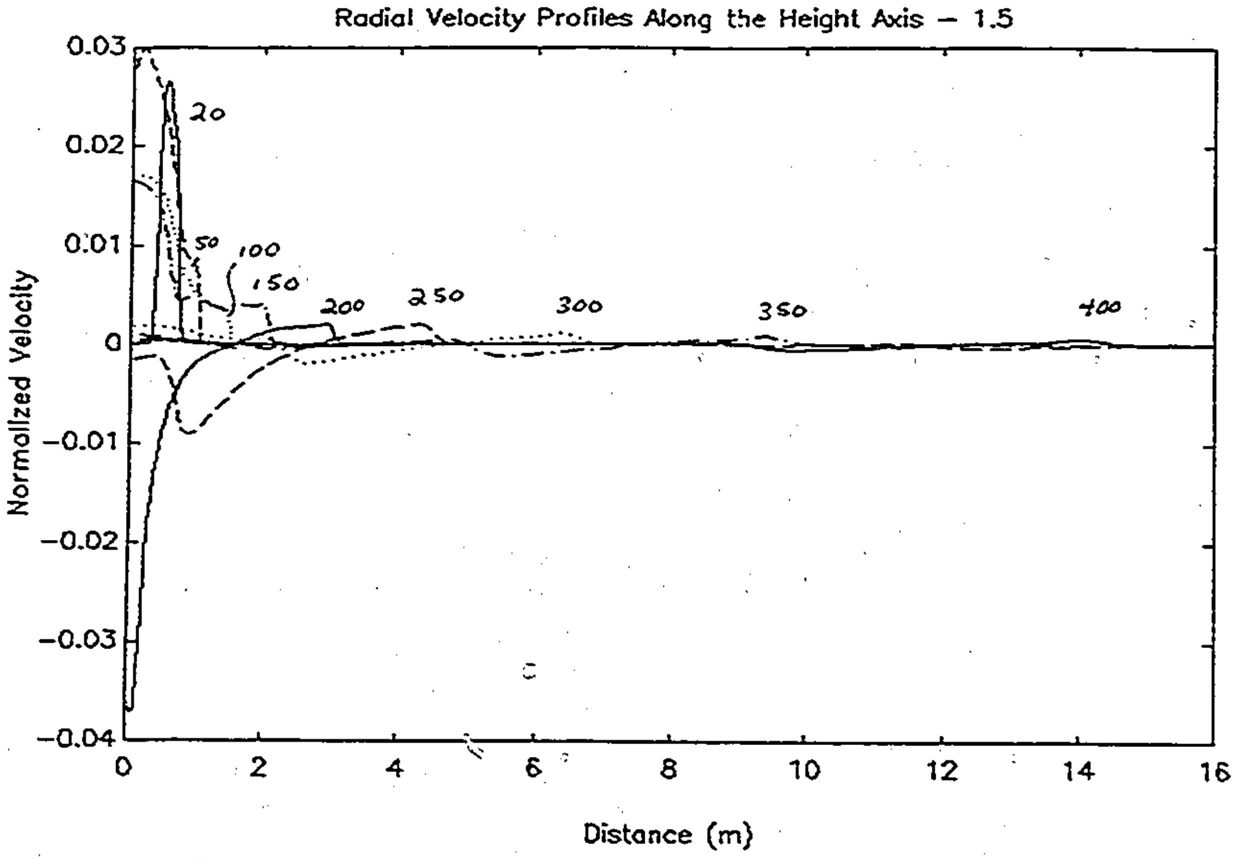

Figure 4.3.2-6 Radial Velocity Height Profiles, ΔP = 8, Ell = 1.5

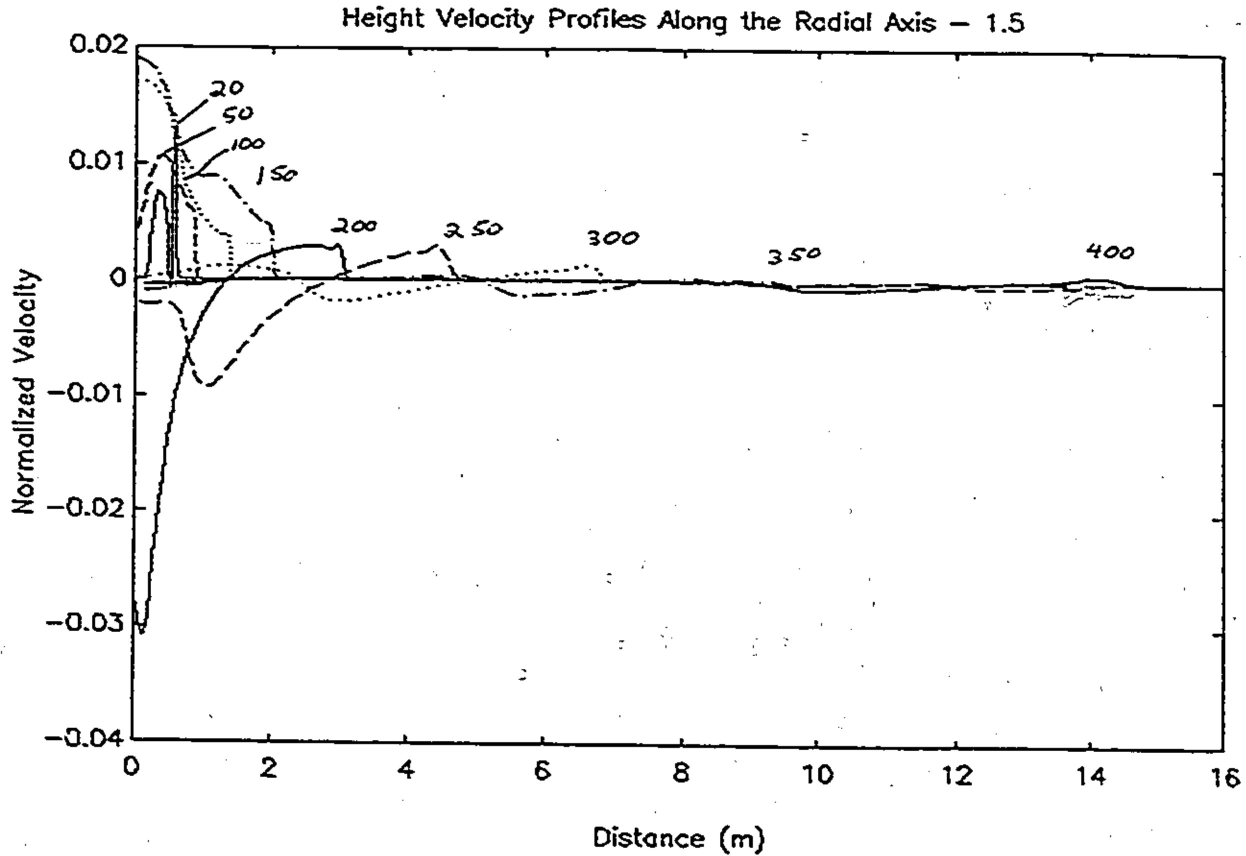

Figure 4.3.2-7 Height Velocity Radial Profiles, ΔP = 8, E11 = 1.5

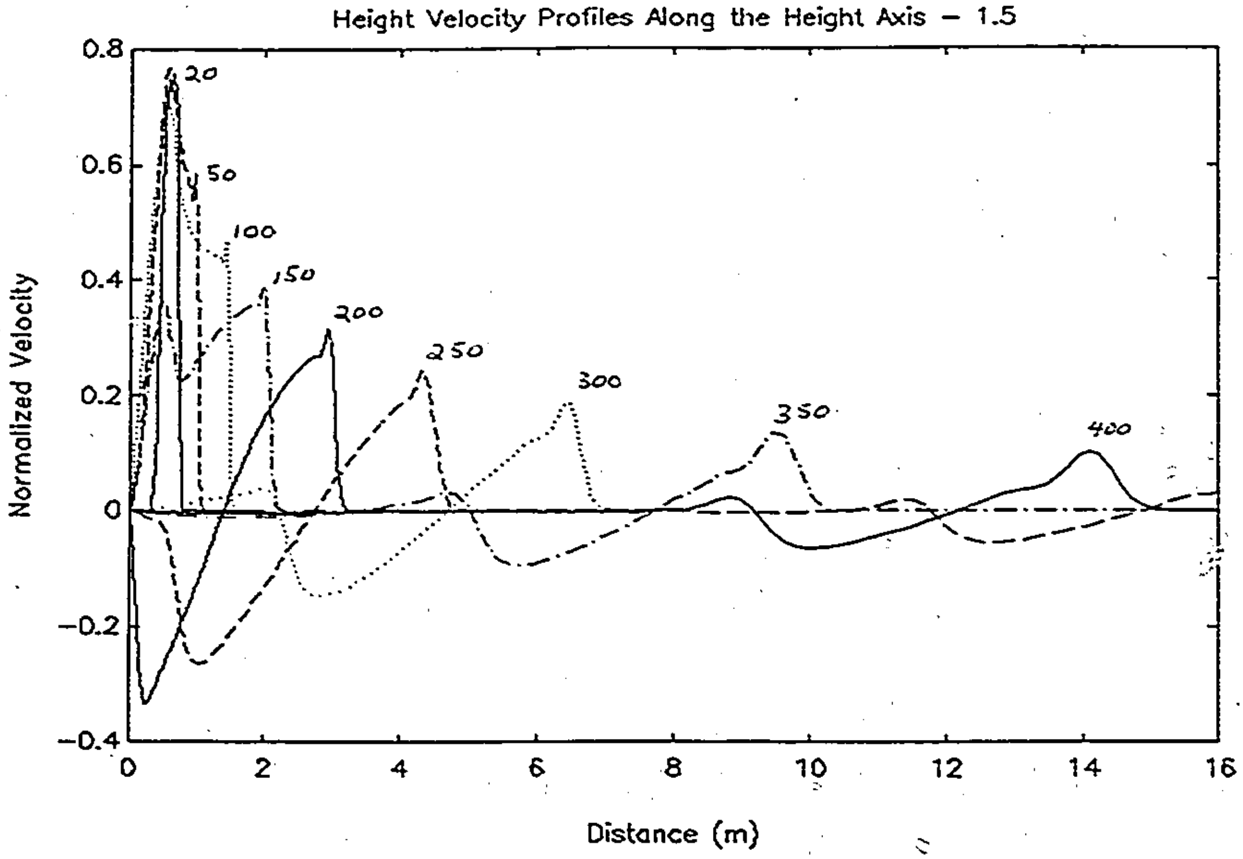

Figure 4.3.2-8 Height Velocity Height Profiles, ΔP = 8, Ell = 1.5

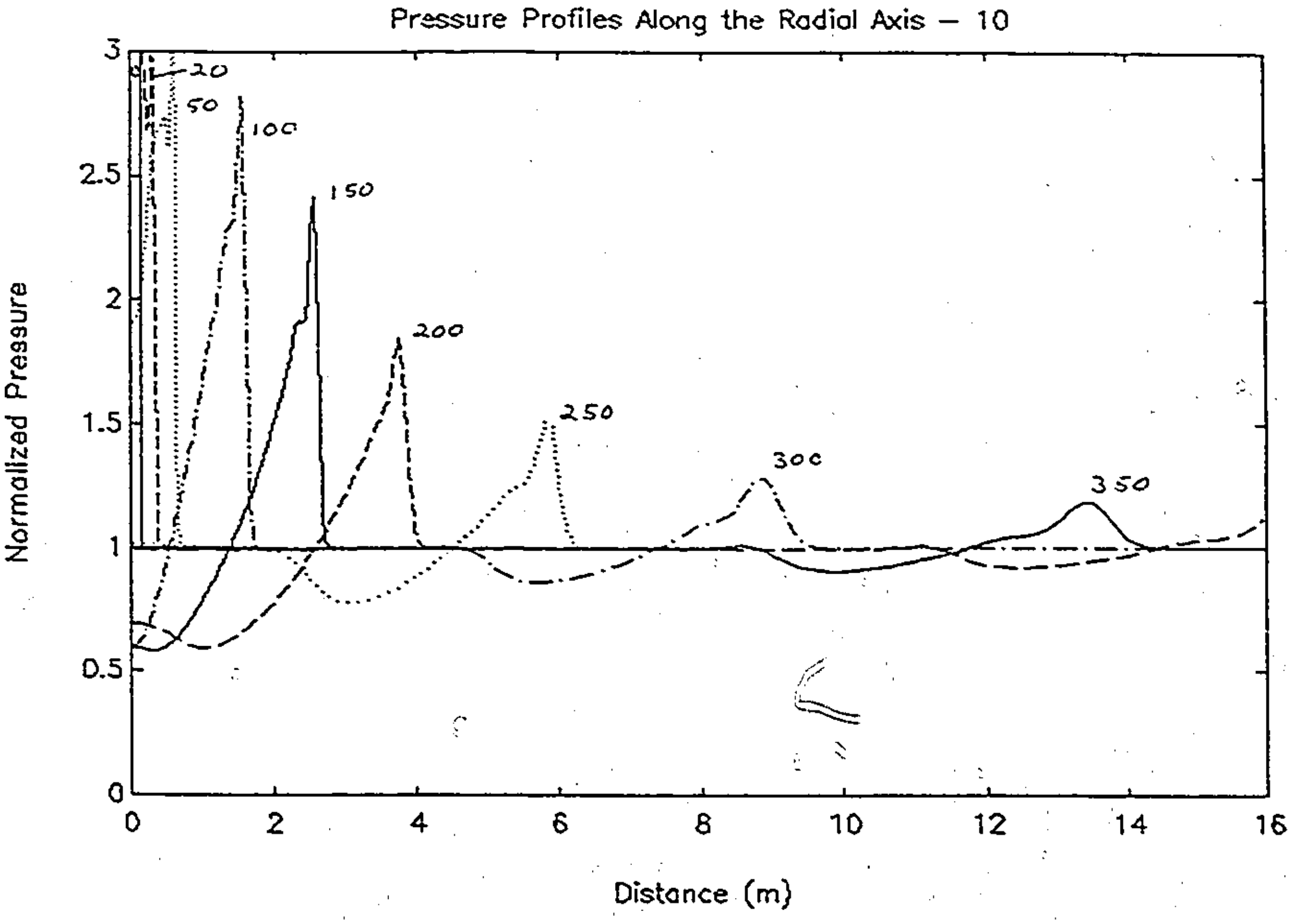

Figure 4.3.3-1 Pressure Radial Profiles, ΔP = 8, E11=10

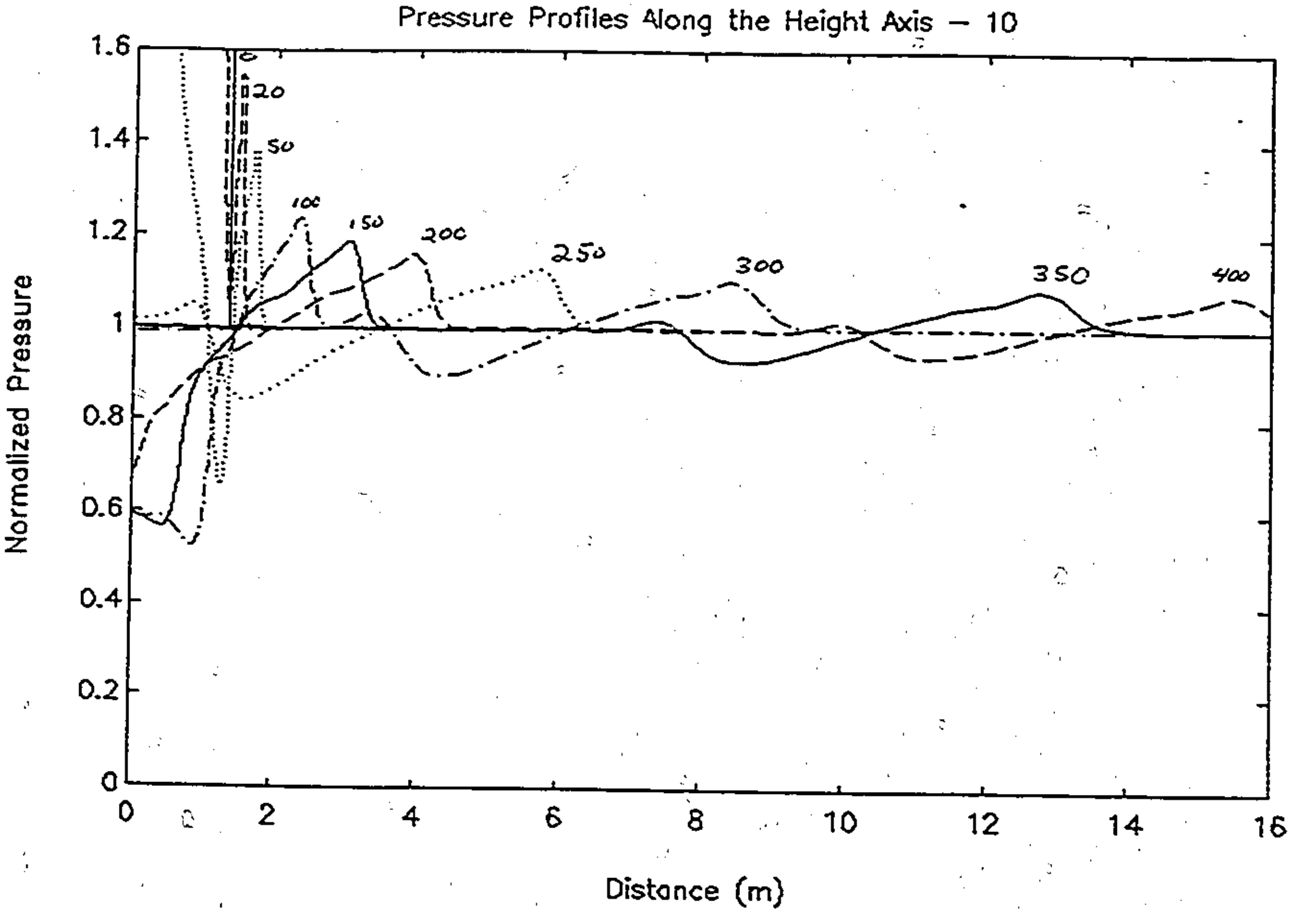

Figure 4.3.3-2 Pressure Height Profiles, ΔP = 8, E11=10

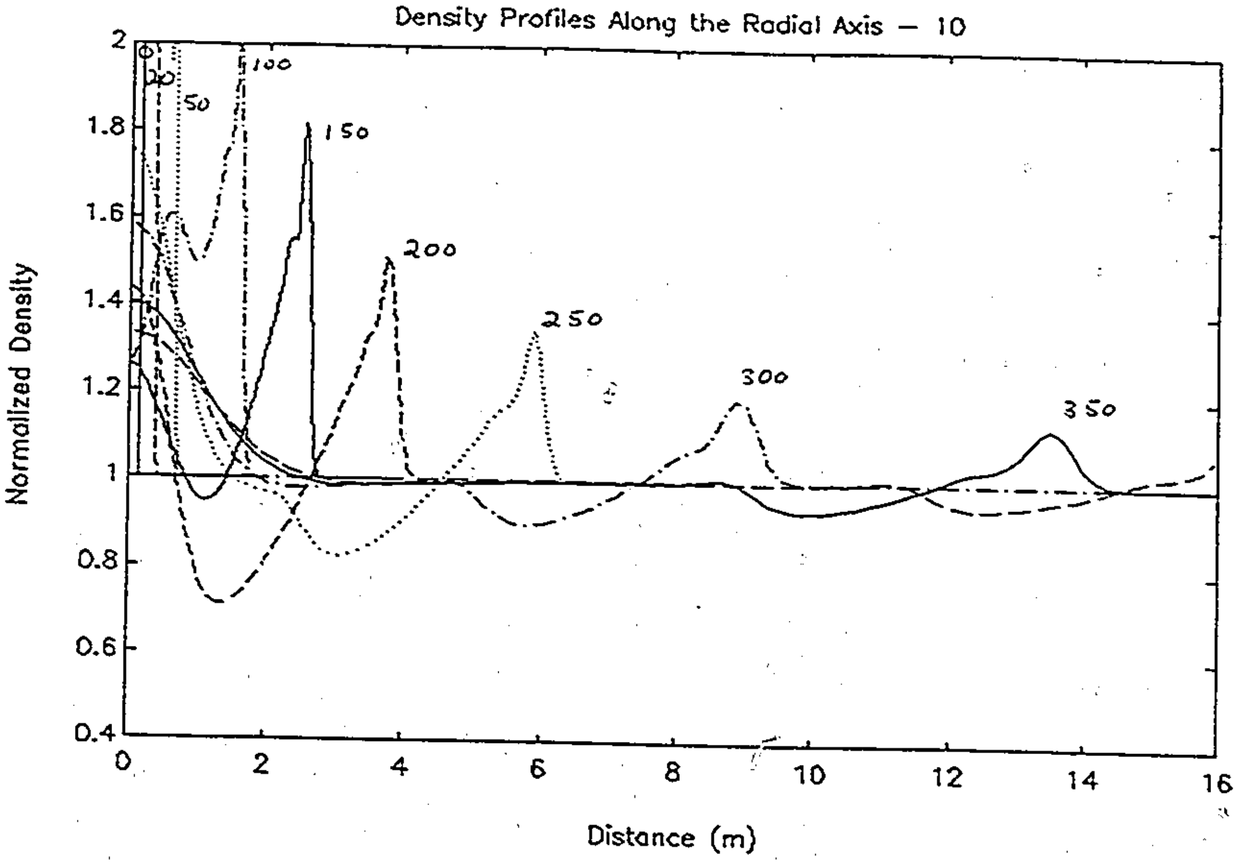

Figure 4.3.3-3 Radial Density Profiles, ΔP = 8, E11 = 10

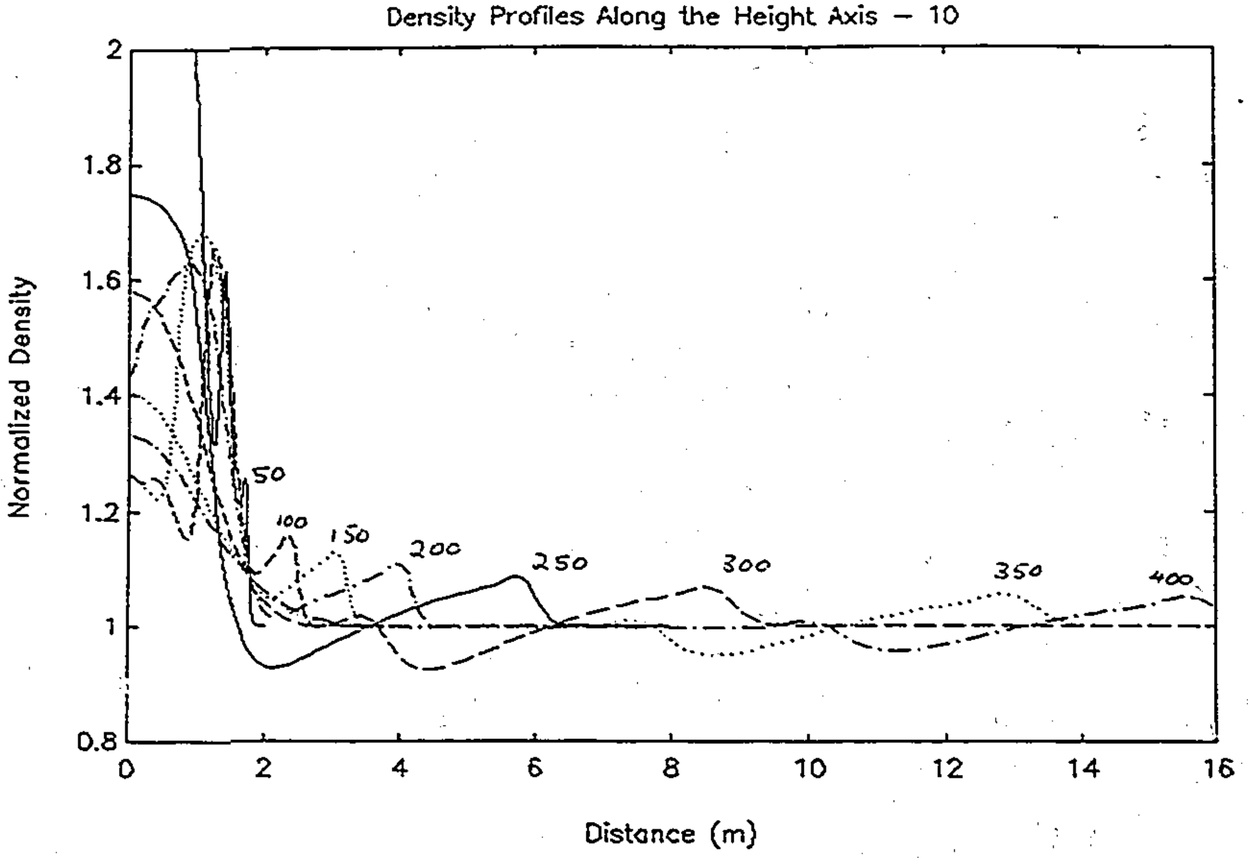

Figure 4.3.3-4 Height Density Profiles, ΔP = 8, Ell = 10

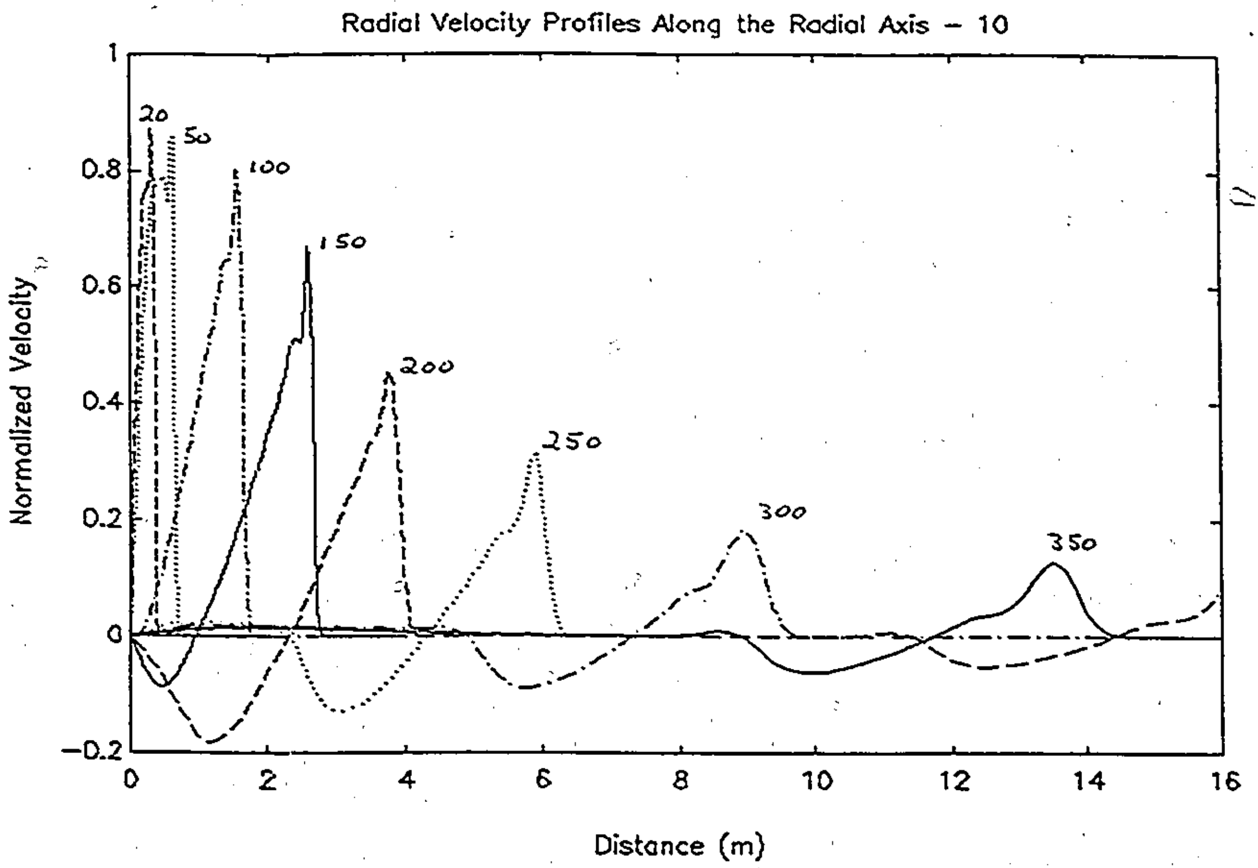

Figure 4.3.3-5 Radial Velocity Radial Profiles, ΔP = 8, E11 = 10

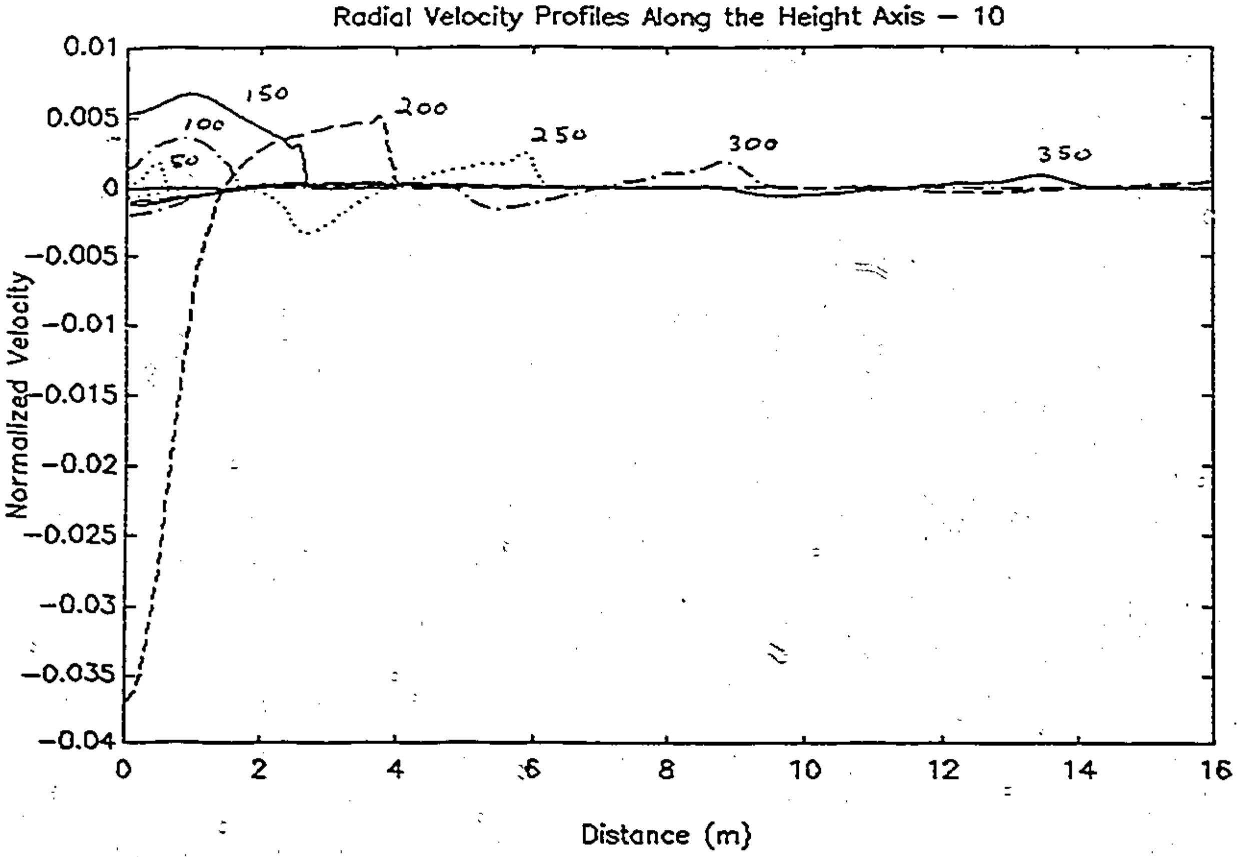

Figure 4.3.3-6 Radial Velocity Height Profiles, ΔP = 8, Ell = 10

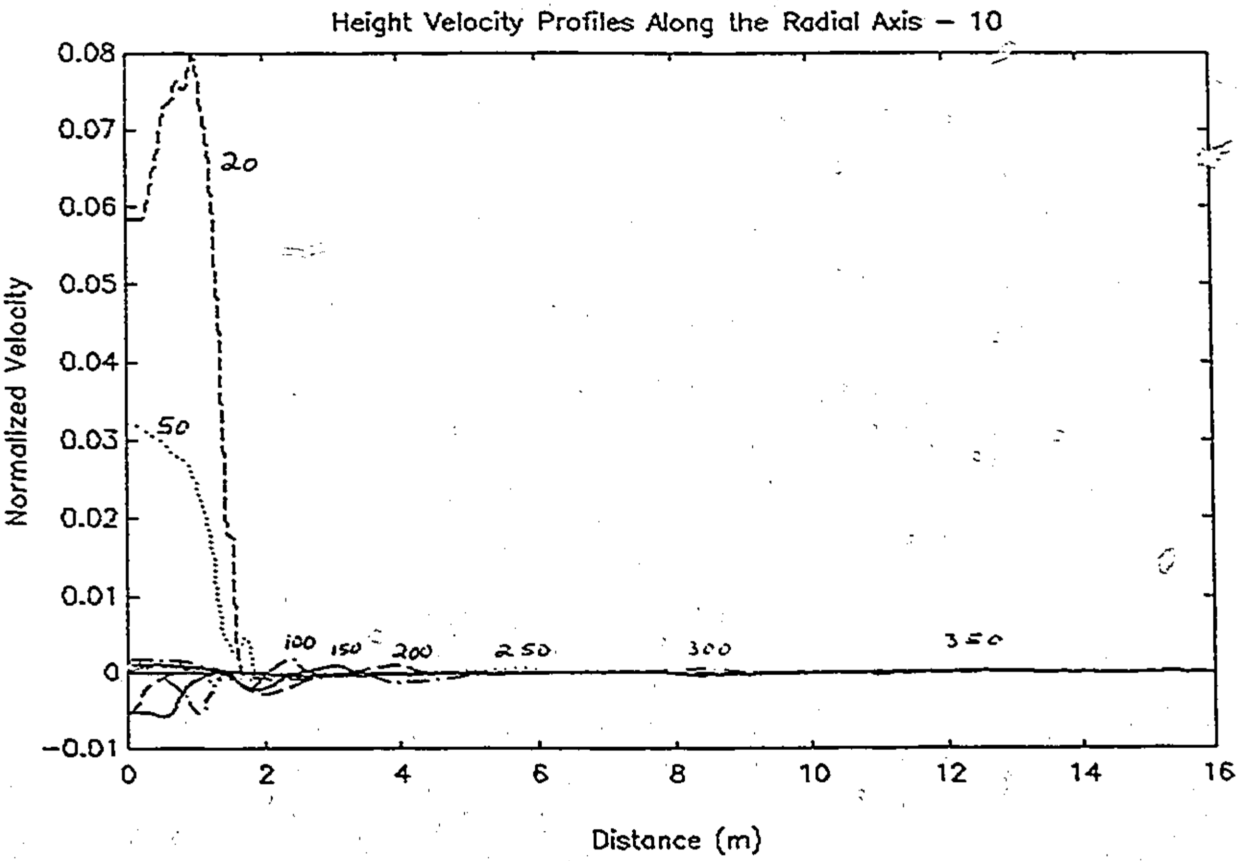

Figure 4.3.3-7 Height Velocity Radial Profiles, ΔP = 8, Ell = 10

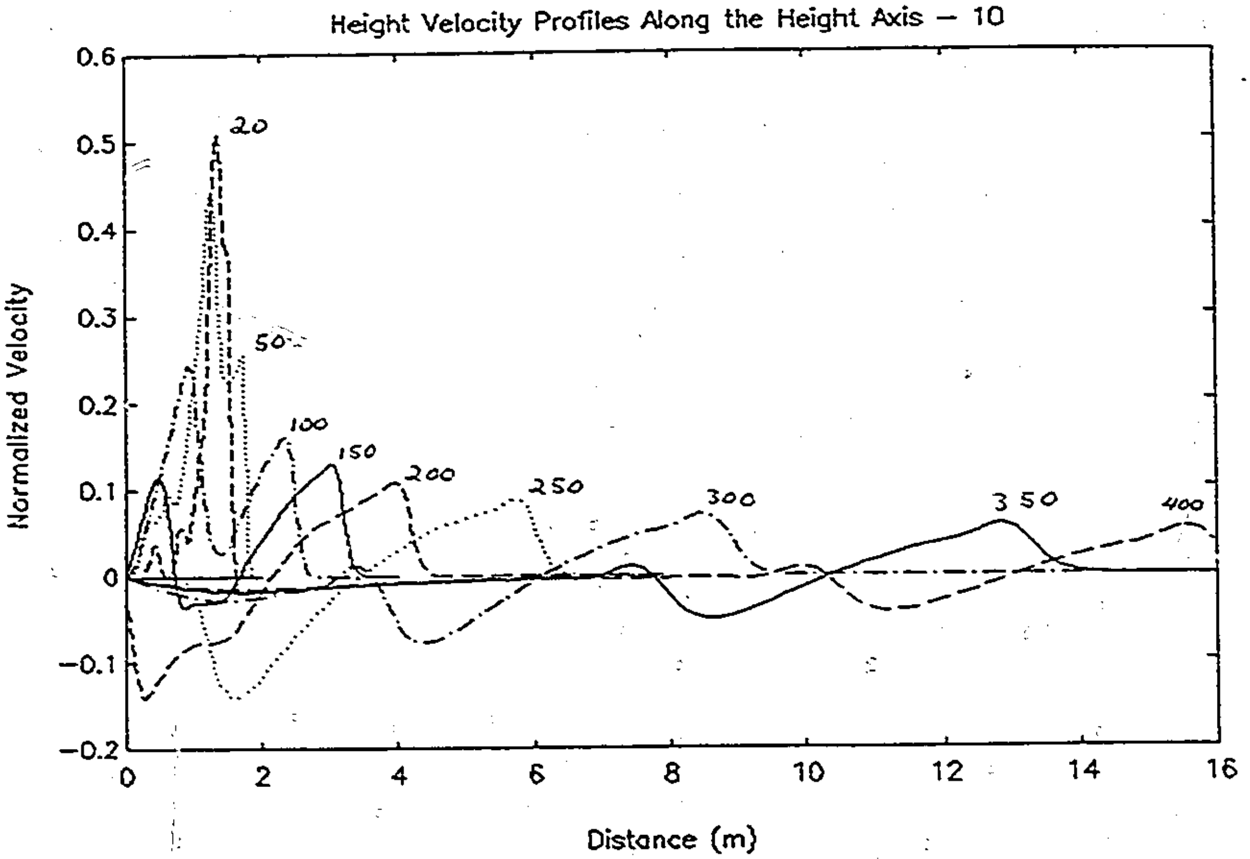

Figure 4.3.3-8 Height Velocity Height Profiles, ΔP = 8, E11 = 10

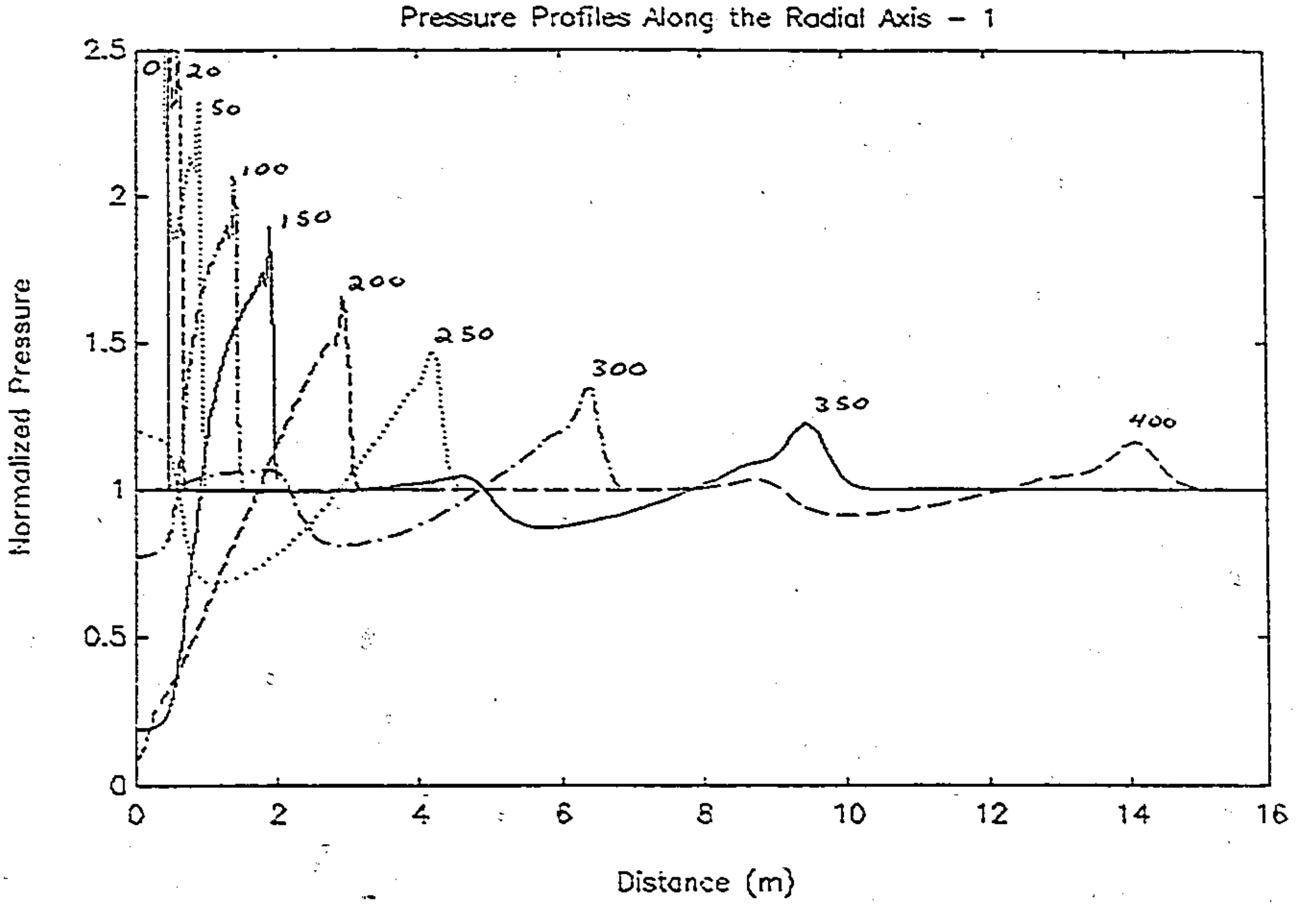

Figure 4.3.4-1 Pressure Profiles, ΔP = 8, E11=1

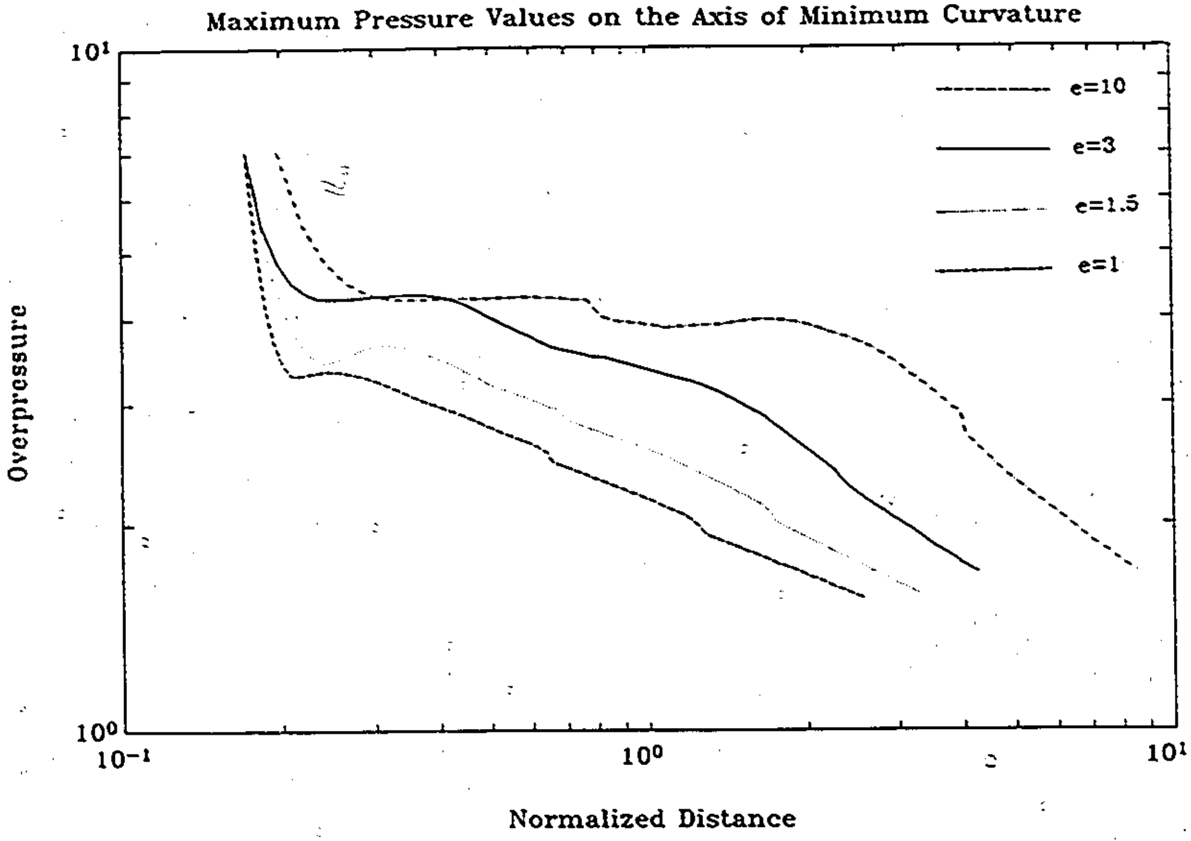

Figure 5.1-1 Peak Pressure Along the Axis of Minimum Curvature, $\Delta P = 19$

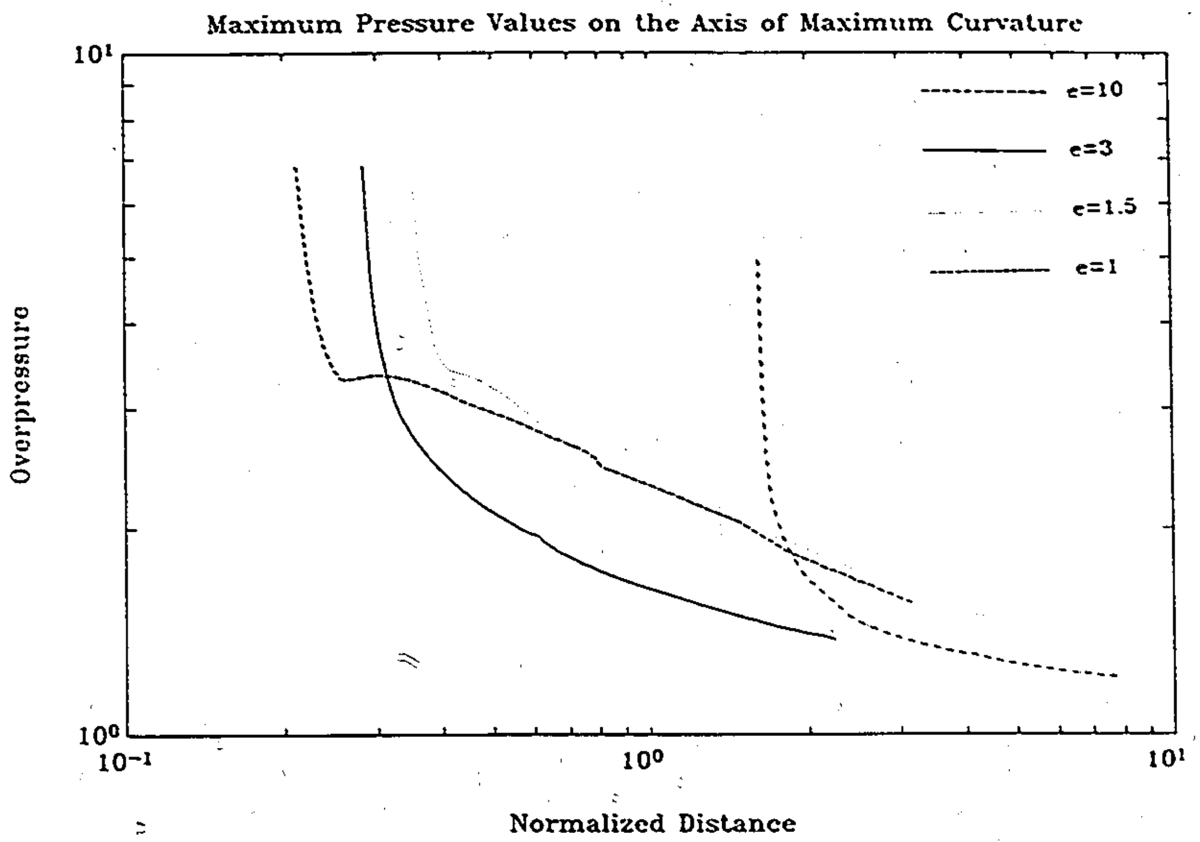

Figure 5.1-2 Peak Pressure Along the Axis of Maximum Curvature, $\Delta P = 19$

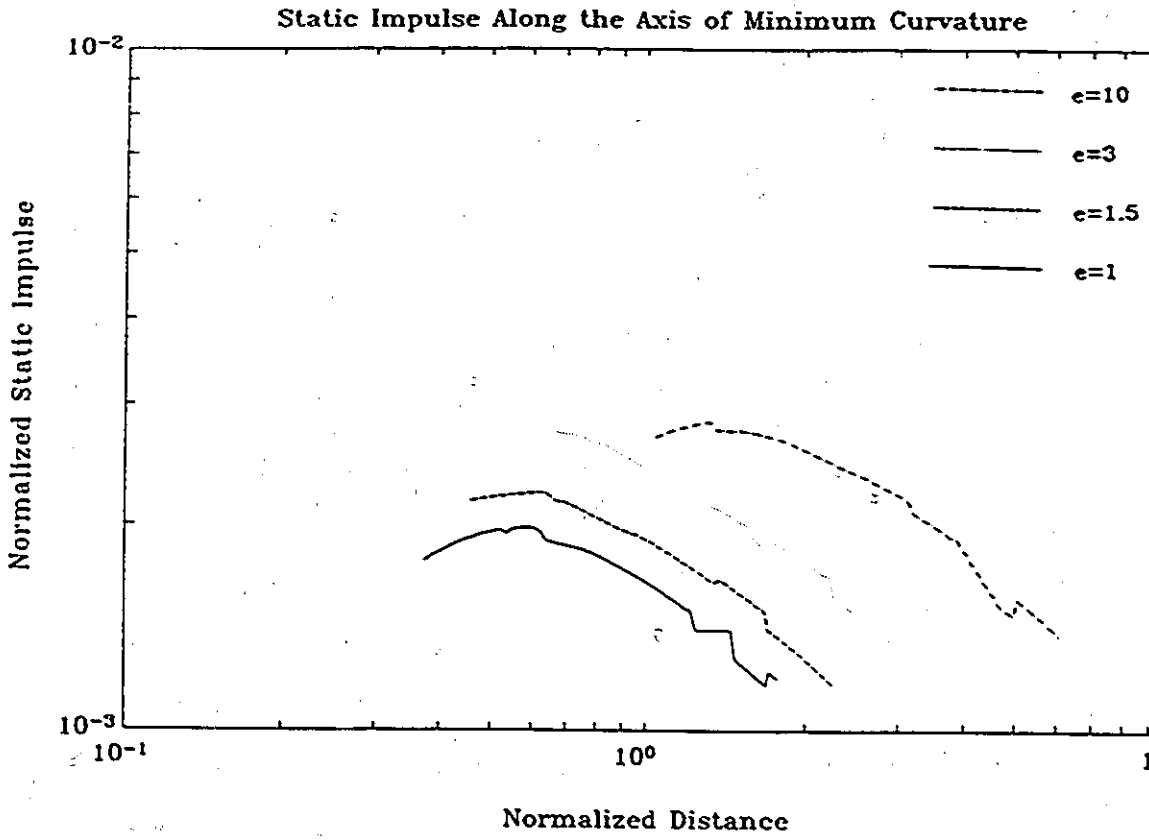

Figure 5.1-3 Static Impulse Along the Axis of Minimum Curvature, $\Delta P = 19$

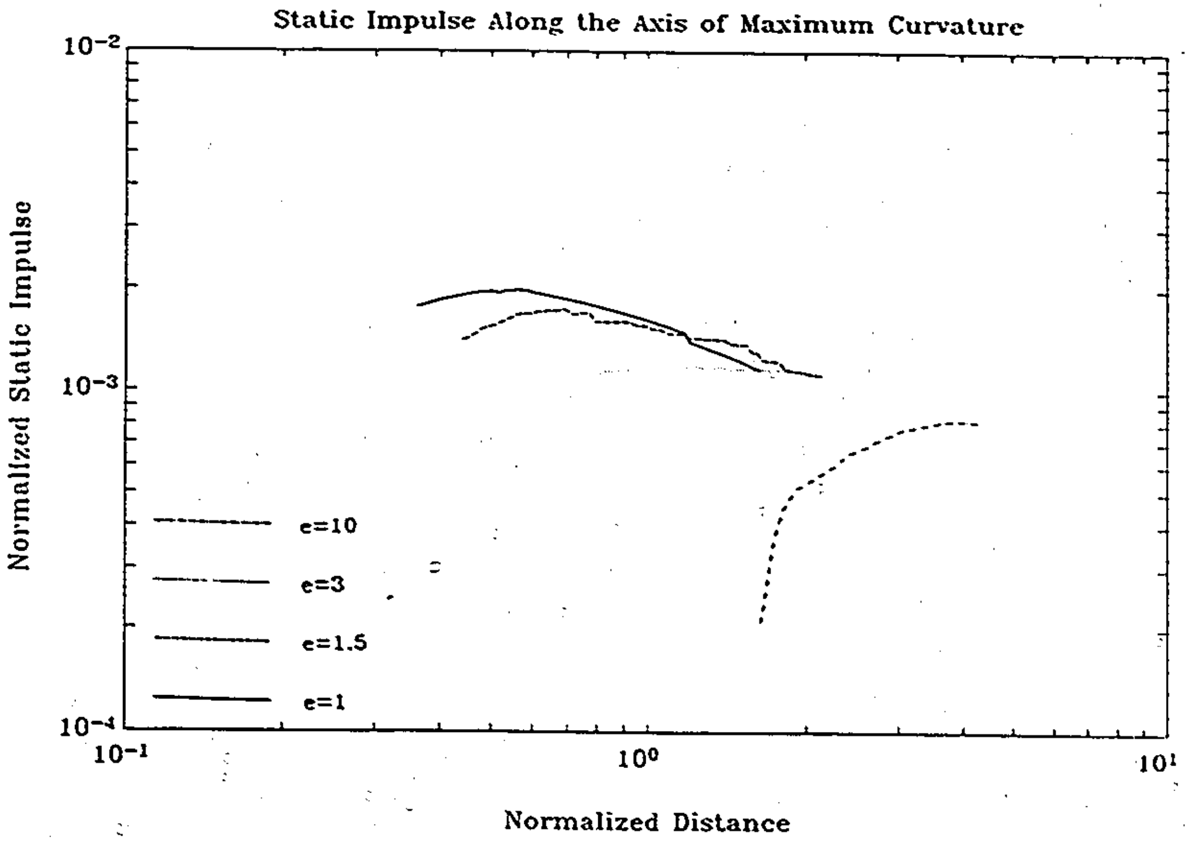

Figure 5.1-4 Static Impulse Along the Axis of Maximum Curvature, $\Delta P = 19$

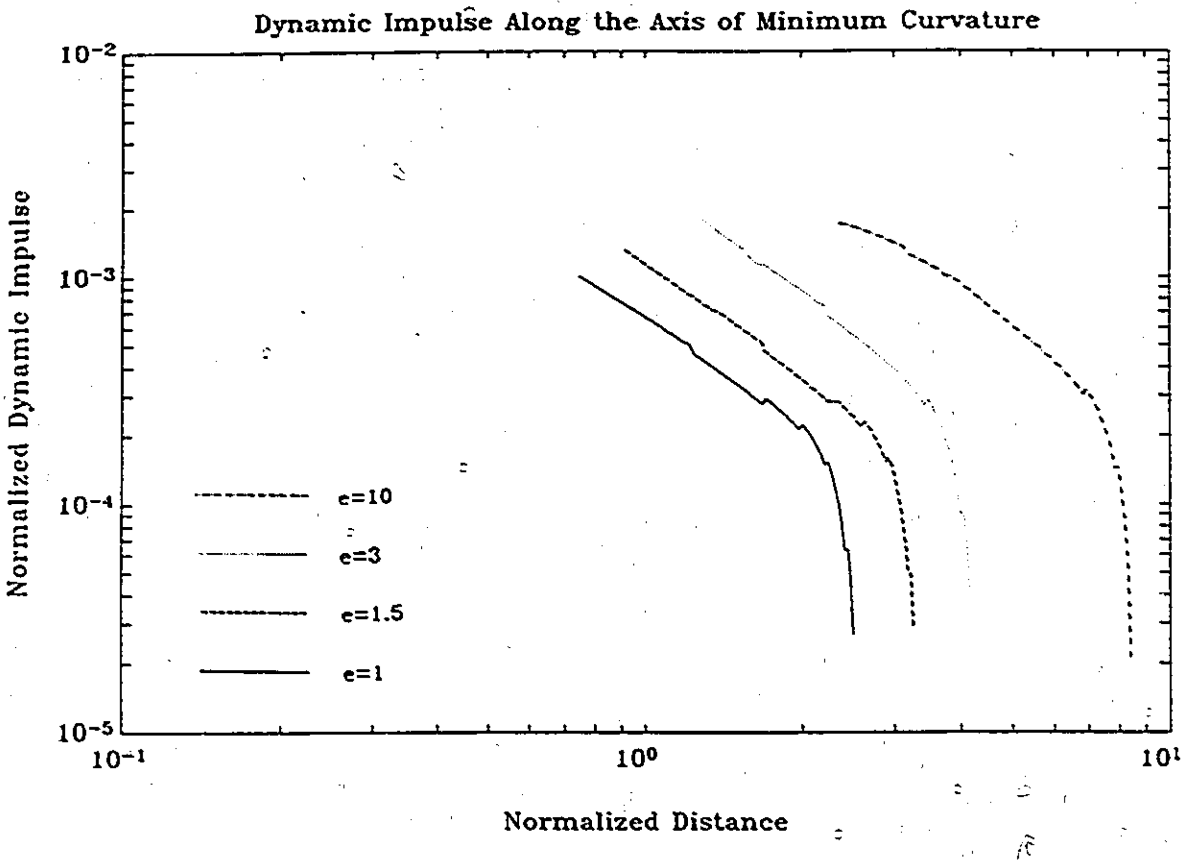

Figure 5.1-5 Dynamic Impulse Along the Axis of Minimum Curvature, $\Delta P = 19$

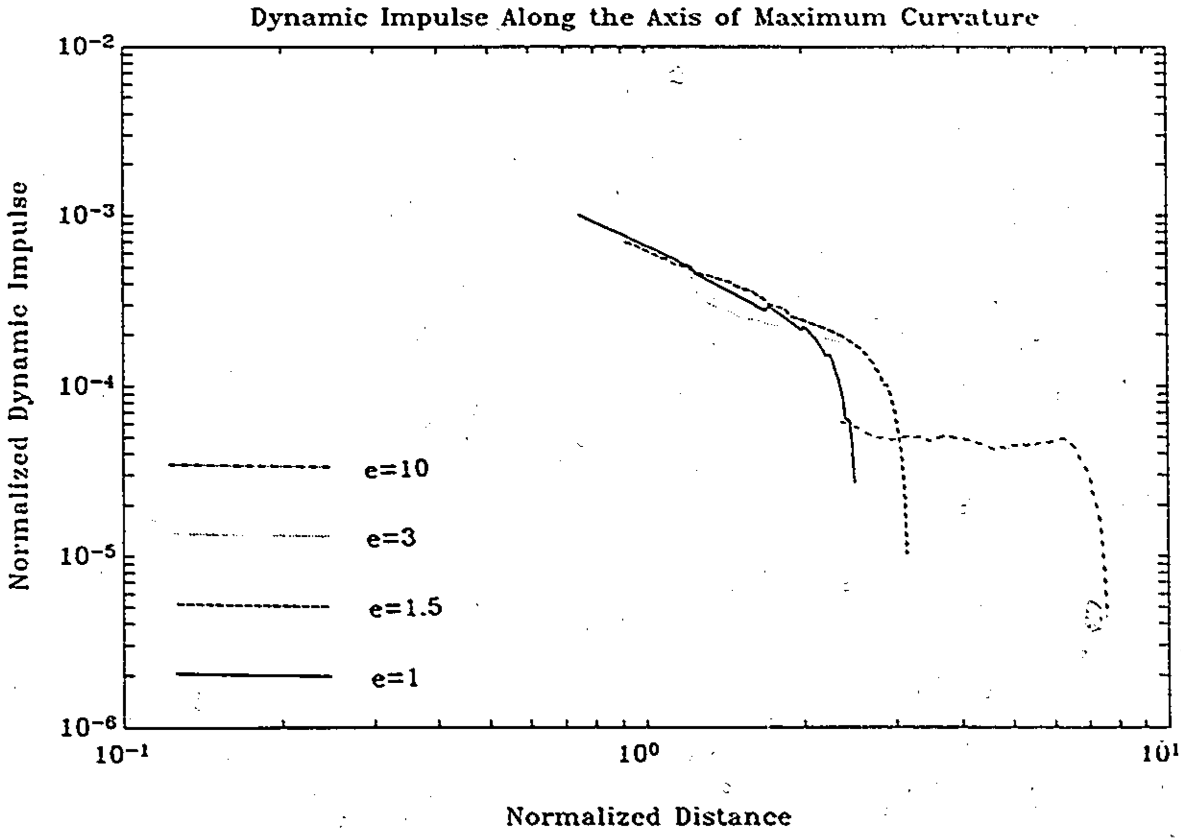

Figure 5.1-6 Dynamic Impulse Along the Axis of Maximum Curvature, ΔP = 19

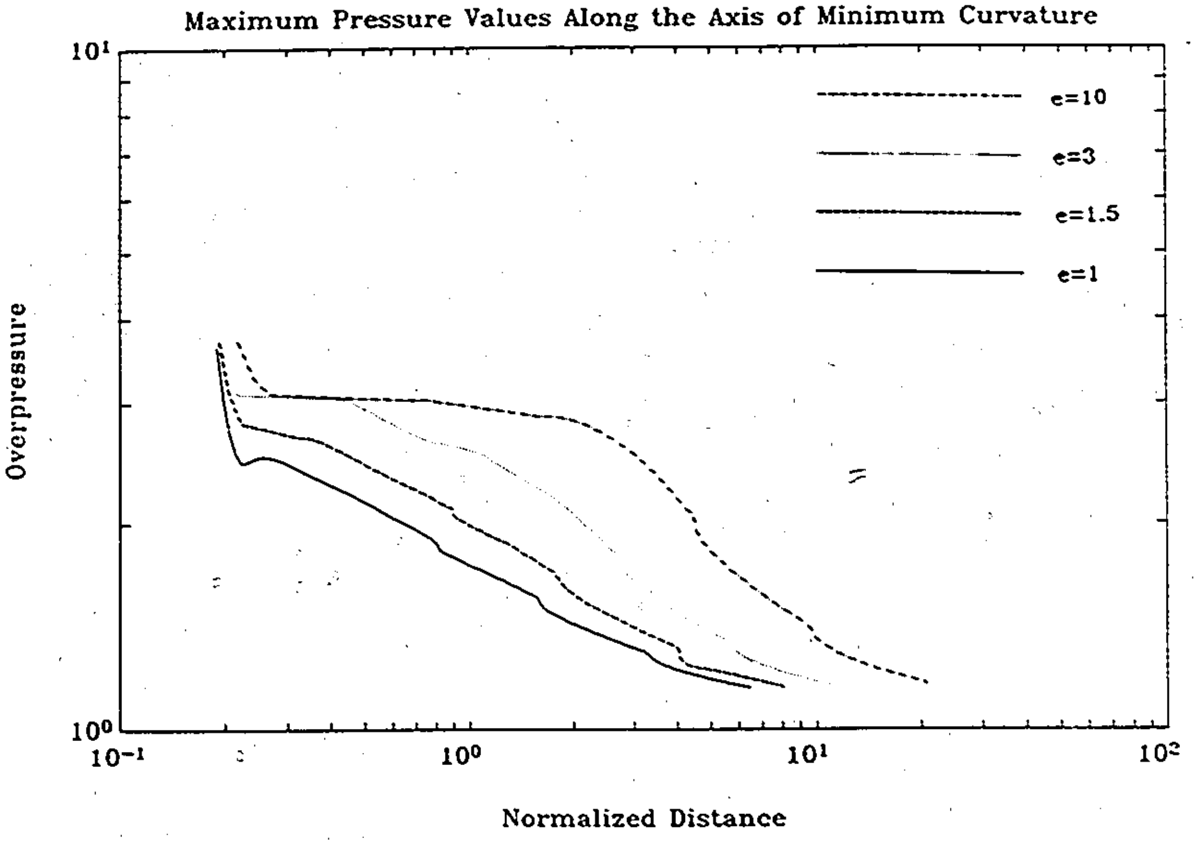

Maximum Pressure Values Along the Axis of Minimum Curvature

Figure 5.2-1 Peak Pressure Along the Axis of Minimum Curvature, $\Delta P = 8$

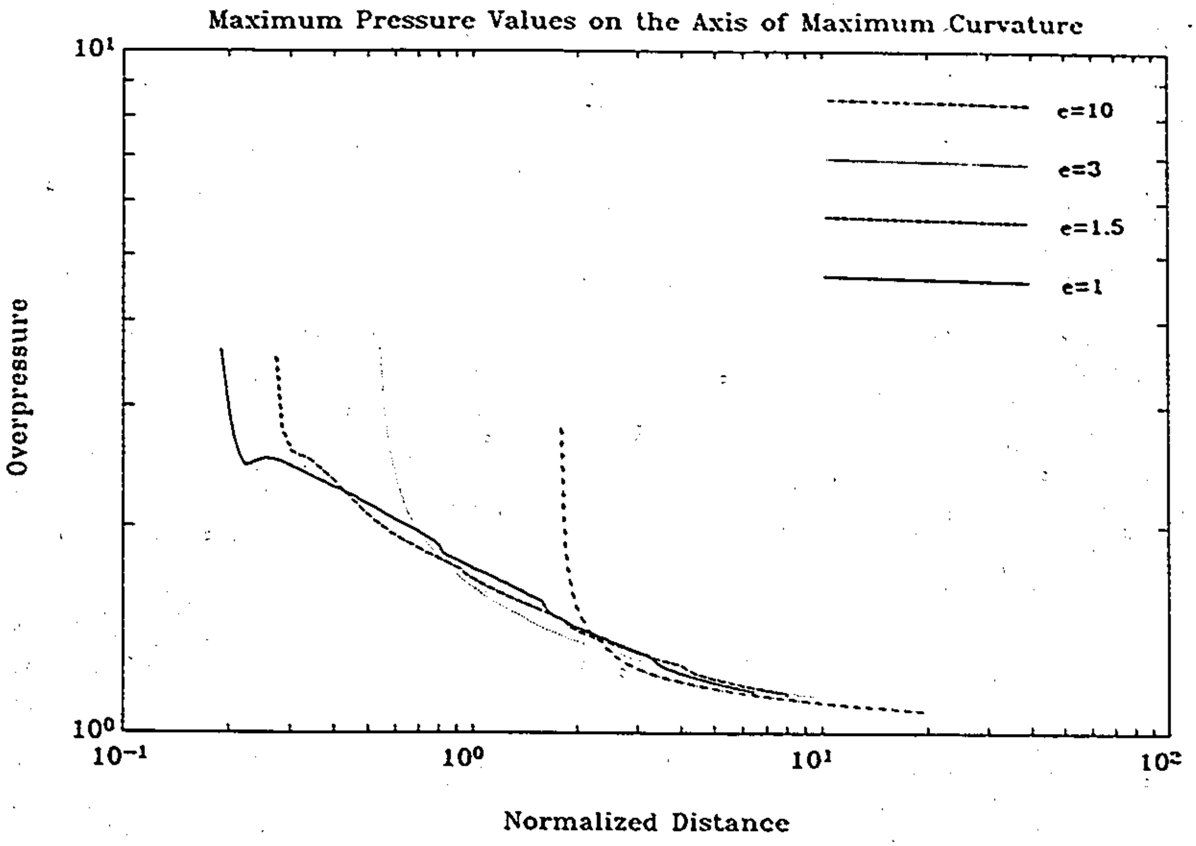

Figure 5.2-2 Peak Pressure Along the Axis of Maximum Curvature, ΔP = 8

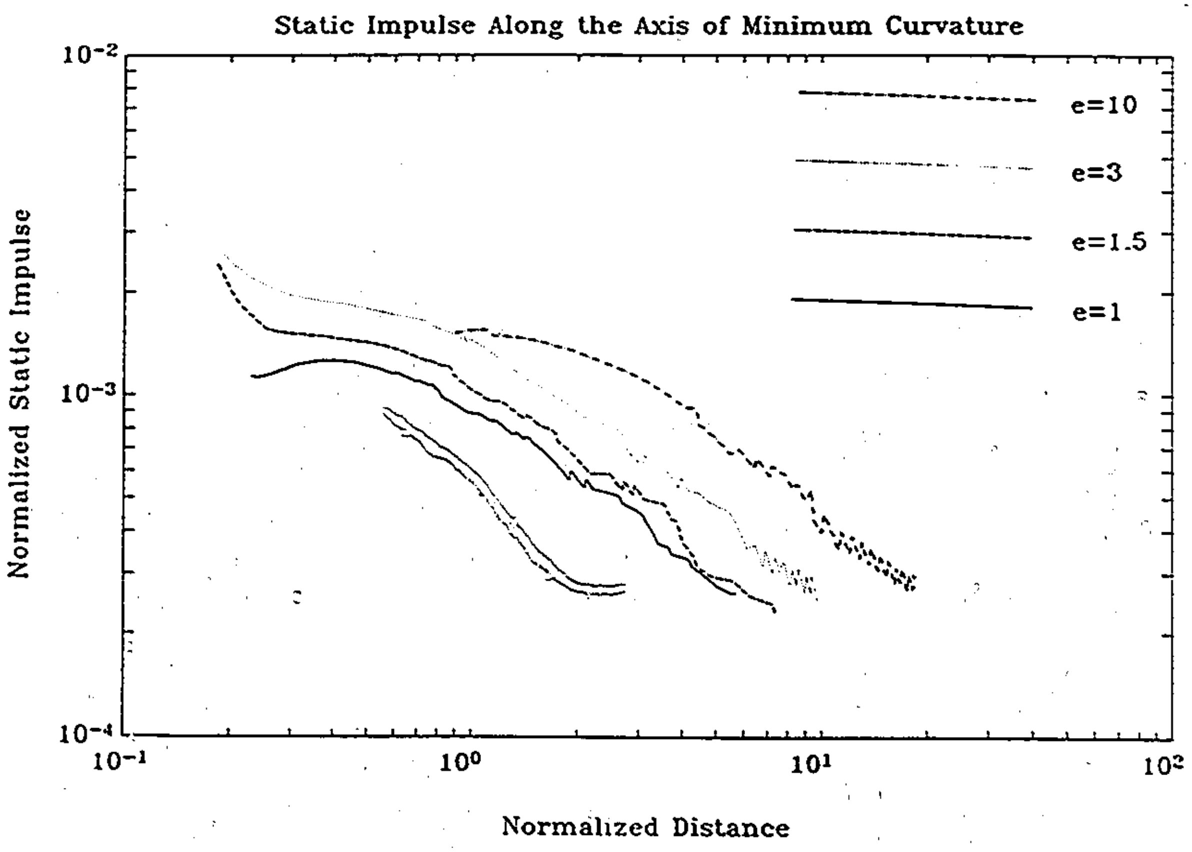

Figure 5.2-3 Static Impulse Along the Axis of Minimum Curvature, $\Delta P = 8$

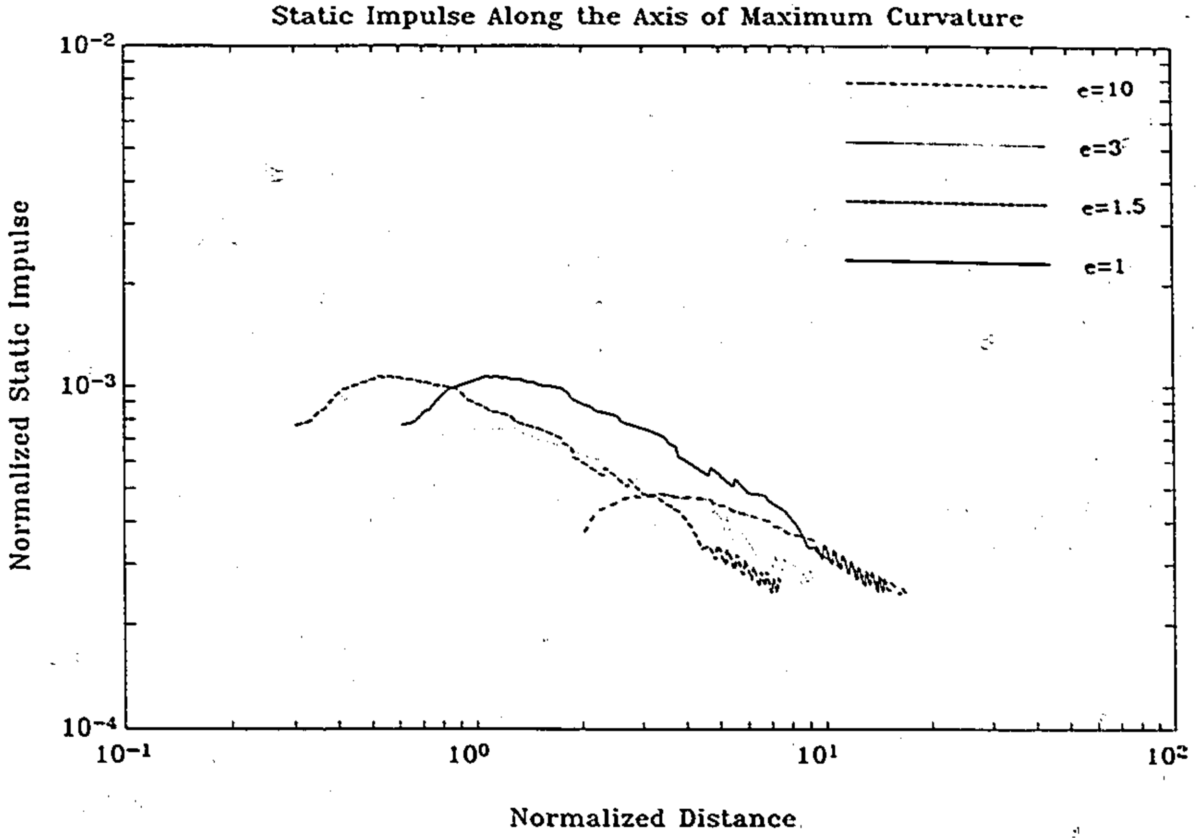

Figure 5.2-4 Static Impulse Along the Axis of Maximum Curvature, $\Delta P = 8$

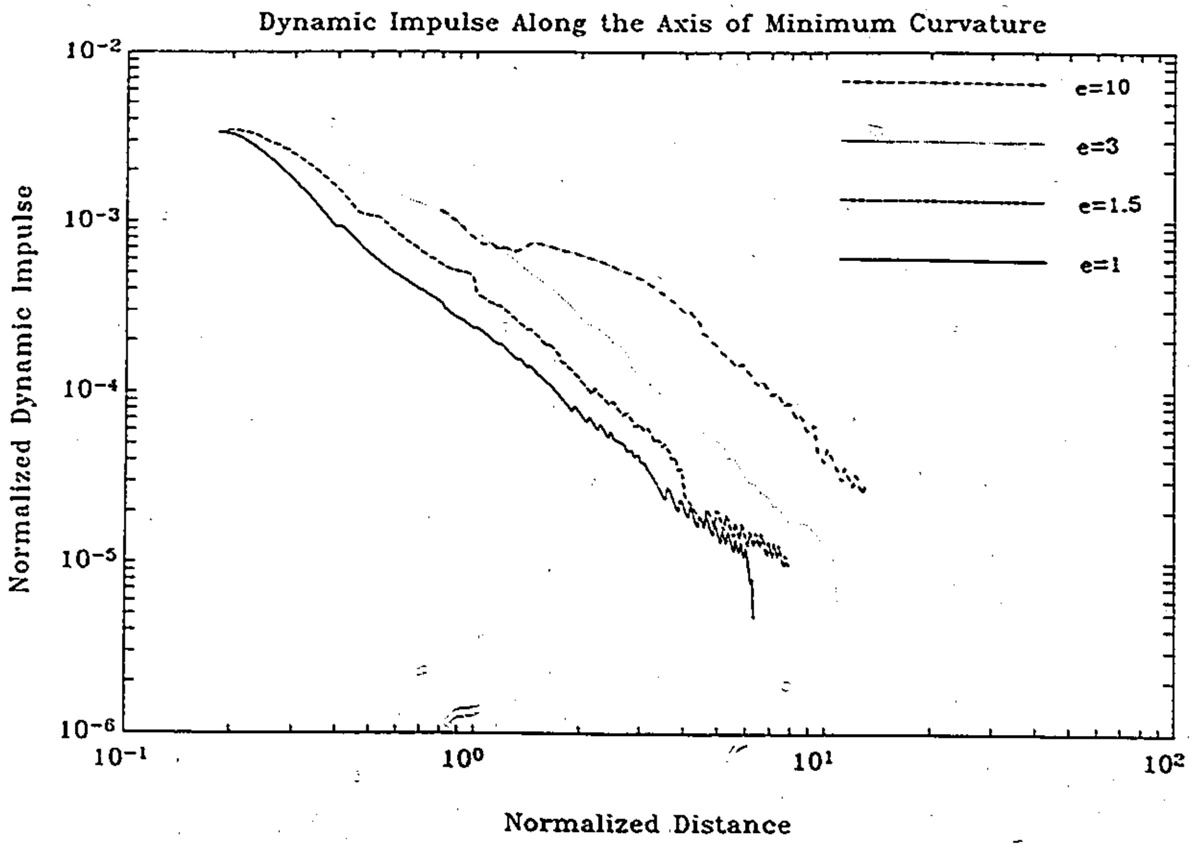

Figure 5.2-5 Dynamic Impulse Along the Axis of Minimum Curvature, $\Delta P = 8$

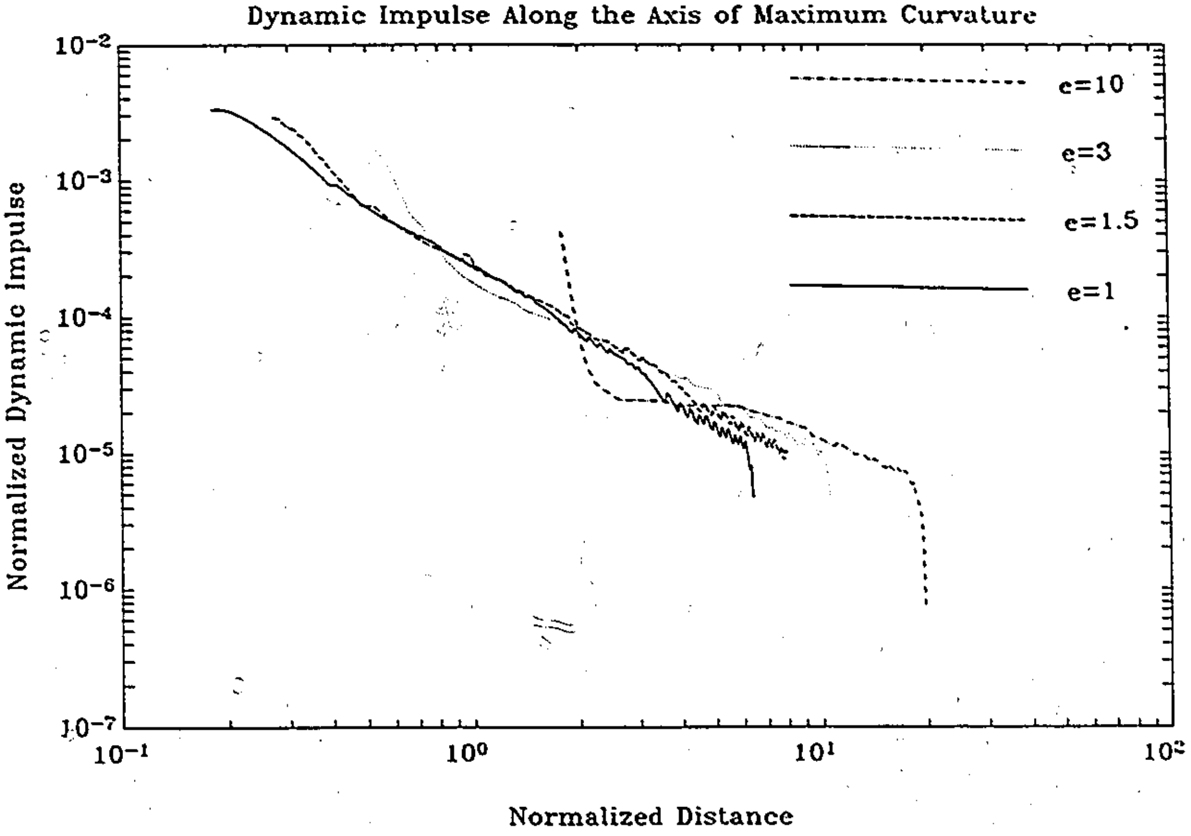

Figure 5.2-6 Dynamic Impulse Along the Axis of Maximum Curvature, ΔP = 8

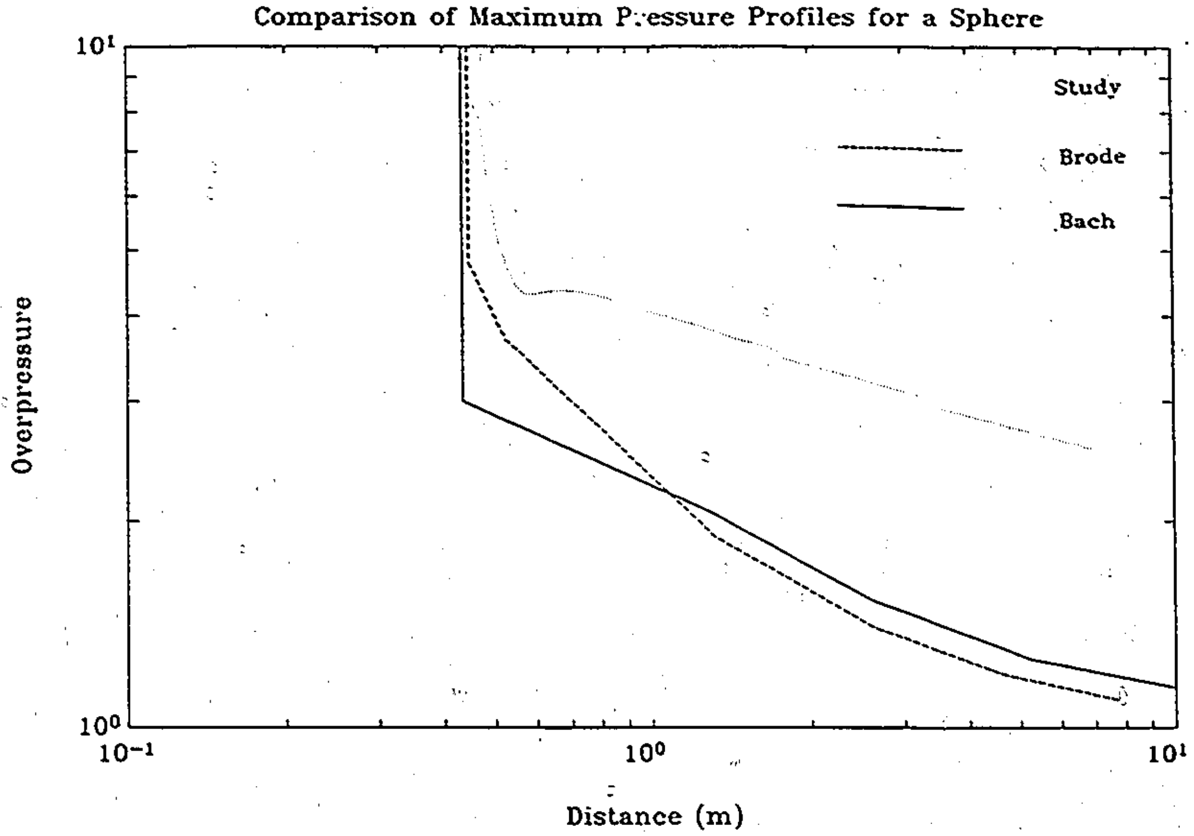

Figure 5.3-1 Comparison of Spherical Models

Appendix A

The question regarding energy equivalence of the blast source is discussed. It is believed that the true energy of an given explosion is the energy delivered to the environment via work done by the expanding explosion products (neglecting other means of energy transport such as radiation). Given the initial states of the sphere and the environment, this energy is unique since the process of the energy transmission is via a shock wave. Unfortunately, the explosion energy cannot be specified a priori without a knowledge of the shock propagation. Only in the case of the ideal point blast in which all the energy release goes to the environment is the explosion energy known a priori.

To estimate the initial energy conditions of the blast wave a prior, two methods are specified. The difference in the methods lies in the thermodynamic path in which the initial state of the sphere (P_o, ρ_o, T_o) is brought to its final state (P_f, ρ_f, T_f), before it bursts. Though it is true that the energy used to prepare the sphere to its busting state is path independent, an accurate evaluation is required.

In the first method, the state of the gas inside the sphere of radius R_i is initially identical to outside the environment. The sphere is then brought to its final state prior to bursting via heat addition at constant volume. The following equation uses the total energy, being the sum of the internal and kinetic, then uses the fact that the perfect gas is motionless.

$$E_{total} = 4\Pi \int_0^{R_o} \rho \; (e_{internal} + \frac{u^2}{2}) \; r^2 \, dr$$

$$= \frac{4}{3} \, \Pi \, \frac{(P_f - P_0)}{\gamma - 1} R_i^3$$

This uses the perfect gas law;

$$e_{internal} = \frac{1}{\gamma - 1} \, \frac{P}{\rho}$$

Due to the temperature change experienced by the sphere, this method is called the hot sphere case.

In the second method, the sphere starts at an ambient condition. The sphere is then pressurized isothermally by mass addition to its bursting state. If the process is considered to be one of isothermal compression then the energy given to the sphere is;

$$E_{total} = \frac{4\Pi}{3} R_o^3 \int_{\rho_o}^{\rho_f} e_{internal}\, d\rho$$

$$= \frac{4\Pi}{3} R_o^3 P_o \ln(\frac{\rho_o}{\rho_f})$$

which again uses the perfect gas law.

due to the lack of a temperature change, this method is called the cold sphere case.

These two methods of the hot and cold sphere are chosen because they represent practical cases. The hot sphere method can be achieved via combustion at constant volume. The cold sphere method can be achieved by the volumetric expansion of a pressurized tank or balloon at equilibrium with the outside environment.